Titre: Title:	Validation of DRAGON5 Lattice Code for PWR (Pressurized Water Reactor) Applications Using Depletion Benchmarks by Detailed Comparison with SERPENT2 Monte Carlo Code
Auteur: Author:	Levon Ghasabyan
Date:	2020
Type:	Mémoire ou thèse / Dissertation or Thesis
Référence: Citation:	Ghasabyan, L. (2020). Validation of DRAGON5 Lattice Code for PWR (Pressurized Water Reactor) Applications Using Depletion Benchmarks by Detailed Comparison with SERPENT2 Monte Carlo Code [Mémoire de maîtrise, Polytechnique Montréal]. PolyPublie. https://publications.polymtl.ca/5527/

URL de PolyPublie: PolyPublie URL:	https://publications.polymtl.ca/5527/
Directeurs de recherche: Advisors:	Alain Hébert
Programme: Program:	Génie physique

POLYTECHNIQUE MONTRÉAL
affiliée à l'Université de Montréal

Validation of DRAGON5 lattice code for PWR (Pressurized Water Reactor) applications using depletion benchmarks by detailed comparison with SERPENT2 Monte Carlo code

LEVON GHASABYAN
Département de génie physique

Mémoire présenté en vue de l'obtention du diplôme de *Maîtrise ès sciences appliquées*
Génie énergétique

Décembre 2020

POLYTECHNIQUE MONTRÉAL
affiliée à l'Université de Montréal

Ce mémoire intitulé :

Validation of DRAGON5 lattice code for PWR (Pressurized Water Reactor) applications using depletion benchmarks by detailed comparison with SERPENT2 Monte Carlo code

présenté par **Levon GHASABYAN**
en vue de l'obtention du diplôme de *Maîtrise ès sciences appliquées*
a été dûment accepté par le jury d'examen constitué de :

Njuki MUREITHI, président
Alain HÉBERT, membre et directeur de recherche
Guy MARLEAU, membre

ACKNOWLEDGEMENTS

First of all, I would like to thank my research director Prof. Alain Hébert, who invited and helped me with all the big and small problems along these two and half years of my studies. This research would not have been possible without his continuous guidance and wise advice.

I am thankful to Prof. Guy Marleau for his valuable help with the registration issues and advises related to scholarships and funding.

Special thanks to Ahmed Naceur, who was always ready to help me with everyday issues at the campus.

Finally, my thoughts are with my Family who has provided the crucial everyday support needed to finalize these studies.

RÉSUMÉ

L'objectif de ce projet est de valider un schéma de calcul à deux niveaux pour quatre benchmarks d'assemblage de réacteurs à eau sous pression (REP) avec le code de réseau DRAGON5. Ici, nous validons le schéma à deux niveaux par rapport à un schéma classique à un niveau du calcul DRAGON5 et le comparons avec les résultats du code Monte-Carlo SERPENT2 à trois burnups différents. Les résultats sont comparés à 0 burnup, au burnup à k_{eff} maximum et au burnup maximum de 70 GWd/t. De plus, trois benchmarks de cellules uniques PWR sont validés en comparant les résultats du schéma à un niveau DRAGON5 avec ceux du code Monte-Carlo SERPENT2. Le schéma classique à un niveau utilise généralement la méthode des probabilités de collision (CP) pour les calculs de cellules uniques et la méthode des caractéristiques (MOC) pour les calculs d'assemblage. Les calculs MOC sont capables de traiter des problèmes plus complexes et de fournir une meilleure précision au prix d'un plus grand coût de calcul. Un schéma à deux niveaux a été proposé pour traiter les assemblages PWR. Au premier niveau, la méthode à courant d'interface (IC) est utilisée sur un maillage d'énergie à 295 groupes pour effectuer un calcul de flux efficace. Tous les schémas de calcul utilisent un calcul d'autoprotrection basé sur la méthode des sous-groupes avec des tables de probabilités mathématiques avec une technique de solution IC. Le premier niveau est suivi par une correction de Super Homogénéisation (SPH). Ensuite, au deuxième niveau, la méthode MOC utilise l'estimation initiale du flux pour effectuer un calcul de flux plus détaillé sur le maillage énergétique de 26 groupes. Dans cette étude, nous montrons que le schéma optimisé à deux niveaux est capable d'effectuer un calcul d'assemblage PWR plus rapidement sans perte significative de précision de calcul.

ABSTRACT

The goal of this project is to validate a two-level calculation scheme of four Pressurized Water Reactor (PWR) assembly benchmarks with the DRAGON5 lattice code. Here, we validate the two-level scheme with classical one-level scheme of DRAGON5 calculation and compare it with the results of SERPENT2 Monte Carlo code at three different burnups. The results are compared at 0 burnup, burnup at maximum k_{eff} and at maximum burnup of 70 GWd/t.

Additionally, three PWR pin cell benchmarks are validated by comparing DRAGON5 one-level scheme results with those of SERPENT2 Monte Carlo code.

The classical one-level scheme typically uses Collision Probability (CP) method for pin cell calculations and Method of Characteristics (MOC) for assembly calculations. MOC calculations are capable of handling larger problems and provide better accuracy at the expense of being computationally more intensive.

A two-level scheme was proposed for PWR assemblies. At the first level, Interface Current (IC) method is used on 295-group energy mesh to perform efficient flux calculation. All computational schemes use subgroup self-shielding with mathematical probability tables and IC solution technique. The first level is followed by Super Homogenisation (SPH) correction. Then, at the second level, MOC method uses initial estimate of the flux to perform a more detailed flux calculation on the 26-group energy mesh.

In this study, we show that the optimized two-level scheme is capable of performing a PWR assembly calculation essentially faster without any significant loss of calculation precision.

TABLE OF CONTENTS

LIST OF TABLES

LIST OF FIGURES

LIST OF SYMBOLS AND ACRONYMS

PWR	Pressurized Water Reactor
UOX	Uranium Oxide
Gd	Gadolinium
BTE	Boltzmann Transport Equation
MOC	Method of Characteristics
CP	Collision Probability
DO	Discrete Ordinates
IC	Interface Current
SPH	Super Homogenisation
CPU	Central Processing Unit
RE	Relative Error
1L/2L	one-level/two-level computational scheme
G1/G2	Group 1/Group 2
XS	Cross Section
BU	Burnup

LIST OF APPENDICES

CHAPTER 1 INTRODUCTION

The detailed modeling of nuclear reactors using deterministic computational tools is driven by the increased availability of concurrent computation resources and advanced reactor designs [1].

The complex task of simulating a nuclear reactor core presently requires use of two types of deterministic codes. The first is a lattice code which is used to generate a multi-parameter reactor database by solving the Boltzmann Transport Equation (BTE) for a pin cell or an assembly for different materials. The second is a diffusion code used to compute the neutron flux in the reactor core using the generated reactor database.

Advances in the computational methods employed to solve the BTE are creating the ground for CPU-efficient production tools which can efficiently generate high resolution reactor databases [2].

1.1 Research Scope

The scope of this research project is to validate an optimized 2-level calculation scheme [2] of deterministic lattice code DRAGON5 for PWR assemblies with and without gadolinium pins. We validate the 2-level scheme by comparing it with the 1-level scheme and with SERPENT2 [3] Monte-Carlo calculations at different burnups. To achieve our goal we use a specific benchmark which was designed to validate lattice code accuracy for PWR applications in depletion conditions.

1.2 Research Objectives

The main objective of this study is to validate a two-level computational scheme for PWR pin cells and fuel assemblies using DRAGON5 lattice code. The validation was conducted at different burnups and supplements the results reported by Canbakan in [2]. The two-level DRAGON5 calculations are verified by Monte Carlo simulations conducted via SERPENT2 code [4]. The second objective is to show the pros and cons of two-level over one-level scheme. Thus identical one-level calculations were performed and compared with two-level scheme. The final objective is to make this study easily reproducible by interested parties. As such, the SERPENT2 and DRAGON5 input/output files and the code used to parse and analyse the results is distributed along the thesis in a portable and organized way.

1.3 Methodology

The study was conducted for pin cells and fuel assemblies. 4 pin cells with the same geometry but different materials were evaluated using one-level scheme. 3 calculations were run with CP method. Three PWR fuel assemblies were evaluated using one-level and two-level schemes. For assembly calculations MOC method was used. All seven test cases were implemented for SERPENT2 code and evaluated. The results of these calculations were analysed and compared.

1.4 Thesis Outline

Chapter 2 covers the theoretical concepts on which DRAGON5 input files were constructed. Chapter 3 presents the detailed description of benchmark and its seven test cases. Afterwards, the the validation results are presented by charts, heat maps and tables which draw parallels between DRAGON5 and SERPENT2 calculations. Finally, Chapter 4 concludes the thesis by summarizing the results and presenting the advantages and limitations of one-level/two-level schemes.

CHAPTER 2 LITERATURE REVIEW AND THEORETICAL BASIS

This chapter presents the theoretical foundations of the work done in this project. First of all, the particle flux is defined which is the solution of the Boltzmann Transport Equation (BTE). Then we present the transport equation and the numerical methods which are used to solve it for real-world nuclear reactor systems. The formalism used in this chapter follows the book of A. Hébert *Applied Reactor Physics* [5].

2.1 The Boltzmann Transport Equation

The BTE describes the neutron flux distribution in space at a specific time. Here the BTE equation and the methods used to solve it are presented.

2.1.1 Core definitions

To be able to quantify the neutron population in time an approach from statistical mechanics is utilized. It presumes that each particle is moving in a six-dimensional phase space. Out of these six-dimensions, three dimensions describe the position of the particle and the other three its velocity. The particle is localized by:

- position $\boldsymbol{r} = x\boldsymbol{i} + y\boldsymbol{j} + z\boldsymbol{k}$
- velocity $\boldsymbol{V}_n = \dfrac{d\boldsymbol{r}}{dt}$, where $V_n = \|\boldsymbol{V}_n\|$ and $\hat{\boldsymbol{\Omega}} = \dfrac{\boldsymbol{V}}{V}$

The population of particles is presented with particle density $n(\boldsymbol{r}, V_n, \boldsymbol{\Omega}, t)$ so that $n(\boldsymbol{r}, V_n, \boldsymbol{\Omega}, t)d^3r dV_n d^2\Omega$ is the number of particles inside volume element d^3r at point $\boldsymbol{r}$ within velocity element dV_n surrounding V_n and the solid angle element $d^2\Omega$ surrounding $\boldsymbol{\Omega}$ at time t. In reactor physics the particle flux ϕ is preferably used and is defined as:

$$\phi\left(\boldsymbol{r}, V_n, \boldsymbol{\Omega}, t\right) = V_n n\left(\boldsymbol{r}, V_n, \boldsymbol{\Omega}, t\right) \tag{2.1}$$

In many engineering problems angular dependence is not important and equation 2.1 can be integrated over $\boldsymbol{\Omega}$. The result is an integrated flux:

$$\phi\left(\boldsymbol{r}, V_n, t\right) = \int_{4\pi} d^2\Omega \phi\left(\boldsymbol{r}, V_n, \boldsymbol{\Omega}, t\right) \tag{2.2}$$

Neutron transport is a complex process in which neutrons travel through the atoms of a medium. During their travel the following processes can happen

- leakage of neutrons out of a control volume
- scattering of neutrons away from nuclei
- capture of neutrons by nuclei followed by a variety of nuclear events
- generation of two or more neutrons from fission events

Each type of nuclear reaction can occur with some probability. The probability of occurrence of the reaction x on a nucleus i is characterised with a microscopic cross section $\sigma_{x,i}$. $\sigma_{x,i}$ has a dimension of surface and is expressed in barns ($1\ barn = 10^{-24} cm^2$). Another fundamental quantity is macroscopic cross section defined as:

$$\Sigma_{x,i}(E) = \sigma_{x,i}(E) N_i \tag{2.3}$$

where N_i stands for the number density of isotope i.

For a material containing different isotopes, the macroscopic cross section is defined as:

$$\Sigma_x(E) = \sum_i \Sigma_{x,i}(E) \tag{2.4}$$

2.1.2 Deriving the BTE

The transport equation is a balance equation of neutron population in a six phase volume $d^3 r dV_n d^2\Omega$ during Δt [5]:

$$\begin{aligned} \text{Change of the number of neutrons during } \Delta t = \\ & - \text{Number of neutrons leaving the volume } d^3 r \\ & - \text{Number of lost neutrons due to collisions} \\ & + \text{Number of new neutrons created} \end{aligned} \tag{2.5}$$

where:

- Change of the number of neutrons during Δt in $d^3 r dV_n d^2\Omega$ is equal to $n\left(\boldsymbol{r}, V_n, \boldsymbol{\Omega}, t+\Delta t\right) - n\left(\boldsymbol{r}, V_n, \boldsymbol{\Omega}, t\right)$
- Number of neutrons leaving the volume $d^3 r$ during Δt is $\boldsymbol{\nabla} \cdot \boldsymbol{\Omega}\phi\left(\boldsymbol{r}, V_n, \boldsymbol{\Omega}, t\right)\Delta t = \boldsymbol{\Omega} \cdot \boldsymbol{\nabla}\phi\left(\boldsymbol{r}, V_n, \boldsymbol{\Omega}, t\right)\Delta t$
- Number of lost neutrons due to collisions is $\Sigma(\boldsymbol{r}, V_n)\phi\left(\boldsymbol{r}, V_n, \boldsymbol{\Omega}, t\right)\Delta t$
- Number of new neutrons created is $Q\left(\boldsymbol{r}, V_n, \boldsymbol{\Omega}, t\right)\Delta t$, where $Q\left(\boldsymbol{r}, V_n, \boldsymbol{\Omega}, t\right)$ stands for the source density

Thus, the balance equation (2.5) can be written as:

$$\begin{aligned}\frac{n\left(\boldsymbol{r}, V_n, \boldsymbol{\Omega}, t+\Delta t\right) - n\left(\boldsymbol{r}, V_n, \boldsymbol{\Omega}, t\right)}{\Delta t} = &- \boldsymbol{\Omega} \cdot \boldsymbol{\nabla}\phi\left(\boldsymbol{r}, V_n, \boldsymbol{\Omega}, t\right) \\ &- \Sigma\left(\boldsymbol{r}, V_n\right)\left[\phi\left(\boldsymbol{r}, V_n, \boldsymbol{\Omega}, t\right)\right] \\ &+ Q\left(\boldsymbol{r}, V_n, \boldsymbol{\Omega}, t\right)\end{aligned} \tag{2.6}$$

Taking the limit $\Delta t \to 0$ the equation (2.6) becomes the differential transport equation

$$\frac{1}{V_n}\frac{\partial}{\partial t}\phi\left(\boldsymbol{r}, V_n, \boldsymbol{\Omega}, t\right) + \boldsymbol{\Omega} \cdot \boldsymbol{\nabla}\phi\left(\boldsymbol{r}, V_n, \boldsymbol{\Omega}, t\right) + \Sigma\left(\boldsymbol{r}, V_n\right)\phi\left(\boldsymbol{r}, V_n, \boldsymbol{\Omega}, t\right) = Q\left(\boldsymbol{r}, V_n, \boldsymbol{\Omega}, t\right) \tag{2.7}$$

The steady state transport equation can be written as:

$$\boldsymbol{\Omega} \cdot \boldsymbol{\nabla}\phi\left(\boldsymbol{r}, V_n, \boldsymbol{\Omega}\right) + \Sigma\left(\boldsymbol{r}, V_n\right)\phi\left(\boldsymbol{r}, V_n, \boldsymbol{\Omega}\right) = Q\left(\boldsymbol{r}, V_n, \boldsymbol{\Omega}\right) \tag{2.8}$$

Replacing V_n with the energy $E = \dfrac{mV_n^2}{2}$ equation (2.8) we get:

$$\boldsymbol{\Omega} \cdot \boldsymbol{\nabla}\phi\left(\boldsymbol{r}, E, \boldsymbol{\Omega}\right) + \Sigma\left(\boldsymbol{r}, E\right)\phi\left(\boldsymbol{r}, E, \boldsymbol{\Omega}\right) = Q\left(\boldsymbol{r}, E, \boldsymbol{\Omega}\right) \tag{2.9}$$

The steady state transport equation, due to practical and theoretical reasons, is commonly presented using lethargy u

$$\boldsymbol{\Omega} \cdot \boldsymbol{\nabla}\phi\left(\boldsymbol{r}, u, \boldsymbol{\Omega}\right) + \Sigma\left(\boldsymbol{r}, u\right)\phi\left(\boldsymbol{r}, u, \boldsymbol{\Omega}\right) = Q\left(\boldsymbol{r}, u, \boldsymbol{\Omega}\right) \tag{2.10}$$

The characteristic form of the BTE can be derived by integrating the streaming operator $\boldsymbol{\Omega} \cdot \nabla\Phi$ along a straight line of direction $\boldsymbol{\Omega}$. This integration line corresponds to particle trajectory and is called characteristic line. At time $t+s/V_n$ the particle is at $\boldsymbol{r}+s\boldsymbol{\Omega}$, where s is the position of the particle on the characteristic. $\boldsymbol{r}$ is the reference position of the particle.

$$\frac{d}{ds}\phi(\boldsymbol{r}+s\boldsymbol{\Omega},E,\boldsymbol{\Omega})+\Sigma(\boldsymbol{r}+s\boldsymbol{\Omega},E)\phi(\boldsymbol{r}+s\boldsymbol{\Omega},E,\boldsymbol{\Omega})=Q(\boldsymbol{r}+s\boldsymbol{\Omega},E,\boldsymbol{\Omega}) \tag{2.11}$$

2.1.3 Source density

The steady-state source density is utilized in lattice calculations. Assuming isotropic fission reactions in the laboratory frame of reference, the source density can be written as:

$$\begin{aligned} Q(\boldsymbol{r},E,\boldsymbol{\Omega}) = &\int_{4\pi} d^2\Omega' \int_0^\infty dE'\Sigma_s\left(\boldsymbol{r},E\leftarrow E',\boldsymbol{\Omega}\leftarrow\boldsymbol{\Omega'}\right)\phi\left(\boldsymbol{r},E',\boldsymbol{\Omega'}\right) \\ &+\frac{1}{4\pi k_{eff}}Q^{fiss}(\boldsymbol{r},E) \end{aligned} \tag{2.12}$$

where:

- the microscopic differential scattering cross section from energy E' to E and from solid angle $\boldsymbol{\Omega'}$ to $\boldsymbol{\Omega}$ is $\Sigma_s\left(\boldsymbol{r},E\leftarrow E',\boldsymbol{\Omega}\leftarrow\boldsymbol{\Omega'}\right)$
- the effective multiplication factor is k_{eff}. In steady state the production rate of neutrons due to fission must be equal to the sum of absorption and leakage rates. The adjustment of fission source is done using k_{eff} in a way to match the loss of neutrons.
- The isotropic fission source $Q^{fiss}\left(\boldsymbol{r},E\right)$ is considered to be independent of the incident neutron and can be written as:

$$Q^{fiss}(\boldsymbol{r},E)=\sum_{j=1}^{J^{fiss}}\chi_j(E)\int_0^\infty dE'\nu\Sigma_{f,j}\left(\boldsymbol{r},E'\right)\phi\left(\boldsymbol{r},E'\right) \tag{2.13}$$

  where $\chi_j(E)dE$ is the probability that the neutron which was emitted by the fissile nuclide j has the energy between E and $E+dE$. J^{fiss} stands for the total number of fissile isotopes. The macroscopic fission cross section of the j^{th} isotope is denoted as $\Sigma_{f,j}$ and ν is the number of neutrons emitted per fission. $\phi\left(\boldsymbol{r},E'\right)$ is the integral flux which is calculated via equation (2.2).

Equation (2.12) can be simplified due to the fact that the scattering cross section for isotropic media is only a function of scattering angle. Thus, equation (2.12) can be written as:

$$Q(\boldsymbol{r},E,\boldsymbol{\Omega}) = \frac{1}{2\pi}\int_{4\pi} d^2\Omega' \int_0^\infty dE' \Sigma_s\left(\boldsymbol{r},E \leftarrow E',\boldsymbol{\Omega}\cdot\boldsymbol{\Omega}'\right)\phi\left(\boldsymbol{r},E',\overrightarrow{\Omega'}\right) + \frac{1}{4\pi k_{eff}} Q^{fiss}(\boldsymbol{r},E) \tag{2.14}$$

Expanding the scattering cross section into Legendre polynomials of the order L we get:

$$\Sigma_s\left(\boldsymbol{r},E \leftarrow E',\boldsymbol{\Omega}\cdot\boldsymbol{\Omega}'\right) = \sum_{l=0}^{L} \frac{2l+1}{2} \Sigma_{s,l}\left(\boldsymbol{r},E \leftarrow E'\right) P_l\left(\boldsymbol{\Omega}\cdot\boldsymbol{\Omega}'\right) \tag{2.15}$$

where the Legendre moments are $\Sigma_{s,l}\left(\boldsymbol{r},E \leftarrow E'\right)$.

Using spherical harmonics of the flux equation (2.14) transforms into:

$$Q(\boldsymbol{r},E,\boldsymbol{\Omega}) = \frac{1}{4\pi}\left[\int_0^\infty dE' \sum_{l=0}^{L}(2l+1)\Sigma_{s,l}\left(\boldsymbol{r},E \leftarrow E'\right) \sum_{m=-l}^{l} R_l^m(\boldsymbol{\Omega})\phi_l^m\left(\boldsymbol{r},E'\right) + \frac{1}{k_{eff}} Q^{fiss}(\boldsymbol{r},E)\right] \tag{2.16}$$

where $\phi_l^m(\boldsymbol{r},E) = \int_{4\pi} d^2\Omega R_l^m(\boldsymbol{\Omega})\phi(\boldsymbol{r},E,\boldsymbol{\Omega})$

For those cases where the scattering in the laboratory system is isotropic, equation (2.16) simplifies to:

$$Q(\boldsymbol{r},E) = \frac{1}{4\pi}\left[\int_0^\infty dE \Sigma_{s,0}\left(\boldsymbol{r},E \leftarrow E'\right)\phi\left(\boldsymbol{r},E'\right) + \frac{1}{k_{eff}} Q^{fiss}(\boldsymbol{r},E)\right] \tag{2.17}$$

2.1.4 Boundary conditions

Boundary conditions are required to solve the BTE. Let's take a domain V which contains moving particles and the boundary conditions are enacted on the surrounding ∂V boundary. At each point $\boldsymbol{r}_S \in \partial V$ one can associate an outward normal $\boldsymbol{N}(\boldsymbol{r}_s)$. To solve the BTE inside volume V one needs to know the angular flux $\phi(\boldsymbol{r}_s,E,\boldsymbol{\Omega})$ at $\boldsymbol{\Omega}\cdot\boldsymbol{N}(\boldsymbol{r}_s) < 0$ (incoming flux). Common approach is to relate the unknown incoming flux with the know outgoing one, which is called the albedo boundary condition and is written as:

$$\phi\left(\boldsymbol{r}_s,E,\boldsymbol{\Omega}\right) = \beta\phi\left(\boldsymbol{r}_s,E,\boldsymbol{\Omega}'\right) \quad \text{with } \boldsymbol{\Omega}\cdot\boldsymbol{N}\left(\boldsymbol{r}_s\right) < 0 \tag{2.18}$$

where $\boldsymbol{\Omega}'$ is the direction of the outgoing particle and albedo β stands for the boundary condition. $\beta = 1$ represents the reflective boundary condition. $\beta = 0$ represents the vacuum boundary condition.

The white boundary condition is a special reflective condition where the leaving particles return back with an isotropic angular distribution:

$$\phi\left(\boldsymbol{r}_s, E, \boldsymbol{\Omega}\right) = \frac{1}{\pi} \int_{\boldsymbol{\Omega}' \cdot \boldsymbol{N}(\boldsymbol{r_s}) > 0} d^2\Omega' [\boldsymbol{\Omega}' \cdot \boldsymbol{N}(\boldsymbol{r}_s)] \phi\left(\boldsymbol{r}_s, E, \boldsymbol{\Omega}'\right) \quad \text{with } \boldsymbol{\Omega} \cdot \boldsymbol{N}\left(\boldsymbol{r}_s\right) < 0 \tag{2.19}$$

Periodic boundary condition represents the equality of the flux on parallel boundaries in a periodic lattice. For a periodic lattice with a pitch of $\boldsymbol{\Delta r}$ the boundary condition can be written as:

$$\phi\left(\boldsymbol{r}_s, E, \boldsymbol{\Omega}\right) = \phi\left(\boldsymbol{r}_s + \boldsymbol{\Delta} r, E, \boldsymbol{\Omega}\right) \tag{2.20}$$

2.1.5 Multi-group discretization

To be able to solve the BTE numerically one needs to apply multi-group energy discretization over it. The discretization is carried out by dividing the energy axis into G energy groups and condensing all energy dependent parameters into those groups. In each of those groups the neutrons are viewed as one-speed particles. The energy groups can be presented using energy E or lethargy u variables as:

$$W_g = \{E; E_g \leq E \leq E_{g-1}\} = \{u; u_{g-1} \leq u \leq u_g\}; \quad g = 1, G \tag{2.21}$$

where the maximum energy of the neutron is denoted as E_0. The differential form of the multi-group BTE is written as:

$$\boldsymbol{\Omega} \cdot \boldsymbol{\nabla} \phi_g(\boldsymbol{r}, \boldsymbol{\Omega}) + \Sigma_g(\boldsymbol{r}) \phi_g(\boldsymbol{r}, \boldsymbol{\Omega}) = Q_g(\boldsymbol{r}, \boldsymbol{\Omega}) \tag{2.22}$$

The group-average values of the flux and the source are defined as:

$$\begin{aligned} \phi_g(\boldsymbol{r}, \boldsymbol{\Omega}) &= \int_{u_{g-1}}^{u_g} \phi(\boldsymbol{r}, u, \boldsymbol{\Omega}) du \\ Q_g(\boldsymbol{r}, \boldsymbol{\Omega}) &= \int_{u_{g-1}}^{u_g} Q(\boldsymbol{r}, u, \boldsymbol{\Omega}) du \end{aligned} \tag{2.23}$$

The multi-group characteristic form of the BTE is given by:

$$\frac{d}{ds}\phi_g(\boldsymbol{r}+s\boldsymbol{\Omega},\boldsymbol{\Omega})+\Sigma_g(\boldsymbol{r}+s\boldsymbol{\Omega})\phi_g(\boldsymbol{r}+s\boldsymbol{\Omega},\boldsymbol{\Omega})=Q_g(\boldsymbol{r}+s\boldsymbol{\Omega},\boldsymbol{\Omega}) \tag{2.24}$$

The integral form of the transport equation is:

$$\phi_g(\boldsymbol{r},\boldsymbol{\Omega})=\int_0^\infty ds e^{-\tau_g(s)}Q_g(\boldsymbol{r}-s\boldsymbol{\Omega},\boldsymbol{\Omega}) \tag{2.25}$$

where $\tau_g(s)=\int_0^s ds'\Sigma_g(\boldsymbol{r}+s'\boldsymbol{\Omega})$ is the optical path.

2.2 Solving the BTE

In the previous section we derived the BTE in multiple forms. Even with multi-group energy discretization, the BTE cannot be solved analytically for the real-world problems. Numerical methods are used to treat the angular variable. There are two main methods which can be used to solve the BTE: stochastic method and deterministic method. Below we present stochastic and deterministic methods and relevant computational codes which were used in this research.

2.2.1 Monte-Carlo Method

Monte-Carlo method, also known as stochastic method, use sequence of random numbers to simulate the random events which are happening to each particle history. Millions of particle histories are simulated using continuous energy or multi-group representation of the cross sections within the specific domain to achieve a sufficient accuracy. The calculation times can become very long due to large number of particle histories.

This method is the most accurate and is mostly used as a validation and benchmarking tool for deterministic methods. In this study, SERPENT2 Monte-Carlo code was used to generate the reference results needed to validate deterministic DRAGON5 lattice code calculations [6].

Stochastic method has the advantage of solving any complex problem which cannot be solved using deterministic methods. The computed quantities are provided with standard deviations which clearly indicate their statistically accuracy.

2.2.2 Deterministic Methods

Deterministic methods are based on discretization of BTE in each of its phase space variables. Discretization of BTE results in a typically large system of coupled algebraic equations. This system of equations is then solved numerically using efficient algorithms and acceleration techniques. There are a few well known deterministic methods which are

- the methods of characteristics - MOC
- the collision probability method - CP
- the interface current method - IC
- the discrete ordinates method - DO
- the method of spherical harmonics

In this research only MOC, CP and IC methods were used.

2.2.3 Collision probability (CP) Method

The CP method is the outcome of the spatial discretization of the integral form of the multi-group BTE. Spatial discretization is possible to perform on an infinite domain or a finite domain were the boundary conditions are imposed on the outer surface of that domain. The derivation presented here will use infinite lattice of assemblies. Substituting $\boldsymbol{r} - s\boldsymbol{\Omega}$ with $\boldsymbol{r'}$ in equation (2.24) and integrating it over the solid angle, a new form of the transport equation is derived:

$$\begin{aligned}\phi_g(\boldsymbol{r}) = \int_{4\pi} d^2\Omega \phi_g(\boldsymbol{r}, \boldsymbol{\Omega}) &= \frac{1}{4\pi} \int_{4\pi} d^2\Omega \int_0^{\infty} ds e^{-\tau_g(s)} Q_g(\boldsymbol{r} - s\boldsymbol{\Omega}) \\ &= \frac{1}{4\pi} \int_{\infty} d^3 r' \frac{e^{-\tau_g(s)}}{s^2} Q_g\left(\boldsymbol{r'}\right)\end{aligned} \tag{2.26}$$

Then the assembly is split into volumes V_i. In each of the region V_i the sources of secondary neutrons are assumed to be uniform and equal to $Q_{i,j}$. V_i^{∞} is the infinite set of V_i volumes belonging to all the assemblies in the lattice. By multiplying equation (2.26) with $\Sigma_g(\boldsymbol{r})$ and integrating over each volume V_i we get:

$$\int_{V_j} d^3 r \Sigma_g(\boldsymbol{r}) \phi_g(\boldsymbol{r}) = \frac{1}{4\pi} \int_{V_j} d^3 r \Sigma_g(\boldsymbol{r}) \sum_i Q_{i,g} \int_{V_i^{\infty}} d^3 r' \frac{e^{-\tau_g(s)}}{s^2} \tag{2.27}$$

Equation (2.27) can be written as:

$$\phi_{j,g} = \frac{1}{V_j} \Sigma_{j,g} \sum_i Q_{i,g} V_i P_{ij,g} \tag{2.28}$$

where:

$$\phi_{j,g} = \frac{1}{V_j} \int_{V_j} d^3 r \phi_g(\boldsymbol{r}) \tag{2.29}$$

$$\Sigma_{j,g} = \frac{1}{V_j \phi_{j,g}} \int_{V_j} d^3 r \Sigma_g(\boldsymbol{r}) \phi_g(\boldsymbol{r}) \tag{2.30}$$

$$P_{ij,g} = \frac{1}{4\pi V_i} \int_{V_i^\infty} d^3 r' \int_{V_j} d^3 r \Sigma_g(\boldsymbol{r}) \frac{e^{-\tau_g(s)}}{s^2} \tag{2.31}$$

$P_{ij,g}$ is called the collision probability (CP) and presents the probability of a new born neutron from volume V_i to undergo a collision in the volume V_j of the assembly. Assuming that the total cross section $\Sigma_{j,g}$ in the volume V_j is constant, the reduced CPs can be written as:

$$p_{ij,g} = \frac{P_{ij,g}}{\Sigma_{j,g}} = \frac{1}{4\pi V_i} \int_{V_i^\infty} d^3 r' \int_{V_j} d^3 r \frac{e^{-\tau_g(s)}}{s^2} \tag{2.32}$$

Reduced CPs satisfy the reciprocity and conservation properties

$$p_{ij,g} V_i = p_{ji,g} V_j \tag{2.33}$$

$$\sum_j p_{ij,g} \Sigma_{j,g} = 1; \forall i \tag{2.34}$$

Equation (2.28) can be rewritten using reduced CPs and the reciprocity property as:

$$\phi_{j,g} = \sum_j Q_{j,g} p_{ij,g} \tag{2.35}$$

To numerically calculate the CPs the following steps are performed. First, the angular domain is split into m number of tracks with direction $\boldsymbol{\Omega}_m$ and weight ω_m so that $\int_0^{4\pi} d^2\Omega = \sum_m \omega_m \boldsymbol{\Omega}_m = 4\pi$. For each of $\boldsymbol{\Omega}_m$ direction a normal plane is created and divided into uniform grid with integration points $\boldsymbol{p}_{m,n}$ and weights $\Pi_{m,n}$. The tracking is the discretization with integration lines and points. Then, the numerical integration is performed using the tracking information and the macroscopic total cross sections of each region. Equation (2.32) after discretization has the following form:

$$
\begin{aligned}
p_{ij,g} = \frac{1}{\Sigma_i \Sigma_j V_i} \sum_m \omega_m \sum_n \Pi_{m,n} \\
\sum_k \delta_{i,V_k} \sum_h \delta_{j,V_h} \quad \left[1 - e^{-\Sigma_i L_k}\right] e^{-\tau_{k,h}} \left[1 - e^{-\Sigma_j L_h}\right]
\end{aligned}
\tag{2.36}
$$

where L_k represents the distance crossed in the volume V_k of a neutron born at the point $\boldsymbol{p}_{m,n}$ and moving in direction $\boldsymbol{\Omega}_m$.

2.2.4 Method of Characteristics (MOC)

The Method of Characteristics (MOC) is a well-known technique for solving partial differential equations and particularly can be used to solve the BTE [7]. The MOC is based on an iterative calculation of the neutron flux by solving the characteristic form of the transport equation over tracks crossing the complete domain [8].

The MOC is based on discretization of equation (2.24) along the particle paths and integration of the flux using

$$
\begin{aligned}
V_j \phi_{j,g} &= \int_{V_j} d^3 r \int_{4\pi} d^2 \boldsymbol{\Omega} \; \phi_g(\boldsymbol{r}, \boldsymbol{\Omega}) \\
&= \int_{\Upsilon} d^4 T \int_{-\infty}^{\infty} ds \; \chi_{V_j}(\boldsymbol{T}, s) \; \phi_g(\boldsymbol{p} + s\boldsymbol{\Omega}, \boldsymbol{\Omega})
\end{aligned}
\tag{2.37}
$$

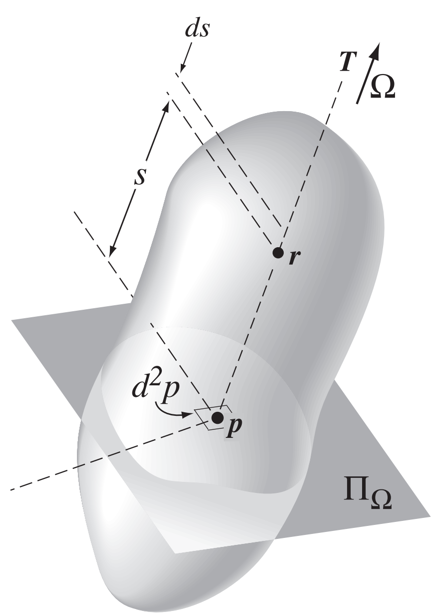

Figure 2.1 Spacial integration domain.

where

$V_j, j = 1, J$ - small volume, obtained after partitioning the spacial volume into J regions where each region has uniform nuclear properties

$\phi_{j,g}$ - average flux in region j of energy group g

$\Upsilon = \{\boldsymbol{T}\}$ - the tracking domain

$\boldsymbol{T}$ - single characteristic determined by its orientation $\boldsymbol{\Omega}$, weight $\boldsymbol{\omega_T}$ and starting point $\boldsymbol{p}$ defined on a reference plane $\boldsymbol{\Pi_\Omega}$

$\boldsymbol{\Pi_\Omega}$ - reference plane perpendicular to $\boldsymbol{T}$, shown in Figure 2.1

$\chi_{V_j}(\boldsymbol{T}, s)$ - characteristic function which is equal to one when characteristic $\boldsymbol{T}$ passes through V_j and zero otherwise.

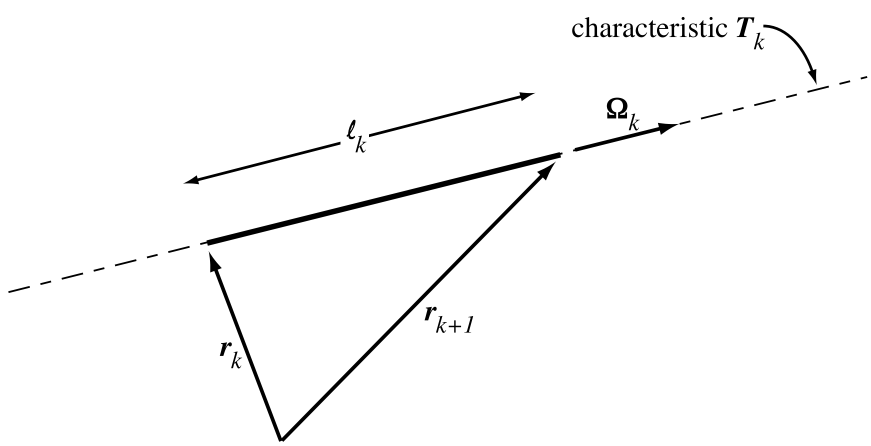

Figure 2.2 A segment of a single characteristic

The MOC method needs to know the region index N_k and segment length l_k which described the crossing of characteristic $\boldsymbol{T}$ with the domain (Figure 2.2). This information is presented as $N_k, l_k; k = 1, K$ where K stands for the total number of intersections of regions with $\boldsymbol{T}$. The intersection points of $\boldsymbol{T}$ with region boundaries and the corresponding angular fluxes at those boundaries are defined as

$$\begin{aligned} \boldsymbol{r}_{k+1} &= \boldsymbol{r}_k + \ell_k \boldsymbol{\Omega}; \quad k = 1, K \\ \phi_g^k(\boldsymbol{T}) &= \phi_g\left(\boldsymbol{r}_k, \boldsymbol{\Omega}\right); \quad k = 1, K+1 \end{aligned} \tag{2.38}$$

Assuming a flat source approximation $(\forall s \in [0, \ell_k], Q_g(\boldsymbol{r} + s\boldsymbol{\Omega}, \boldsymbol{\Omega}) = Q_g^{N_k}(\boldsymbol{\Omega}.)$ and a constant total cross section in each region $(\forall s \in [0, \ell_k], \Sigma_g(\boldsymbol{r} + s\boldsymbol{\Omega}) = \Sigma_g^{N_k})$ and defining the optical path as $\tau_k = \Sigma_g^{N_k}\ell_k$, the equation (2.24) can be evaluated to obtain the following relation between incoming and outgoing angular flux:

$$\phi_g^{k+1}(\boldsymbol{T}) = \phi_g^{k}(\boldsymbol{T})e^{-\tau_k} + \frac{1-e^{-\tau_k}}{\Sigma_g^{N_k}} Q_g^{N_k}(\boldsymbol{T}) \tag{2.39}$$

Assuming that incoming angular flux is known on the boundaries of the domain and integrating equation (2.39) over each segment and angle, the flux can be written as:

$$\phi_{j,g} = \frac{Q_{j,g}}{\Sigma_j} - \frac{1}{\Sigma_{j,g}V_j}\sum_T \omega_T \sum_k \delta_j^{N_k}\left(\phi_g^{k+1} - \phi_g^{k}\right) \tag{2.40}$$

2.2.5 Comparison of CP and MOC Methods

The MOC has the advantage of using the same tracking information as the CP method.

CP method has two major limitations: (1) for a problem containing N regions, the CP method produces square matrices of the order equal to N thus cannot be applied to large domains and (2) the CP method is limited to isotropic sources in the laboratory system. On the contrary, for a problem containing N regions and M surfaces the MOC method requires only $N + M$ equations to be solved. Furthermore, the MOC method can be extended to handle linearly anisotropic sources in the laboratory system and further accelerated using different acceleration methods [9], [10].

2.3 Computational Schemes

Single level computational schemes require long computational times when used with a detailed energy mesh and fine spacial discretization. Therefore, multilevel schemes were introduced aiming to reduce computational time by decreasing the number of groups utilized in the flux calculation. In a way, multilevel schemes offer a balance between a certain degree of accuracy and computational time.

Recent developments in DRAGON5 show the viability of a two-level scheme, proposed by Canbakan, which is based on Method of Characteristics (MOC) and optimized for the SHEM295 energy mesh [2]. Here, we present a detailed description of the one-level and two-level schemes used in our calculations with DRAGON5.

2.3.1 One-Level Computational Scheme

The one level computational scheme is applied to pincells benchmarks and to reference assembly calculations. In the latter case, a different solution of the BTE is used for the resonance self-shielding and for the flux calculation. The flow chart of the one-level scheme is depicted in Figure 2.3. Its DRAGON5 implementation is depicted in Figure 2.4.

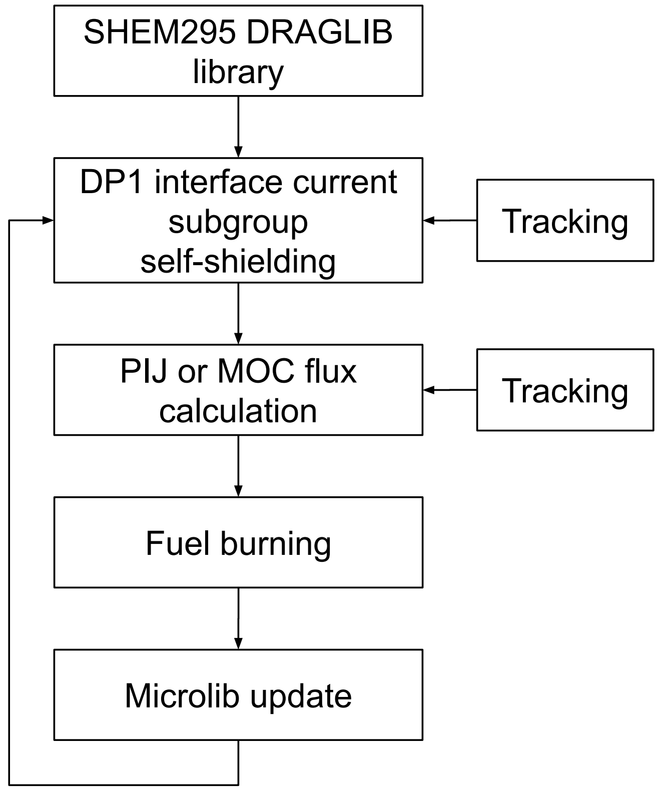

Figure 2.3 One-level computational scheme flow chart

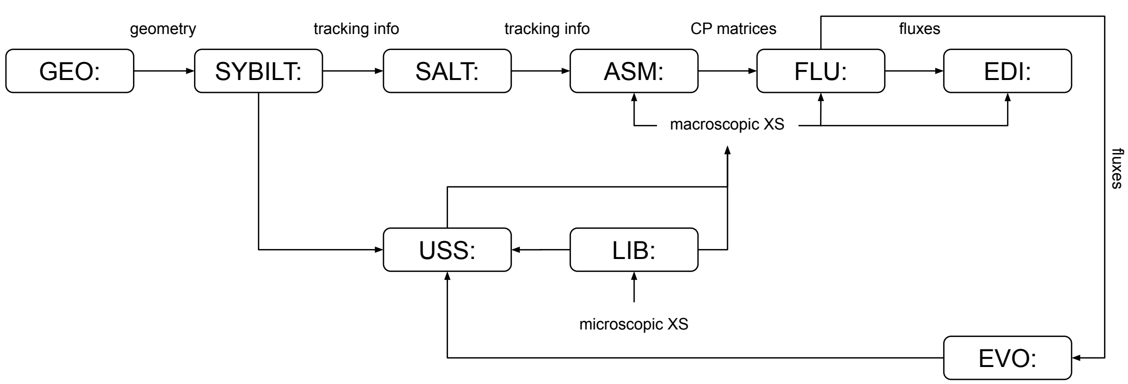

Figure 2.4 One-level computational scheme implementation in DRAGON5

The one-level computational scheme is based on the introduction of two geometries (and corresponding trackings):

1. A self-shielded geometry is defined to be used with the IC method. At the self-shielding step, there is no need to submesh moderator regions and some fuel regions can be merged together to save CPU costs.

2. A flux-solution geometry is defined to be used for the BTE solution with the PIJ or MOC method. At the BTE solution step, the *windmill discretization*, depicted in Figure 2.5 for the case of a standard PWR assembly, is recommended and used in this study. [2] The windmill discretization is based on the *TDT surfacic model* [11], and can be generated in DRAGON5 as depicted in Figure 2.6. The discretization in Figure 2.5 features an explicit *water gap* on the right, useful for computing *assembly discontinuity factors* or for performing *Selengut normalization* of few-group cross sections [12].

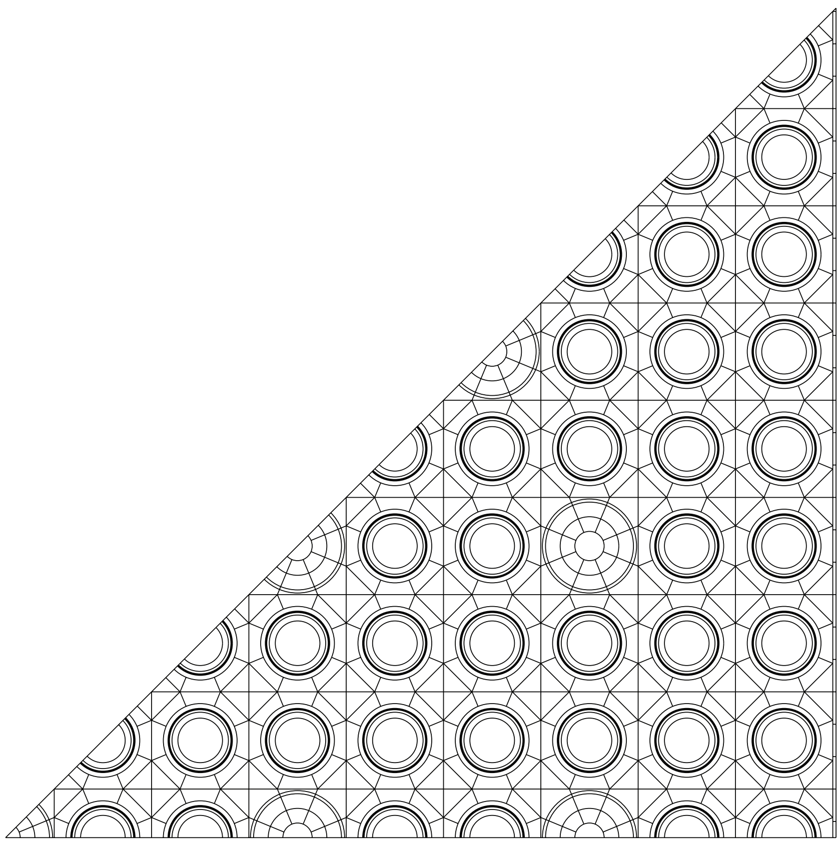

Figure 2.5 Windmill discretization of a PWR assembly.

The one-level computational scheme is implemented as follows:

1. The isotopic content of the pincell or assembly is recovered from a cross-section library in DRAGLIB format. We used a SHEM295 energy mesh designed with a resonance

Figure 2.6 Generation of a windmill geometry.

self-shielding cutoff located at 4.63 eV. All energy groups below 4.63 eV are finely discretized according to the Santamarina-Hfaiedh recommendation. [13] Above 4.63 eV, the energy group widths are coarser, but are kept sufficiently narrow to allow using a resonance self-shielding processing based on the subgroup method with mathematical probability tables. [14] It is important to note that the original SHEM281 energy mesh is *not* compatible with a subgroup method with mathematical probability tables.

2. The self-shielding calculation is a solution of the Livolant-Jeanpierre equation for each resonant isotope present in the lattice, as described in Section 4.2.3 of Ref. [5]. This equation is written

$$\boldsymbol{\Omega} \cdot \boldsymbol{\nabla} \varphi(\boldsymbol{r}, u, \boldsymbol{\Omega}) + \Sigma(\boldsymbol{r}, u) \varphi(\boldsymbol{r}, u, \boldsymbol{\Omega}) = \frac{1}{4\pi} \left[\Sigma_{\rm s}^{+}(\boldsymbol{r}, u) + \mathcal{R}^{*}\{\varphi(\boldsymbol{r}, u)\} \right] \tag{2.41}$$

where

$\varphi(\boldsymbol{r}, u, \boldsymbol{\Omega}) =$ fine structure function describing the resonant behavior of the flux as a function of space, lethargy and angle.

$\Sigma(\boldsymbol{r}, u) =$ macroscopic total cross section, a resonant function of the lethargy.

$\Sigma_{\rm s}^{+}(\boldsymbol{r}, u) =$ macroscopic scattering cross section of the non-resonant isotopes.

$\mathcal{R}^{*}\{\varphi(\boldsymbol{r}, u)\} =$ slowing-down operator for the resonant isotope, acting over a short lethargy range.

Equation (2.41) is a source equation that is defined only over resonant energy groups. The idea behind the subgroup method is to replace Riemann integrals in lethargy with Lebesgue integrals and to replace any probability density with a mathematical probability table.

For pin-cells calculations, equation (2.41) can be solved with a collision probability (PIJ) approach (keyword `PIJ`). However, for PWR assemblies, constructing a full PIJ matrix, even using the interface current (IC) method, leads to prohibitive CPU costs. The recommended approach in this case is to use the IC method with a *flux-current* iteration (keyword `ARM`), avoiding the reconstruction of the full PIJ matrix.

3. The main solution step of the BTE is obtained with the collision probability (PIJ) or with the method of characteristics (MOC) approach. The former option is recommended for pincell cases and the MOC is recommended for assembly calculations. In the assembly case, we recommend using different geometries (and different trackings) for the solution of the Livolant-Jeanpierre equation (2.41) and for the solution of the BTE.

   BTE solution is an eigenvalue problem. It can be of two types:

   `TYPE K`: The eigenvalue is the effective multiplication factor K_{eff} for a fixed value of the buckling B^2, generally set to zero. In this study, we chose this option with $B^2 = 0$, in order to facilitate comparisons with reference Monte Carlo calculations.

   `TYPE B`: The eigenvalue is the buckling B^2 for a fixed value of the K_{eff}, generally set to one. A leakage model must be introduced to converge on a leakage rate in each energy group and on the lattice buckling. The *homogeneous* B_1 model is generally used. Heterogeneous models are also available to take streaming effects into account. [5]

4. A solution of the Bateman equations is provided in the `EVO:` module of DRAGON5, as described in Section 4.5 of Ref. [5]. The microlib is updated and a new self-shielding calculation may be performed (or not) before the new solution of the BTE. Self-shielding calculation is repeated for 9 or 10 burnup step values only. The burnup steps, at which the Bateman equation is solved, are predefined in each computational scheme. They are different for standard and gadolinium-poisoned pincells or assemblies.

5. Remaining steps are not represented in Figure 2.3. They are the edition steps in modules `EDI:` and `COMPO:` to produce few-group cross sections to be used in the full-core simulation code. Also, perturbation branching calculations can be performed around some nominal burnup values for neighbouring local parameters variations (fuel temperature, coolant density, boron concentration in water, etc.). We did not consider local parameter perturbations in this study.

2.3.2 Two-Level Computational Scheme

Two-level computational schemes represent the state-of-the-art in reactor physics. They are already implemented for production use in industrial codes such as APOLLO2 and CASMO5. [15, 16] In the case of APOLLO2 with a REL-2005 scheme, the SHEM281 mesh (281 groups) is used with self-shielding cutoffs around 22.5 eV. The interface current method with DP1 development of the interface currents is used for both self-shielding and first-level flux calculation. The self-shielding calculation is based on the Sanchez-Coste equivalence technique. The first level ends with a step of condensation of the cross sections on the energy grid of the second level, coupled with a calculation of non-converged SPH factors. In order to mitigate convergence issues, the REL-2005 scheme performs a unique fixed-point SPH iteration. The second-level flux calculation is based on the MOC.

In the case of CASMO5, 586 groups are used with a cutoff of self-shielding around 6 eV. A self-shielding calculation and a first-level flux calculation are performed on this fine multi-group mesh. This flux calculation is based on an approximate spatial discretization of the neutron transport equation, in order to minimize the calculation time. The second-level flux calculation is based on the MOC.

The two-level computational scheme we used in this study for assembly cases is similar to the Canbakan scheme introduced in Ref. [2]. Since its proposal in 2015, all computational capabilities required to implement this scheme in detail were committed in DRAGON5. The two-level computational scheme is based on the introduction of three geometries, two sets of isotopic mixtures and two energy meshes. The flow chart of the two-level scheme is depicted in Figure 2.7. Its DRAGON5 implementation is depicted in Figure 2.8.

Two sets of isotopic mixtures, each with specific isotopic concentrations, are defined:

1. *First-level mixtures* are used for self-shielding and first-level BTE solution with the IC method.

2. *Second-level mixtures* are used for the second-level BTE solution with the MOC method and Bateman equation solution.

Typical values for the number of first- and second-level mixtures are given in Table 2.1.

Table 2.1 Number of first- and second-level mixtures

Case	# of Gd pins in 1/8 of assembly	# of first-level mixtures	# of second-level mixtures
ASSBLY-A	0	37	161
ASSBLY-B	1	39	163
ASSBLY-C	1.5	41	165
ASSBLY-D	3	47	171

Three geometries (and corresponding trackings) are defined:

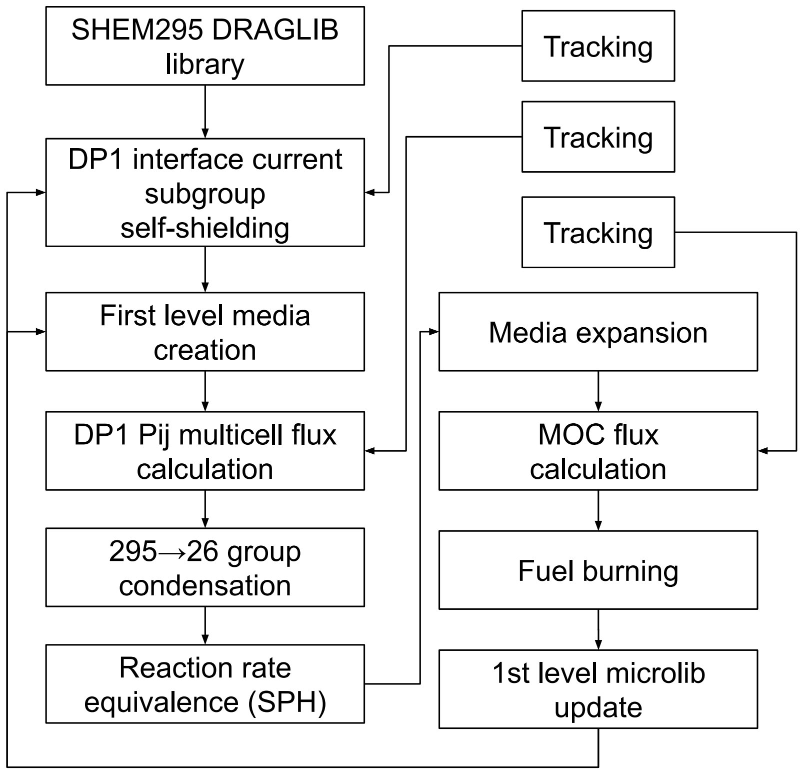

Figure 2.7 Two-level computational scheme flow chart

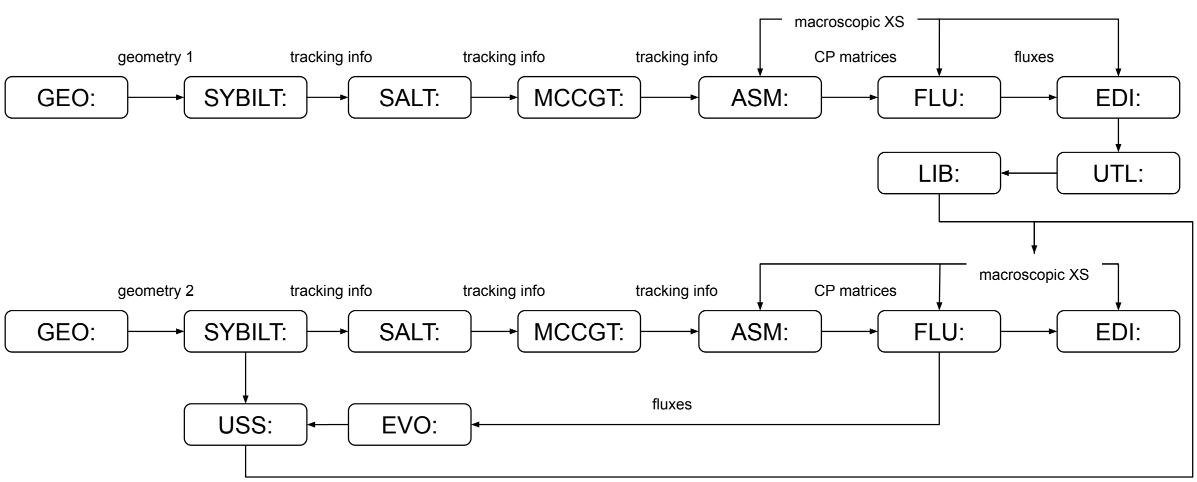

Figure 2.8 Two-level computational scheme implementation in DRAGON5

1. A self-shielded geometry is defined to be used with the IC method. This geometry is similar to the self-shielded geometry used by the one-level scheme. At the self-shielding

step, there is no need to submesh moderator regions and some fuel regions can be merged together to reduce CPU costs.

2. A first-level geometry is defined to be used for the BTE solution with the IC method. This geometry is similar to the self-shielded geometry with a better discretization of moderator regions.

3. A second-level geometry is defined to be used for the BTE solution with the MOC method. A *windmill discretization* of the geometry is used, as proposed for the one-level BTE solution with MOC.

Many steps of the two-level scheme are similar to those of the one-level scheme. The two-level computational scheme is implemented as follows:

1. The isotopic content of the pincell or assembly is recovered from a cross-section library in DRAGLIB format. Isotopic content is defined for a limited set of *first-level mixtures*.

2. A resonance self-shielding calculation is performed with the subgroup method over 295 energy groups and for a limited set of *first-level mixtures*. Self-shielding calculation repeated for 9 or 10 burnup step values only.

3. If the Bateman equations were solved in the previous burnup step, the isotopic concentrations are different in each second-level mixture. Take the average of these isotopic concentrations over the first-level mixtures and recompute the lattice macrolib over the first-level energy mesh and mixtures.

4. Solve the BTE with the interface current (IC) approach over the first-level energy mesh and mixtures.

5. Perform a condensation of first-level cross sections over the second-level energy mesh (from 295 to 26 energy groups in our case).

6. Perform a SPH equivalence over 26g cross sections to preserve reference reaction rates obtained with the 295g calculation. Here, an IC macro-calculation is used. SPH iterations are converged with a fixed-point strategy. Groups 23 to 26 are not SPH-corrected in the gadolinium assemblies. The reason is that at some burnup steps there are too few neutrons in these energy groups for the fixed-point iterations to converge. SPH factors in these groups are equal to one.

7. Perform an expansion of the microlib from the first-level mixture definition to the second-level mixture definition. Here, a simple duplication of 26g microscopic cross sections are used. The `MultLIBEQ.c2m` CLE-2000 procedure of the Canbakan scheme is used.

8. Solve the BTE with the method of characteristics (MOC) approach over the second-level energy mesh and mixtures.

9. Solve the Bateman equations over the second-level mixtures, as described for the one-level scheme.

CHAPTER 3 VALIDATION STUDY

Three PWR pin cells and four PWR assemblies case of the benchmark suit are validated by comparing simulation results of deterministic lattice transport and Monte Carlo codes. In deterministic calculations we used one eighth of assembly geometry due to its symmetries. However, in stochastic calculations an entire assembly geometry was used. Here we perform deterministic calculations using two-level (2L) and one-level (1L) schemes and validate it against Monte Carlo calculations.

This chapter consists of three main sections. The first section presents the calculation codes used for validation. The second section provides detailed description of the benchmark used. Finally, in the third section, comparison of all 7 test cases of the benchmark suit are presented.

3.1 Computer Codes

Validation study was conducted using DRAGON5 deterministic lattice code and SERPENT2 stochastic Monte Carlo code. The two simulation tools are discussed below in Sections 3.1.1 and 3.1.2.

3.1.1 The DRAGON5 Lattice Code

DRAGON lattice code is being developed at Polytechnique Montréal since 1991 under GNU Lesser General Public License. It can be installed on all operating systems which support Fortran. The project contains multiple calculation methods and numerical techniques which can be used to solve the BTE. DRAGON5 code has a modular design which allow easy addition and removal of calculation modules without side effects.

DRAGON5 is capable to perform all the tasks that can be associated with a lattice code [17], such as

- load and interpolate microscopic cross sections provide by standard libraries
- perform resonance self-shielding calculations
- perform multi-group neutron flux calculations with and without leakage
- perform transport-transport or transport-diffusion equivalence calculations
- perform isotopic depletion calculations

DRAGON5 can execute 1D, 2D and 3D calculations using MOC, CP, DO methods [5].

3.1.2 The SERPENT2 Monte Carlo Code

SERPENT2 is a versatile multi-dimensional continuous-energy Monte Carlo code for reactor physics simulations [4]. It is capable to perform burnup calculations via its builtin subroutines. Serpent is a perfect tool to be used for academic research. The academic research fields covered by Serpent are:

- generation of group constants
- studies of fuel cycle
- modeling of research and GenIV reactors
- coupled multi-physics calculations

Due to continuous-energy Monte Carlo method, SERPENT2 can perform reactor physics calculations in complex geometries without significant approximations.

SERPENT2 can perform reactor physics calculations in complex geometries with few approximations. These are related to the limited statistic of the simulated neutron population, to the numerical solution of the Bateman equations, to the cross-section accuracies and to the self-shielding model at unresolved resonance energies.

3.2 Benchmark Description

To validate lattice code accuracy for PWR applications a special benchmark was used. This benchmark was designed for validations of typical PWR cores in depletion conditions. It consists of three fuel pin-cells and four 17 by 17 assemblies. The 3 fuel pins and 4 assemblies have different fuel compositions. All of the 7 test cases have the same material compositions for moderator, cladding and the gap as provided in Table 3.1. In all benchmark problems the average discharge burnup is assumed to be 70 GWd/t. This value presents the target discharge burnup of the next-generation fuels [18].

The fuel rods inside pin and assembly cells were split into several rings. This implementation allows accurate estimation of absorption in major isotopes [19]. Specifically, UOX fuel rods were split into 4 rings and Gd rods into 6 rings with the volume fractions listed in Table 3.2. The pin-cell geometry is shown in Figure 3.1. Fuel rod rings are shown in Figure 3.2.

The radii of pin and assembly cells are listed in Table 3.3 where both pin and assembly cells have square geometries with a side of 1.26 cm.

Table 3.1 Material compositions for moderator, cladding and gap

Material	Index[a]	Isotope	Number density 10^{24} nuclide/cm^3	Temperature K
moderator	1	^{16}O	2.34793×10^{-2}	600
		^{1}H in H_2O	4.69585×10^{-2}	
		^{10}B	5.53089×10^{-6}	
		^{11}B	2.18498×10^{-5}	
clad	2	^{90}Zr	2.165762×10^{-2}	600
		^{91}Zr	4.72300×10^{-3}	
		^{92}Zr	7.219212×10^{-3}	
		^{94}Zr	7.316029×10^{-3}	
		^{96}Zr	1.178642×10^{-3}	
gap	3	^{16}O	3.76439×10^{-6}	600

[a] Column values correspond to region numbers in Figure 3.1

Table 3.2 Volume fractions of UOX and Gd fuel rods

Ring	UO_2 %/*vol*	$UO_2Gd_2O_3$ %/*vol*
A	50	20
B	30	20
C	15	20
D	5	20
E		15
F		5

The 17×17 assembly with a pitch of 21.504 cm is surrounded by a water blade of 0.042 cm. The burnup steps used for depletion calculations in UOX benchmarks is given in Table 3.4. Specifically, for Gd fuel benchmarks a refined burnup grid is used as given in Table 3.5. In all benchmarks the power for depletion calculations is normalized to 39 W/gU.

There are three square pin-cell test cases referred in this document as PIN-A, PIN-B and PIN-C. Geometry of these pin-cells is the same for all cases and is shown in Figure 3.1.

Table 3.3 Pin-cell and assembly cell radii

type	radius
radius of	cm
fuel pellet	0.4096
inner clad	0.4180
outer clad	0.4750
inner guide tube	0.5605
outer guide tube	0.6225
instrumentation inner tube	0.5725
instrumentation outer tube	0.6225

Table 3.4 Burnup steps in GWd/t used in UOX benchmarks

0.0	0.03	0.05	0.075	0.15	0.25	0.5	0.75	1.0	2.0
2.5	3.0	3.5	4.0	4.5	5.0	5.5	6.0	6.5	7.0
7.5	8.0	8.5	9.0	9.5	10.0	11.0	12.0	13.0	14.0
15.0	16.0	17.0	18.0	19.0	20.0	22.0	24.0	26.0	28.0
30.0	32.0	34.0	36.0	38.0	40.0	42.0	44.0	46.0	48.0
50.0	52.0	54.0	56.0	58.0	60.0	62.0	64.0	66.0	68.0
70.0									

Material composition are provided in Table 3.6.

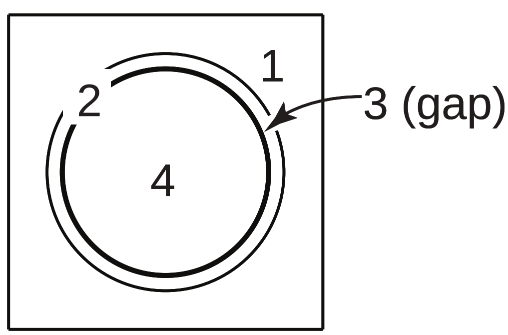

Figure 3.1 Numbered material regions in a pin-cell geometry

Table 3.5 Burnup steps in GWd/t used in Gd benchmarks

0.0	0.015	0.03	0.05	0.075	0.1125	0.15	0.2	0.25	0.375
0.5	0.625	0.75	0.875	1.0	1.25	1.5	1.75	2.0	2.25
2.5	2.75	3.0	3.25	3.5	3.75	4.0	4.25	4.5	4.75
5.0	5.25	5.5	5.75	6.0	6.25	6.5	6.75	7.0	7.25
7.5	7.75	8.0	8.25	8.5	8.75	9.0	9.25	9.5	9.75
10.0	10.25	10.5	10.75	11.0	11.25	11.5	11.75	12.0	12.25
12.5	12.75	13.0	13.25	13.5	13.75	14.0	14.25	14.5	14.75
15.0	15.25	15.5	16.0	16.5	17.0	17.5	18.0	18.5	19.0
19.5	20.0	20.5	22.0	24.0	26.0	28.0	30.0	32.0	34.0
36.0	38.0	40.0	42.0	44.0	46.0	48.0	50.0	52.0	54.0
56.0	58.0	60.0	62.0	64.0	66.0	68.0	70.0		

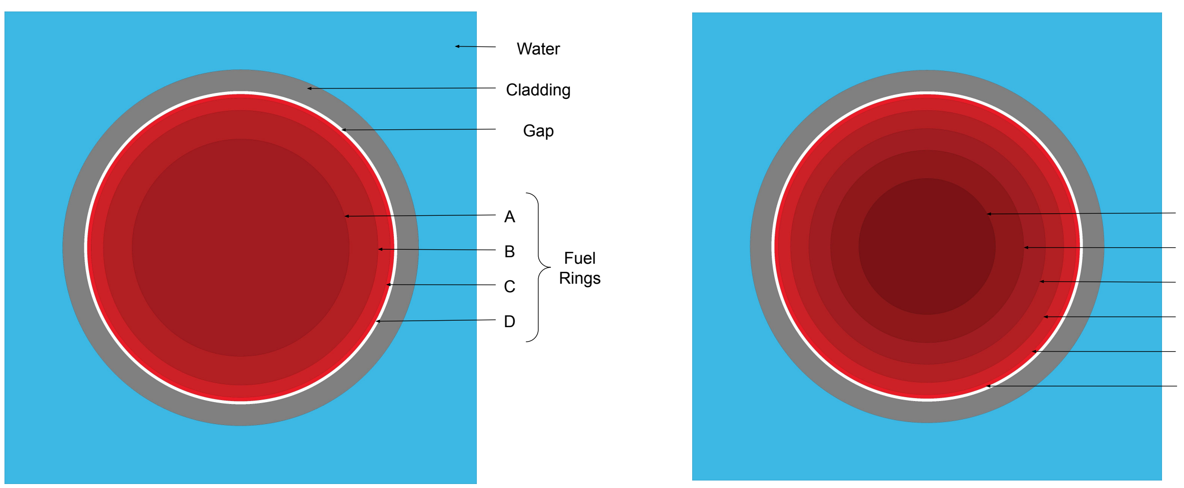

(a) UO_2 (b) $UO_2Gd_2O_3$

Figure 3.2 Scaled up pin cell geometry with distinctive fuel rod rings

Table 3.6 Fuel composition in pin-cell benchmarks

Name	Material	Index[b]	Isotope	Number density 10^{24} nuclide/cm^3	Temperature K
PIN-A	UO_2	4	^{16}O	4.48565×10^{-2}	900
			^{235}U	4.08785×10^{-4}	
			^{238}U	2.20157×10^{-2}	
PIN-B	UO_2	4	^{16}O	4.48632×10^{-2}	900
			^{235}U	7.04005×10^{-4}	
			^{238}U	2.17205×10^{-2}	
PIN-C	UO_2	4	^{16}O	4.48701×10^{-2}	900
			^{235}U	1.01057×10^{-3}	
			^{238}U	2.14140×10^{-2}	

[b] Column values correspond to region numbers in Figure 3.1

There are four 17×17 assembly test cases referred in this document as ASSBLY-A, ASSBLY-B, ASSBLY-C and ASSBLY-D. All four assembly test cases have empty instrumentation and guide tubes. The geometry and fuel composition of ASSBLY-A are given in Figure 3.3 and Table 3.7. The rest of assembly benchmarks, namely cases B, C and D contain various numbers of Gd pins. The geometry and fuel composition of cases B, C and D are provided in Figure 3.4, 3.5, 3.6 and Table 3.8, 3.9, 3.10 correspondingly.

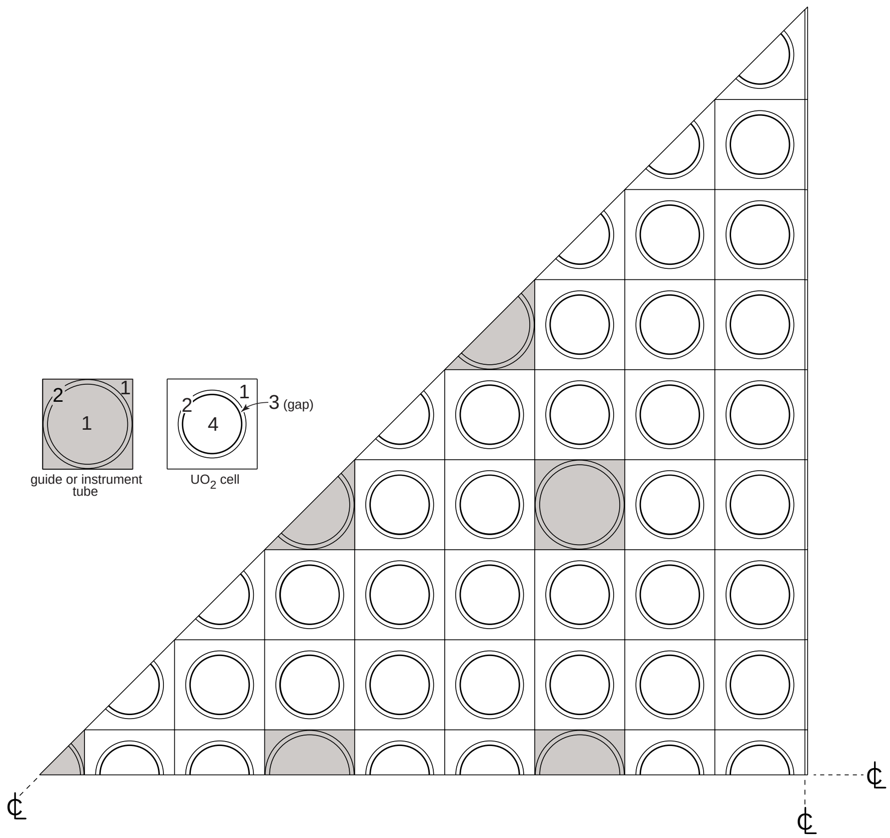

Figure 3.3 Geometry of ASSBLY-A[a]

[a]Numbers in the legend correspond to values of 'Index' column in Tables 3.1, 3.7

Table 3.7 Fuel composition of ASSBLY-A

Material	Index	Isotope	Number density 10^{24} nuclide/cm^3	Temperature K
UO_2	4	^{16}O	4.48565×10^{-2}	900
		^{235}U	4.08785×10^{-4}	
		^{238}U	2.20157×10^{-2}	

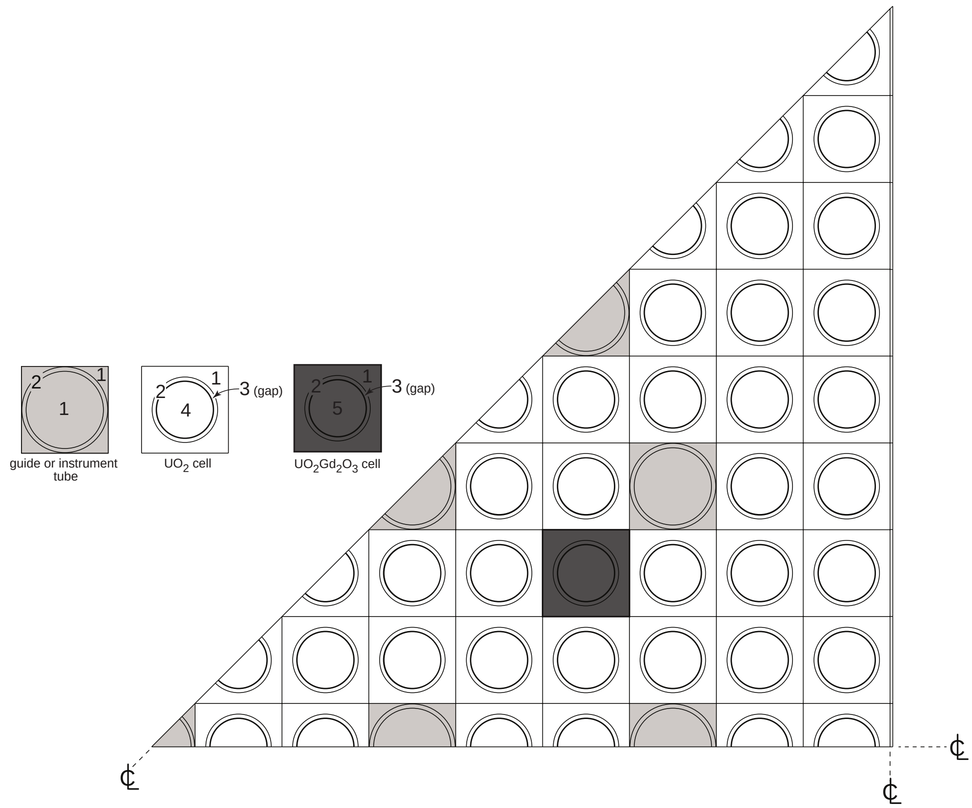

Figure 3.4 Geometry of ASSBLY-B

Table 3.8 Fuel composition of ASSBLY-B

Material	Index	Isotope	Number density 10^{24} nuclide/cm^3	Temperature K
UO_2	4	^{16}O	4.48596×10^{-2}	900
		^{235}U	5.45042×10^{-4}	
		^{238}U	2.18795×10^{-2}	
$UO_2Gd_2O_3$	5	^{16}O	4.40721×10^{-2}	900
		^{235}U	1.42679×10^{-4}	
		^{238}U	1.97006×10^{-2}	
		^{154}Gd	6.37452×10^{-5}	
		^{155}Gd	4.32736×10^{-4}	
		^{156}Gd	5.98515×10^{-4}	
		^{157}Gd	4.57602×10^{-4}	
		^{158}Gd	7.26282×10^{-4}	

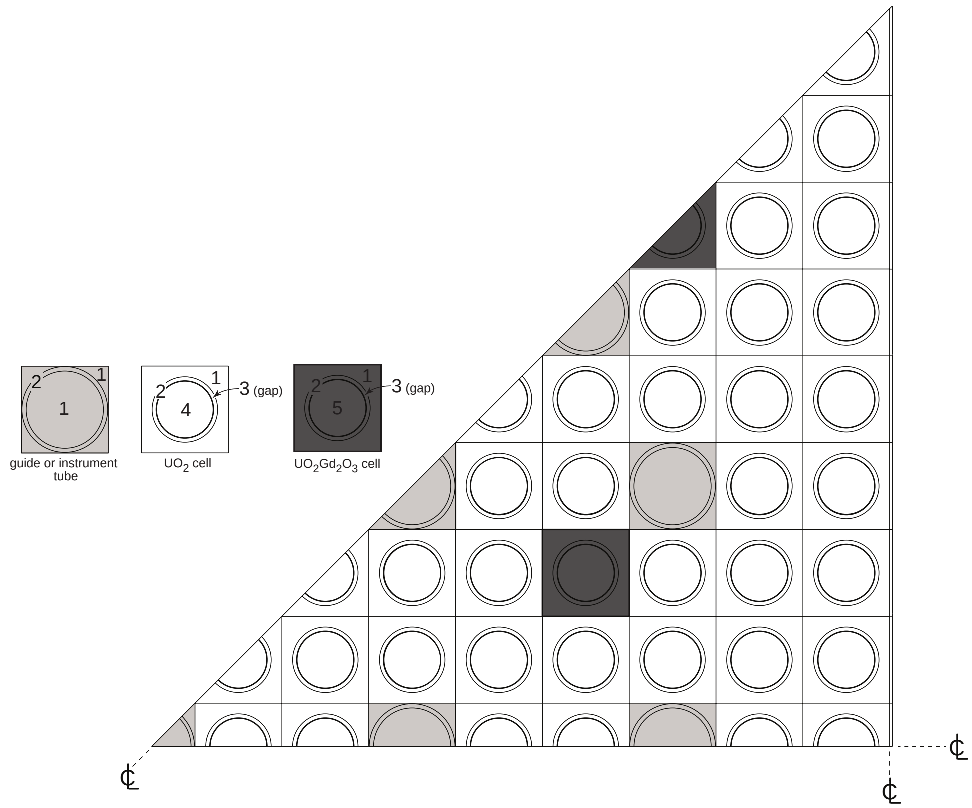

Figure 3.5 Geometry of ASSBLY-C

Table 3.9 Fuel composition of ASSBLY-C

Material	Index	Isotope	Number density 10^{24} nuclide/cm^3	Temperature K
UO_2	4	^{16}O	4.48632×10^{-2}	900
		^{235}U	7.04005×10^{-4}	
		^{238}U	2.17205×10^{-2}	
$UO_2Gd_2O_3$	5	^{16}O	4.40721×10^{-2}	900
		^{235}U	1.42679×10^{-4}	
		^{238}U	1.97006×10^{-2}	
		^{154}Gd	6.37452×10^{-5}	
		^{155}Gd	4.32736×10^{-4}	
		^{156}Gd	5.98515×10^{-4}	
		^{157}Gd	4.57602×10^{-4}	
		^{158}Gd	7.26282×10^{-4}	

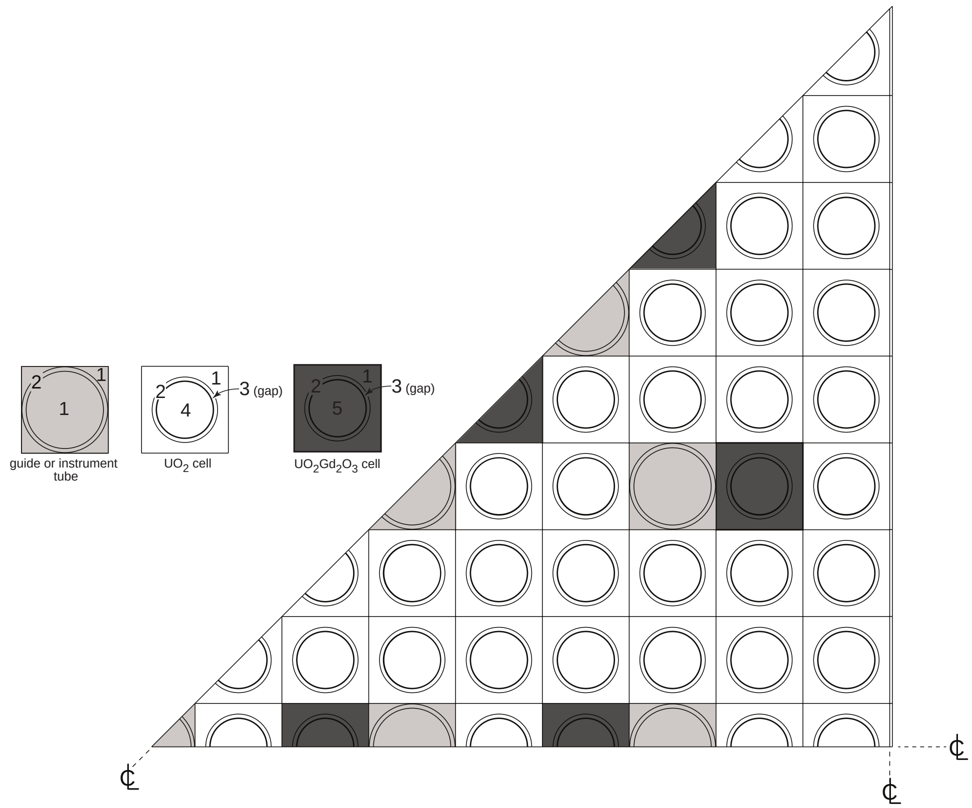

Figure 3.6 Geometry of ASSBLY-D

Table 3.10 Fuel composition of ASSBLY-D

Material	Index	Isotope	Number density 10^{24} nuclide/cm^3	Temperature K
UO_2	4	^{16}O	4.48701×10^{-2}	900
		^{235}U	1.01057×10^{-3}	
		^{238}U	2.14140×10^{-2}	
$UO_2Gd_2O_3$	5	^{16}O	4.41647×10^{-2}	900
		^{235}U	5.09462×10^{-4}	
		^{238}U	1.96177×10^{-2}	
		^{154}Gd	5.68369×10^{-5}	
		^{155}Gd	3.85839×10^{-4}	
		^{156}Gd	5.33652×10^{-4}	
		^{157}Gd	4.08010×10^{-4}	
		^{158}Gd	6.47572×10^{-4}	

3.3 Validation

In this section we are reporting calculation and comparison results between DRAGON5 and SERPENT2 codes. Pin-cell calculation results are reported in Section 3.3.1. Comparison results of assembly test cases are reported in Section 3.3.2.

The data from both SERPENT2 and DRAGON5 calculations were analysed and plotted using specially developed Matlab®/Octave® and Python® scripts which are distributed along with this document. More specifically, DRAGON5 output files (LCM objects) were parsed using Richard Chambon's Matlab/Octave parsers which are distributed along with DRAGON5 [20]. Fission and capture reaction maps are generated using Python and its third party libraries.

3.3.1 Pin-cell Calculations

For pin-cell calculations we have used three UO_2 pin cell test cases. To achieve the best comparison the same discretization of the fuel pin was implemented in both codes. The fuel pin was divided into four rings as specified in Table 3.2 and Figure 3.2. The burnup steps for pin cell benchmarks are exactly the same in both codes and are specified in Table 3.4. The one-level scheme for pin cell calculations is presented in Figures 2.3 and 2.4.

The equation used to calculate absolute discrepancy (pcm) between DRAGON5 and SERPENT2 is:

$$\Delta a = \left[\frac{1}{k_{\text{eff}}(S2)} - \frac{1}{k_{\text{eff}}(D5)} \right] \cdot 10^5 \tag{3.1}$$

Pin-wise average density $\langle n_i \rangle$ of an isotope i is calculated using:

$$\langle n_i \rangle = \frac{\sum_r n_{i,r} \cdot V_r}{\sum_r V_r} \tag{3.2}$$

where $n_{i,r}$ is the atomic density of isotope i in ring r with a volume equal to V_r. The volume fractions of each ring are provided in Table 3.2.

Here we are presenting comparison results only for PIN-C test case. The results for PIN-A and PIN-B test cases are presented in Appendix B, C and are similar to PIN-C results.

Figure 3.7 shows the evolution of the effective multiplication factor for PIN-C test case. The joint behavior of k_{eff} for all pin-cell calculations is shown in Figure 3.8.

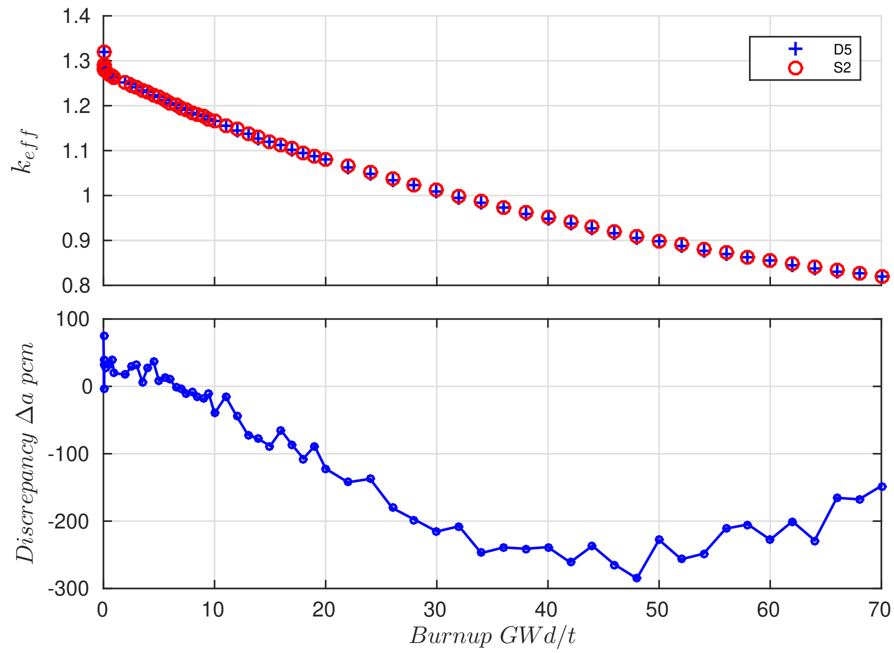

Figure 3.7 Evolution of k_{eff} (PIN-C)

Specific values of multiplication factors and discrepancies for zero burnup, burnup at $\Delta a = \Delta a_{\text{max}}$ and maximum burnup are reported in Table 3.11. Overall, the maximum discrepancy of pin-cell calculations is within 300 pcm (Figure 3.8) and can be argued as a good agreement between SERPENT2 and DRAGON5.

Table 3.11 k_{eff} and absolute discrepancies for pin-cell calculations

Case	*Burnup* MWd/t	$k_{\text{eff}}(S2)$	$k_{\text{eff}}(D5)$	Δa pcm
	0.0	1.08266	1.08402	116
PIN-A	64.0	0.77211	0.77382	286
	70.0	0.76602	0.76742	239
	0.0	1.23811	1.23945	87
PIN-B	36.0	0.89806	0.89647	-197
	70.0	0.78306	0.78369	103
	0.0	1.31943	1.32074	75
PIN-C	48.0	0.90884	0.90649	-285
	70.0	0.82006	0.81907	-148

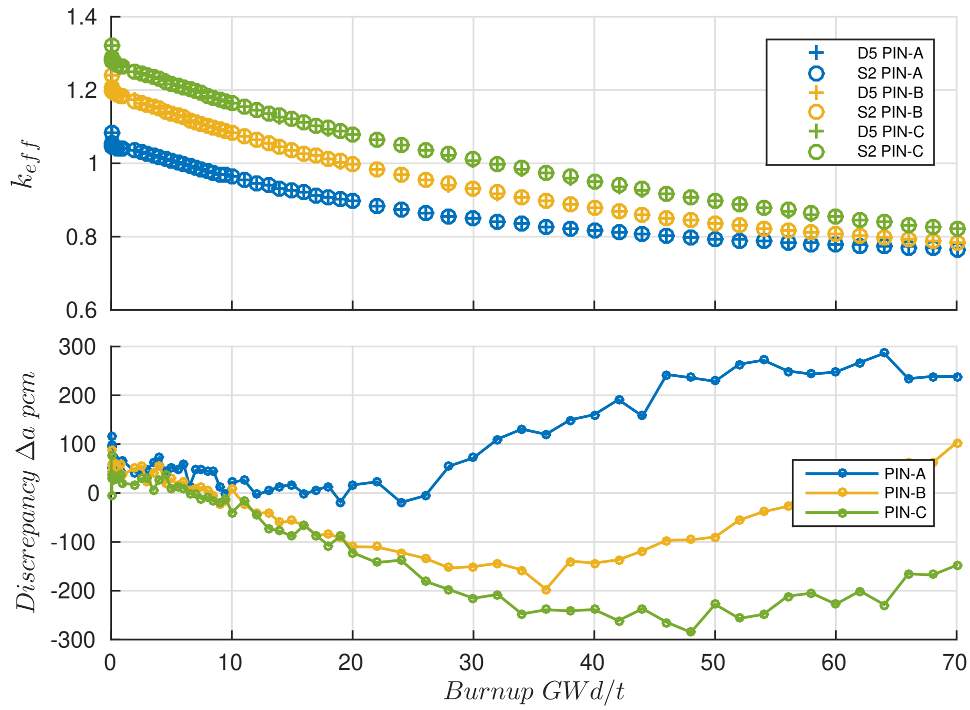

Figure 3.8 Evolution of k_{eff} for all pin-cell calculations

The evolution of atomic density during burnup for PIN-C is presented below. Density plots for PIN-A and PIN-B test cases are reported in Appendix B, C.

The detailed evolution and relative error of ^{235}U, ^{239}Pu, ^{240}Pu and ^{241}Pu isotopes in each ring of the fuel pin are presented in Figure 3.9, 3.10, 3.11, 3.12.

Some of the actinides and fission products are presented as pin-wise averages in Figure 3.13 and Figure 3.14.

The observed maximum relative error of specific isotopes and fission products is presented in Table 3.12. The table shows in which ring the maximum error was observed and at which burnup. Overall ^{235}U is the worst performing isotope and reaches a relative error of $\approx 5.5\%$ at the end of the burnup. The plutonium isotopes show error of less than $\approx 4.3\%$ during the whole burnup calculation.

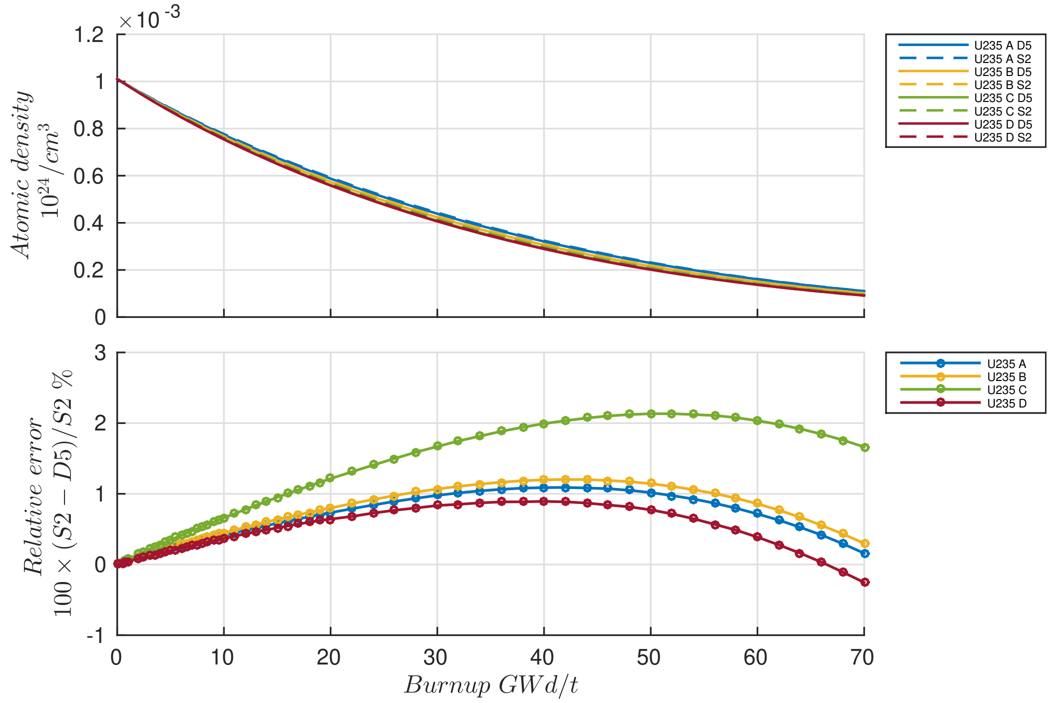

Figure 3.9 Atomic density of ^{235}U (PIN-C)

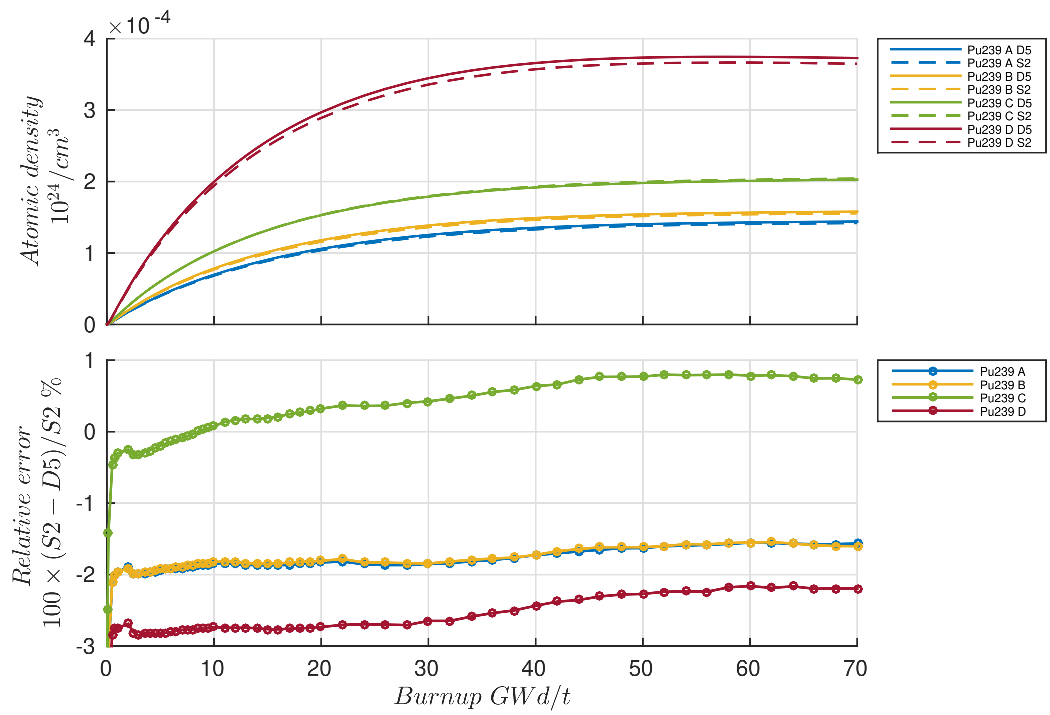

Figure 3.10 Atomic density of ^{239}Pu (PIN-C)

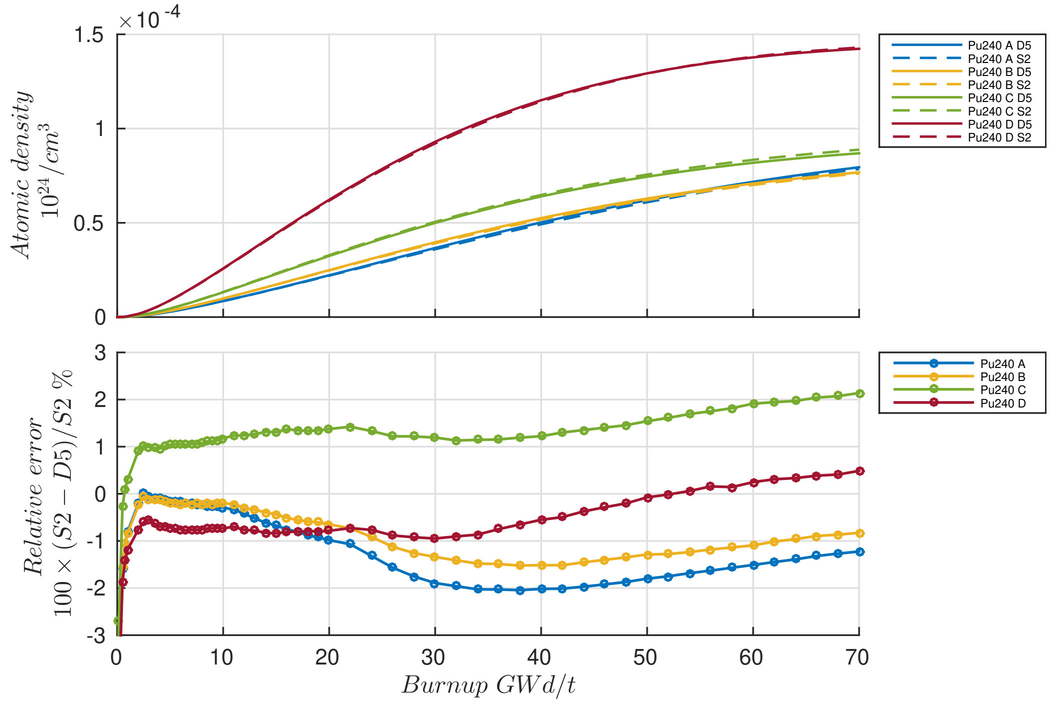

Figure 3.11 Atomic density of ^{240}Pu (PIN-C)

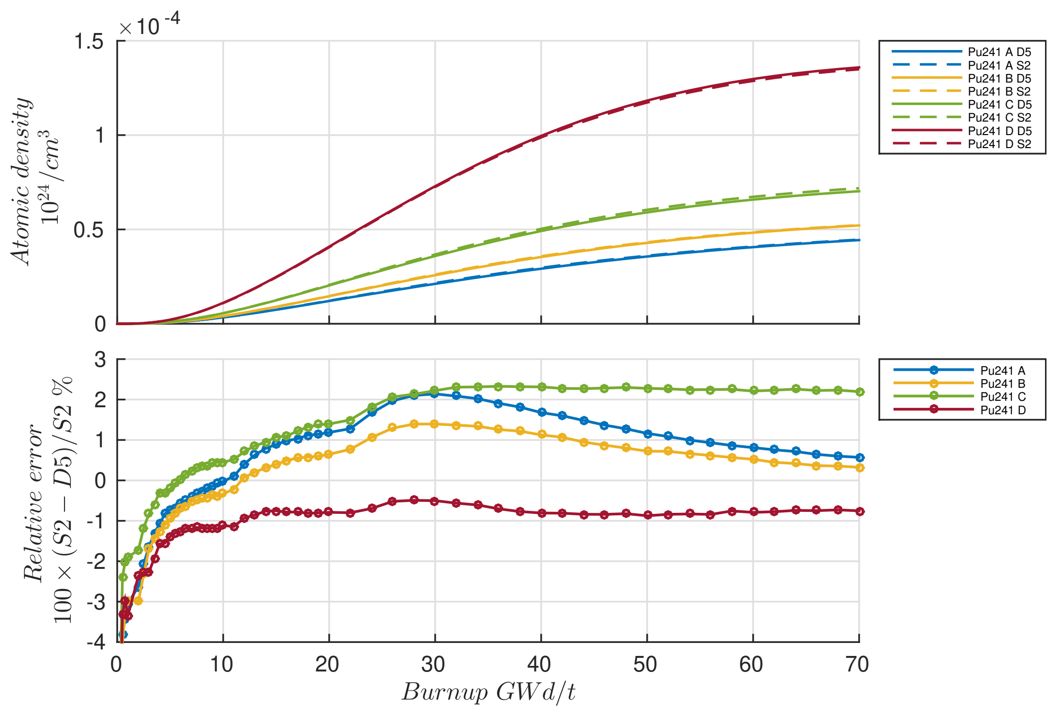

Figure 3.12 Atomic density of ^{241}Pu (PIN-C)

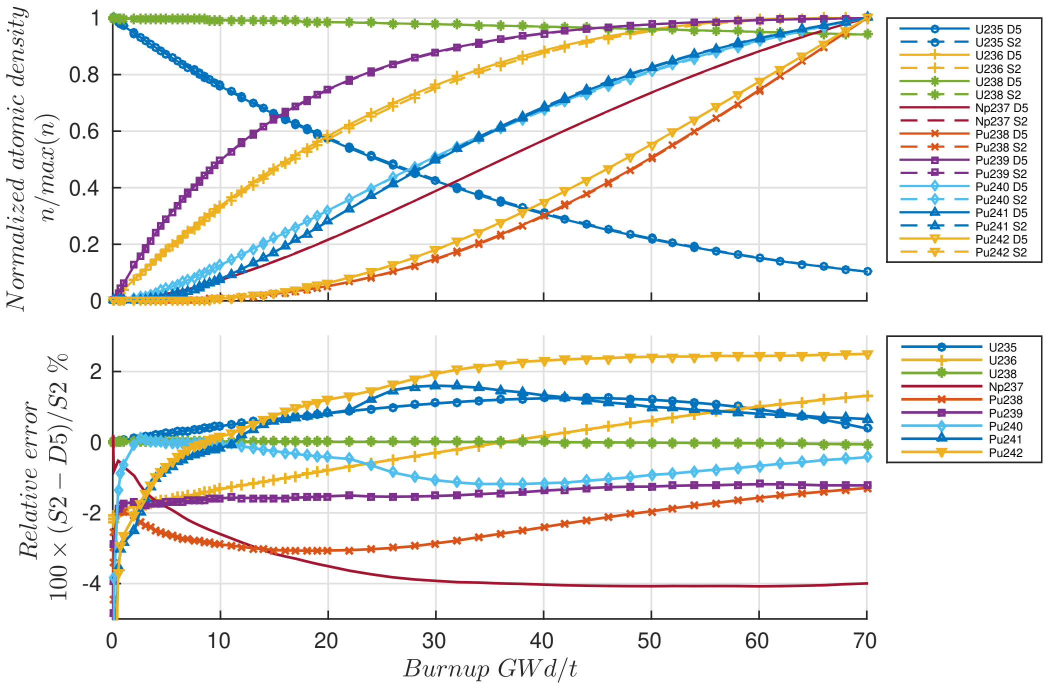

Figure 3.13 Pin-wise average density of actinides (PIN-C)

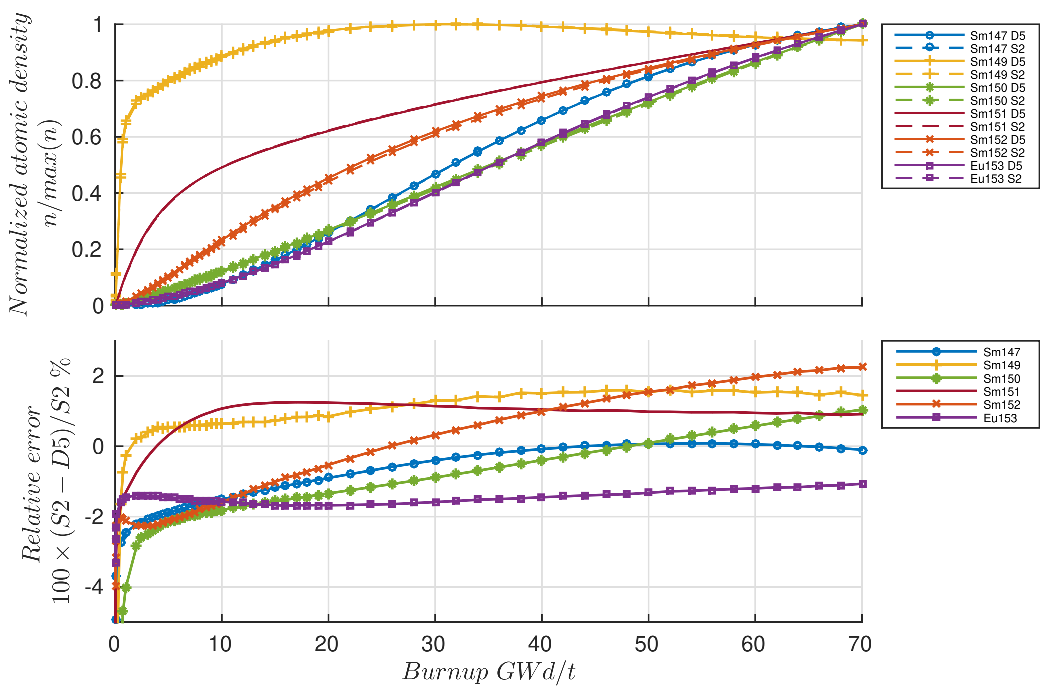

Figure 3.14 Pin-wise average density of fission products (PIN-C)

Table 3.12 Maximum relative error of isotopic densities in pin-cell calculations

	PIN-A			PIN-B			PIN-C		
	Ring	*Error* %	*Burnup* GWd/t	*Ring*	*Error* %	*Burnup* GWd/t	*Ring*	*Error* %	*Burnup* GWd/t
U235	D	-5.453	70.00	D	-2.032	70.00	C	2.133	52.00
U236	C	-1.230	0.75	C	-2.018	0.75	C	-2.456	0.75
U238	C	-0.325	70.00	C	-0.242	70.00	C	-0.174	70.00
Np237	C	-1.856	3.00	C	-3.071	24.00	A	-4.403	62.00
Pu238	C	-2.199	3.50	C	-2.980	5.00	C	-3.742	15.00
Pu239	D	-3.428	28.00	D	-2.899	26.00	D	-2.854	3.00
Pu240	C	3.344	2.00	C	2.350	70.00	C	2.139	70.00
Pu241	C	2.580	4.50	C	2.446	32.00	A	-3.420	0.75
Pu242	C	4.284	66.00	C	3.889	70.00	C	3.405	70.00
Sm147	C	-2.113	0.75	C	-2.836	0.75	C	-3.217	0.75
Sm149	C	2.484	70.00	C	2.793	66.00	C	3.032	68.00
Sm150	C	3.215	70.00	C	-4.506	0.75	C	-5.691	0.75
Sm151	C	3.380	70.00	C	3.070	66.00	C	2.746	58.00
Sm152	C	3.966	62.00	C	3.616	70.00	C	3.150	70.00
Eu153	C	1.199	70.00	C	-1.761	0.75	C	-2.184	0.75

3.3.2 Assembly Calculations

In this section we present the results for assembly calculations without leakage by imposing zero buckling. These calculations were performed with DRAGON5 and SERPENT2. DRAGON5 calculations were performed on one eighth of the assembly. SERPENT2 calculations were conducted using 4000 cycles (20 skipped cycles) of 4000 source neutrons for each of the seven test cases.

There are 4 assembly test cases in this benchmark which are referred in this document as ASSBLY-A, ASSBLY-B, ASSBLY-C and ASSBLY-D. Here the calculation results of ASSBLY-A and ASSBLY-D will be presented. The results for ASSBLY-B and ASSBLY-C are presented in Appendix D, E and are quite similar to ASSBLY-D.

The ASSBLY-A test case contains only UO_2 fuel pins. The other assembly test cases contain also Gd fuel-pins[1]. ASSBLY-D contains the highest number of Gd fuel pins as shown in Figure 3.6 and has the highest absolute discrepancy of k_{eff}. All reported discrepancies are calculated relative to SERPENT2 code. Two DRAGON5 calculations were performed for each of the assembly type, namely

- One-level calculation (1L) as described in Section 2.3.1
- Two-level calculation (2L) as described in Section 2.3.2

The group reaction rate of nuclear reaction x inside region i of the spacial domain is defined as the product of volume-integrated group flux ϕ_i^g (unit $cm^{-2}s^{-1}$) and group macroscopic cross section $\Sigma_{x,i}^g$ (unit cm^{-1}):

$$\mathcal{T}_i^g = \Sigma_{x,i}^g \phi_i^q \tag{3.3}$$

The sum of all reaction rates of all regions i and all groups g represents the total reaction rate. In this study, two group fission and capture reaction rates were calculated and compared with SERPENT2 results. The results are presented in Appendix F. Furthermore, total pin fission and capture reaction rates of each pin in the assembly were calculated and compared with SERPENT2. The results are presented as heat-maps and step plots. Two group fission/capture rates and total pin fission/capture rates were normalized to the total fission rate of DRAGON5.

[1] In these assemblies some of the UO_2 fuel-pins contain gadolinium (burnable poison) to compensate initial reactivity.

The equation used to calculate relative error of fission and capture rates between DRAGON5 and SERPENT2 is:

$$\Delta r = \left[\frac{\tau_{D5} - \tau_{S2}}{\tau_{S2}}\right] \cdot 100 \tag{3.4}$$

and $|\Delta r|$ is the corresponding absolute relative error.

The flux is normalized according to:

$$\frac{1}{k_{\text{eff}}} \sum_{j=1}^{J_{\text{fiss}}} \int_0^\infty dE \int_V d^3r\, \nu \Sigma_{\text{f},j}(\boldsymbol{r}, E)\phi(\boldsymbol{r}, E) = 1 \tag{3.5}$$

where $\phi(\boldsymbol{r}, E)$ is the neutron flux, ν is the number of secondary neutrons, $\Sigma_{\text{f},j}$ is the macroscopic fission cross section of fissile isotope j and J_{fiss} is the total number of fissile isotopes.

Assembly-wise average density $\langle n_i \rangle$ of an isotope i is calculated using:

$$\langle n_i \rangle = \sum_{\substack{all \\ pins}} \left(\frac{\sum_r n_{i,r} \cdot V_r}{\sum_r V_r} \right) \tag{3.6}$$

where $n_{i,r}$ is the atomic density of isotope i in ring r with a volume equal to V_r.

Table 3.13 Execution time of assembly burnup calculations in minutes

	ASSBLY-A	ASSBLY-B	ASSBLY-C	ASSBLY-D
DRAGON5 2L	355	835	883	1154
DRAGON5 1L	789	2665	2566	2730
SERPENT2	64764	105156	106308	106190

Table 3.13 shows the execution time of burnup calculations for all assembly cases[2]. It shows that two-level scheme is about 2-3 times faster than one-level scheme.

Calculation Results (ASSBLY-A)

The ASSBLY-A test case consists of only UO_2 fuel pins as described in Section 3.2. The effective multiplication factor for the 2L scheme has a maximum discrepancy of 351 pcm

[2] SERPENT2 calculations were performed on multiple CPUs using MPI parallel calculation mode. The reported values are the calculation times on one CPU.

compared to 446 pcm in 1L scheme (Figure 3.15, Table 3.15).

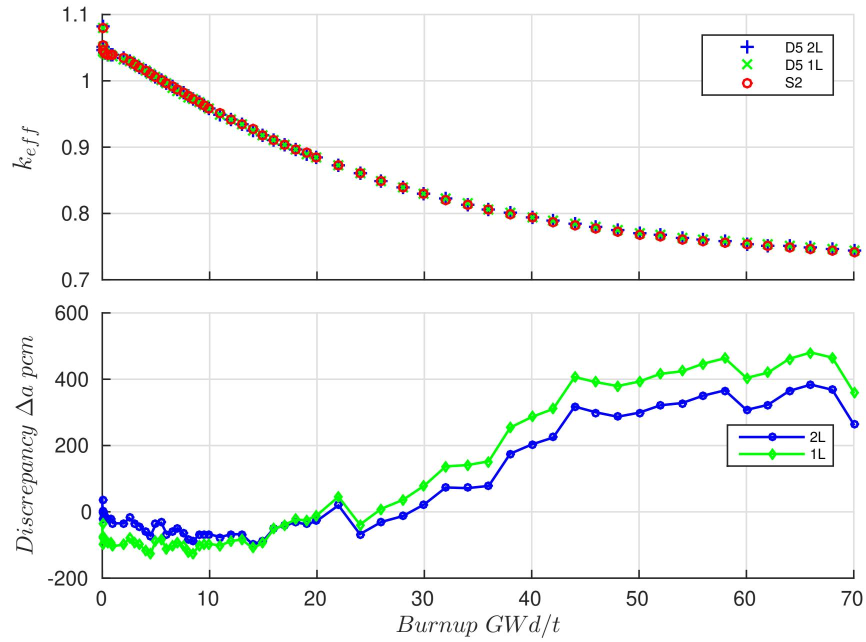

Figure 3.15 Evolution of k_{eff} (ASSBLY-A)

For the analyses of ASSBLY-A we have chosen C0505 pin-cell. The relative errors of ^{235}U, ^{239}Pu, ^{240}Pu and ^{241}Pu in each ring of the C0505 pin are presented in Figure 3.16, 3.17, 3.18, 3.19. Among these isotopes the worst performing one in pin C0505 is ^{235}U with a relative error of about 25% (Figure 3.16). It is important to note that the relative error of assembly-wise average density is less than 7% for 2L scheme as shown in Figure 3.22.

The relative errors of pin-wise average densities of actinides and fission products in C0505 are presented in Figures 3.20, 3.21.

The accuracy of the DRAGON5 lattice code can be presented using the pin power map of the assembly. Figures 3.23, 3.24 present the fission and capture reaction distribution at time zero. The maximum relative error calculated with Equation (3.4) is less than 1% for 2L scheme. The color-bar and cell colors of all heat-maps represent the 2L scheme distribution. At the same time, all the heat-maps contain 1L scheme values located below the 2L values. Figures 3.25, 3.26 present the relative errors of fission and capture rate at the end of the burnup calculation. The maximum relative error at this point is below 2.7% for fission rates and less than 1% for capture rates. Table 3.14 shows maximum and average absolute errors for fission and capture rates. Here the average error for the 2L scheme is higher than that of 1L scheme. More detailed results of fission and capture rates are presented in Tables F.1, F.2. These 2 group reaction rates are normalized using Eq. 3.5.

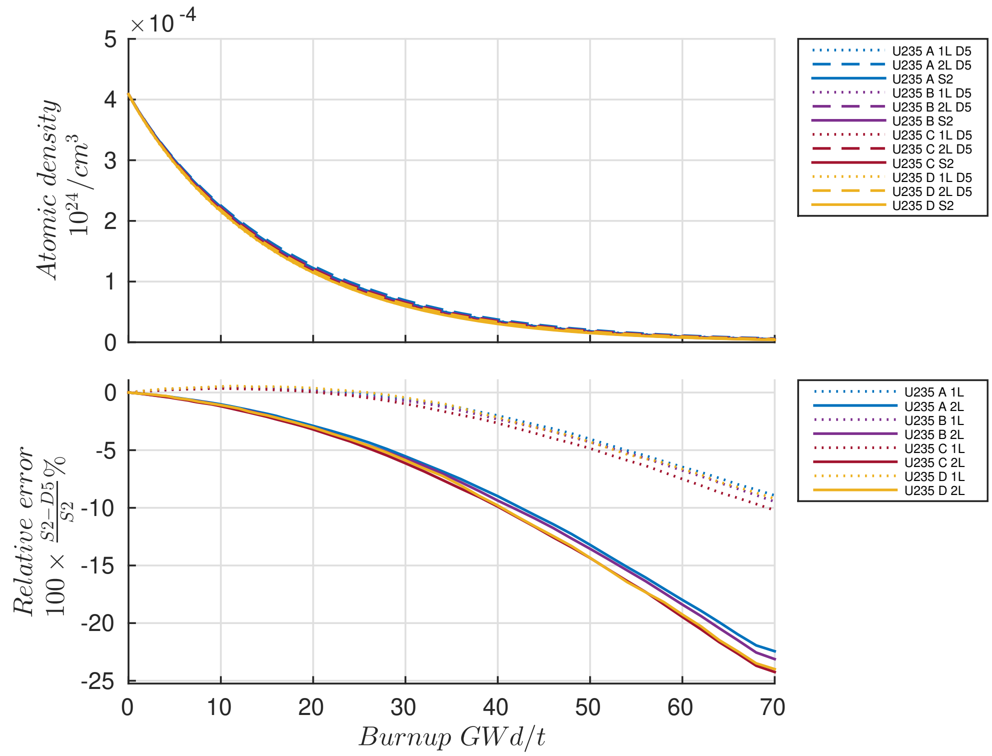

Figure 3.16 Atomic density of ^{235}U (ASSBLY-A, C0505)

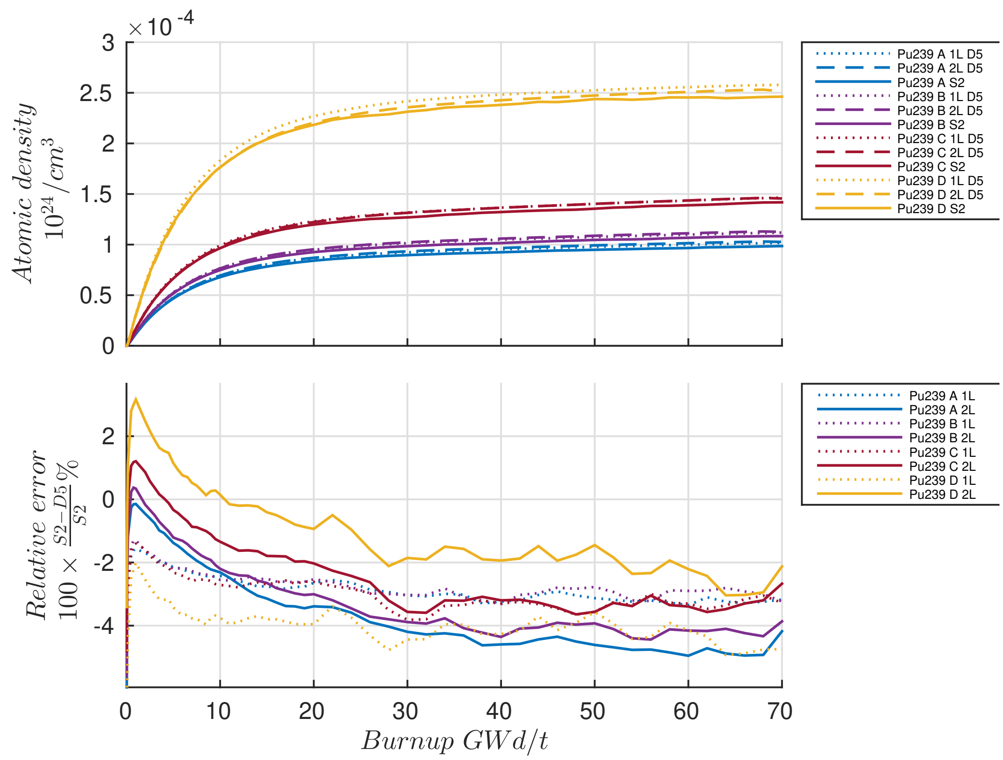

Figure 3.17 Atomic density of ^{239}Pu (ASSBLY-A, C0505)

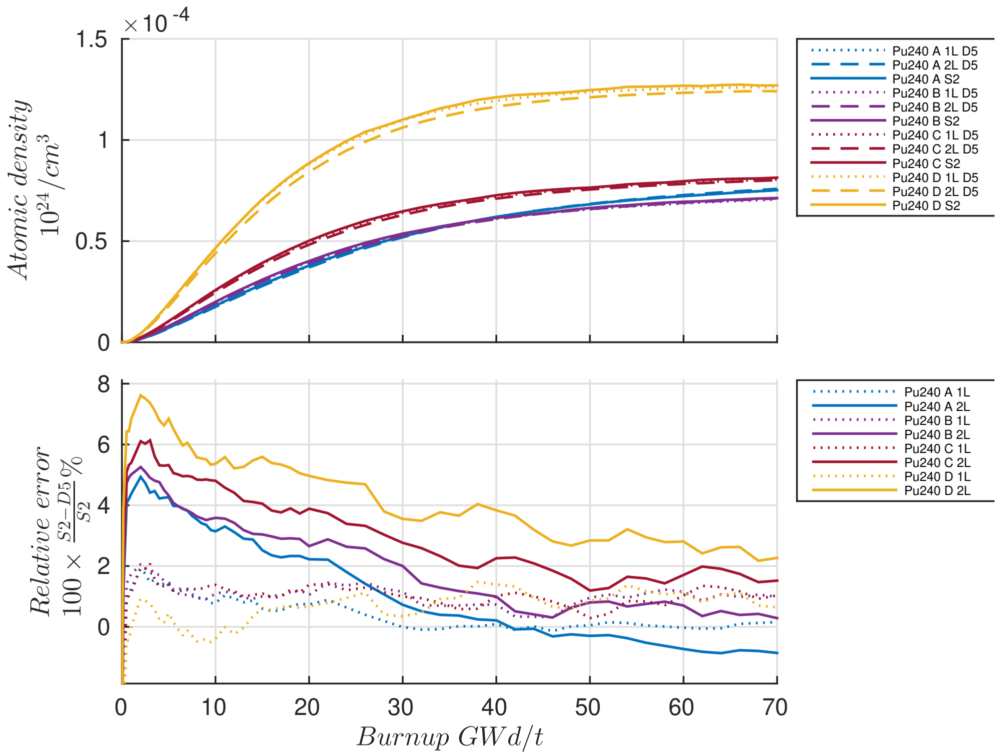

Figure 3.18 Atomic density of ^{240}Pu (ASSBLY-A, C0505)

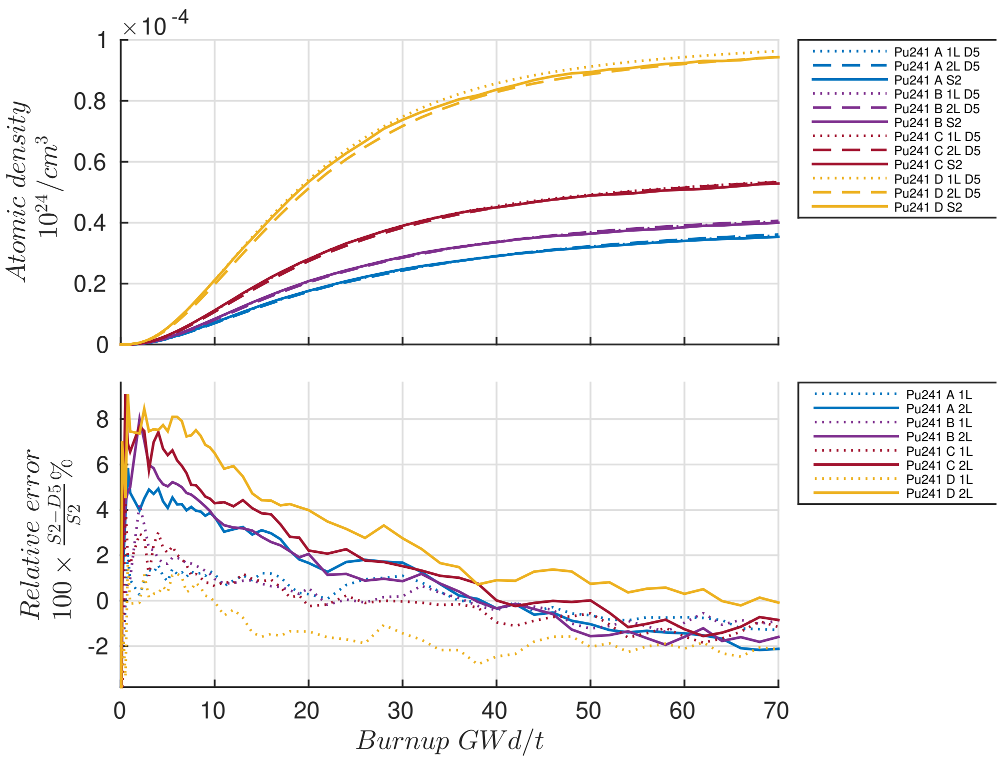

Figure 3.19 Atomic density of ^{241}Pu (ASSBLY-A, C0505)

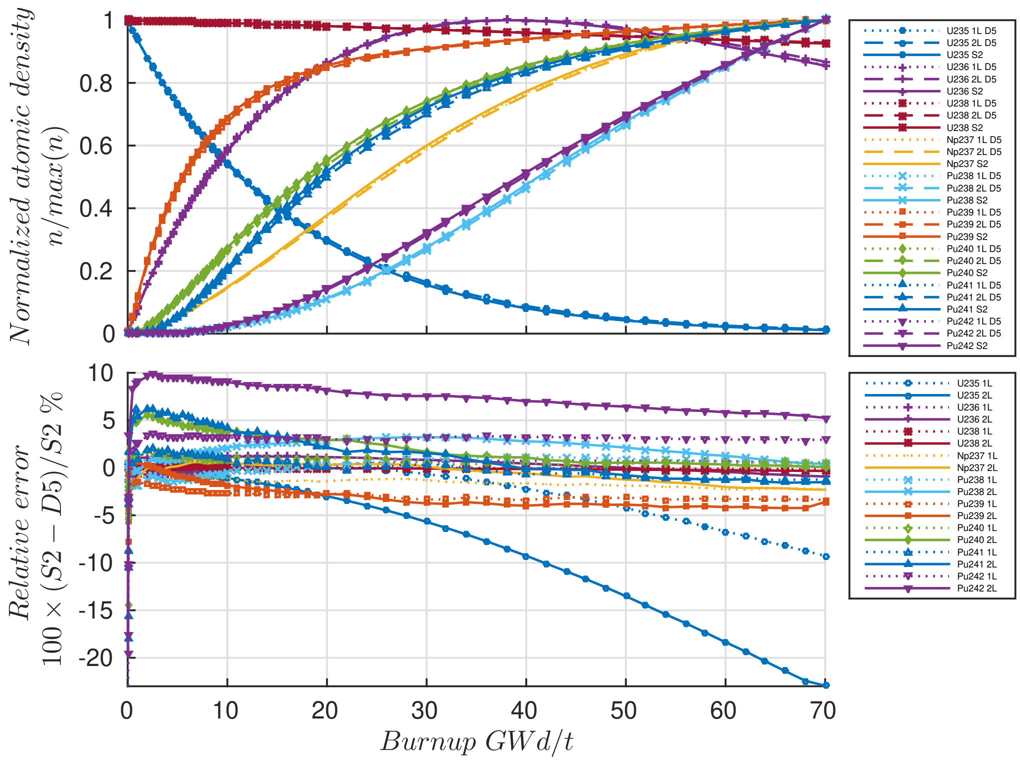

Figure 3.20 Pin-wise average density of actinides (ASSBLY-A, C0505)

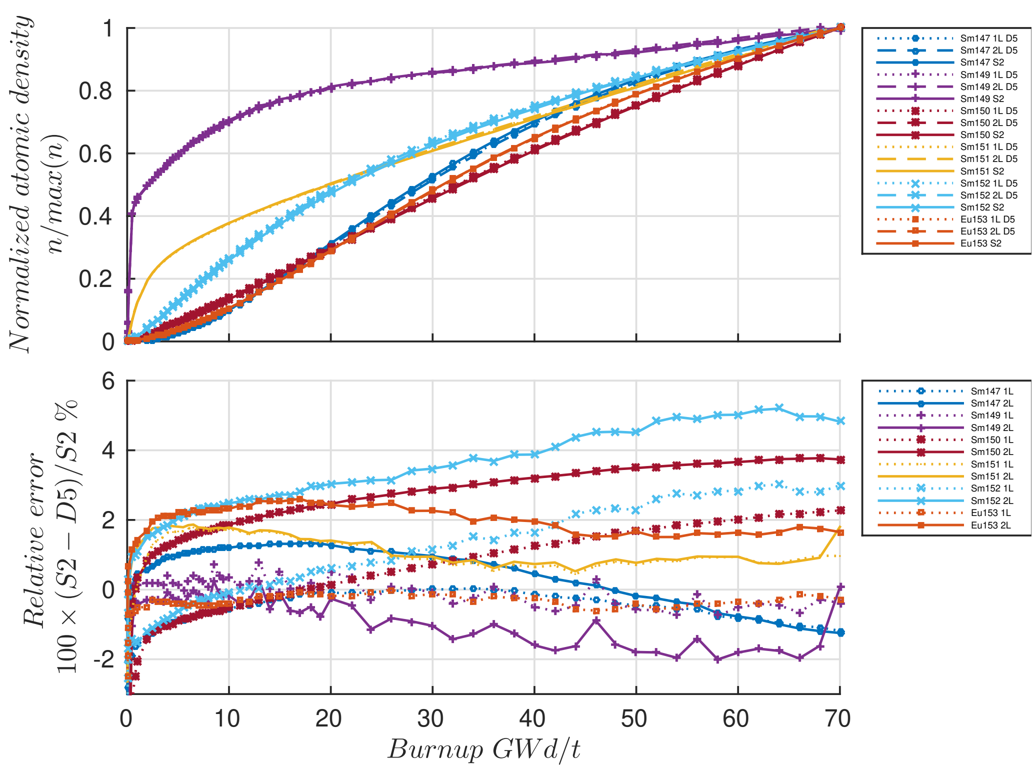

Figure 3.21 Pin-wise average density of fission products (ASSBLY-A, C0505)

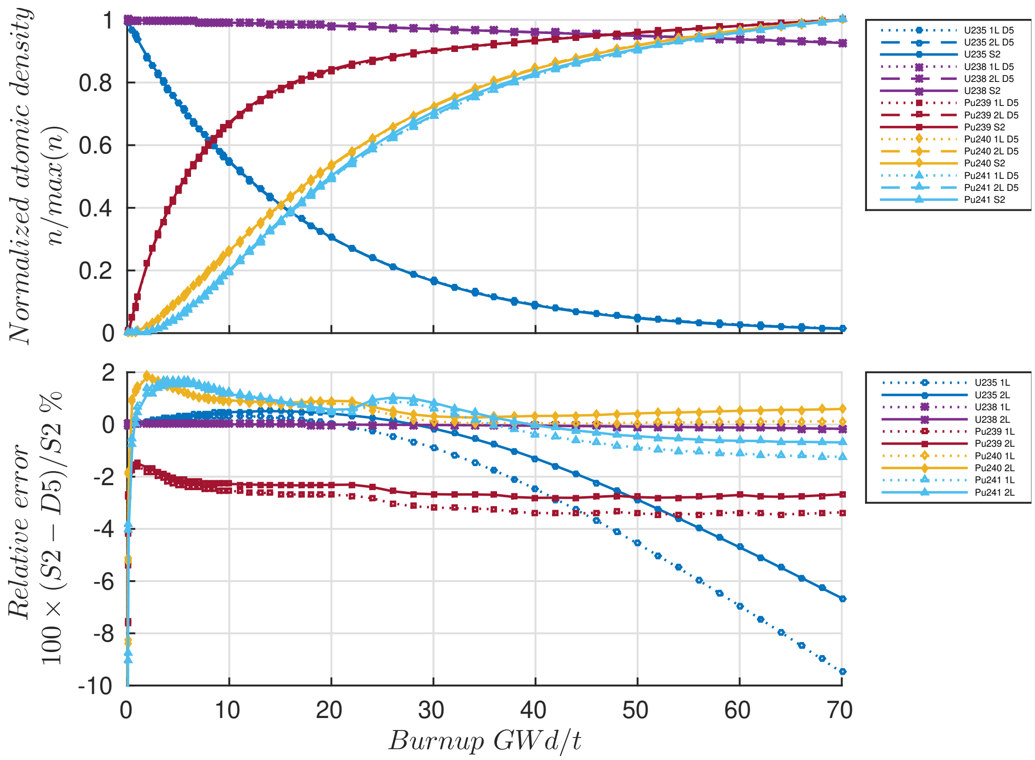

Figure 3.22 Assembly-wise average atomic densities (ASSBLY-A)

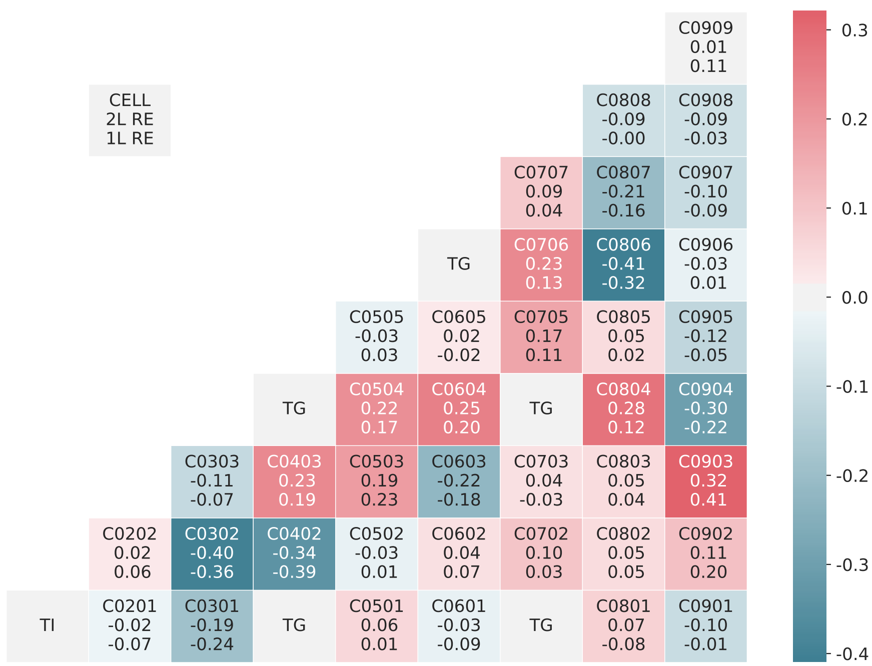

Figure 3.23 Relative discrepancies in the fission reaction map at zero burnup (ASSBLY-A)

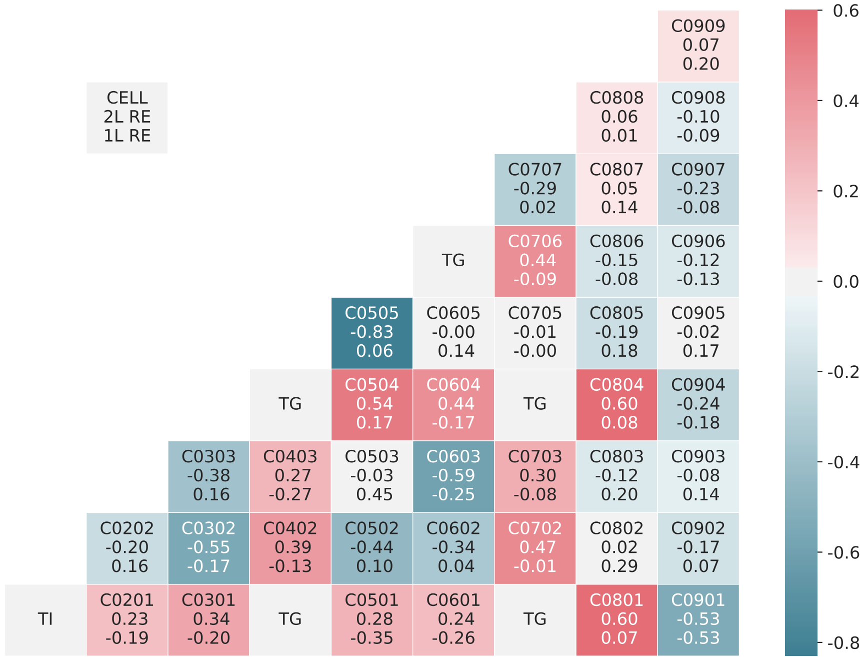

Figure 3.24 Relative discrepancies in the capture reaction map at zero burnup (ASSBLY-A)

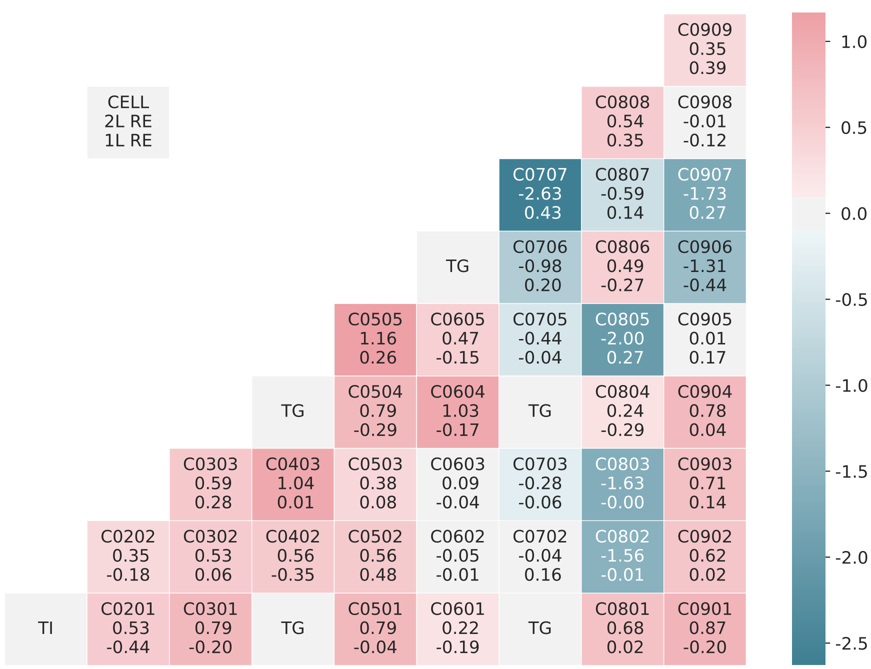

Figure 3.25 Relative discrepancies in the fission reaction map at maximum burnup (ASSBLY-A)

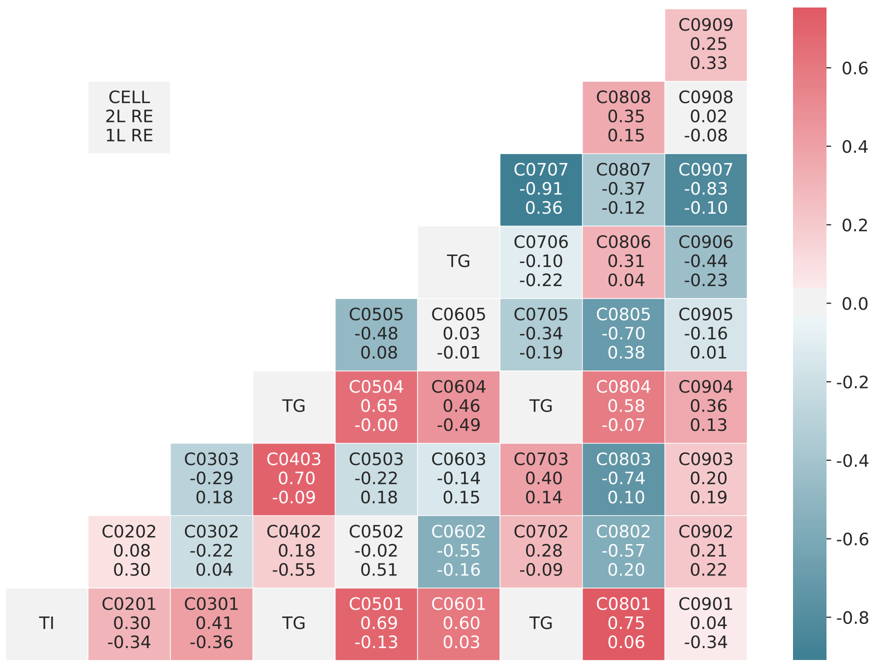

Figure 3.26 Relative discrepancies in the capture reaction map at maximum burnup (ASSBLY-A)

Calculation Results (ASSBLY-D)

The ASSBLY-D test case has the maximum number of Gd fuel pins (Section 3.2) and presents the worst performing assembly in this benchmark. The effective multiplication factor has a discrepancy of 759 pcm (2L scheme) and 1012 pcm (1L scheme) (Figure 3.27, 3.28).

Here we identified pin-cell C0301 as one of the worst performing. The detailed evolution and relative error of ^{235}U, ^{239}Pu, ^{240}Pu and ^{241}Pu isotopes for C0301 are presented in Figures 3.29, 3.30, 3.31, 3.32. The letters A, B, C, D, E and F specified in the legends of these plots refer to the pin ring regions described in Table 3.2 and shown in Figure 3.2. Among these isotopes the worst performing is ^{239}Pu with a relative error of about 7% and 8% for 2L and 1L schemes respectively (Figure 3.30). The relative error of assembly-wise average densities is shown in Figure 3.35. Here we again observe ^{239}Pu with a relative error of about 3% and 4% for 2L and 1L schemes respectively which is twice smaller for C0301.

The relative errors of pin-wise average densities of actinides and fission products in C0301 are presented in Figures 3.33, 3.34.

The fission and capture pin power maps for zero burnup are shown in Figures 3.36, 3.37. Here we observe for both schemes maximum relative error of less than 2% and 4% for fission and capture respectively. The pin power maps at burnup of about 13 GWd/t is shown in Figures 3.38, 3.39. This burnup represents the point when almost all Gd was consumed and multiplication factor has the maximum value. At this point we observe maximum relative error of about 3% for capture and 1.5% for fission. The pin power maps at maximum burnup are shows in Figures 3.40, 3.41. At this point we observe about 4% maximum relative error for fission and capture. Overall, the maximum relative error for fission and capture is below 4% for both schemes.

Table 3.14 shows maximum and average absolute errors for fission and capture rates. In this table we observe that the average error for the 2L scheme is higher compared to 1L scheme.

More detailed results of fission and capture rates are presented in Tables F.7, F.8 where the results are normalized with Eq. 3.5.

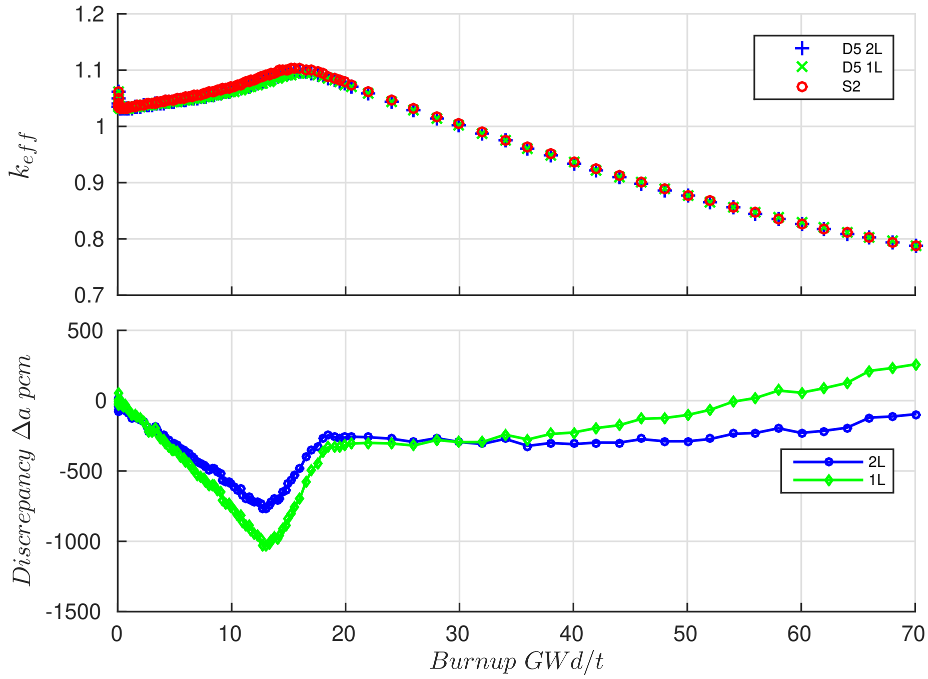

Figure 3.27 Evolution of k_{eff} (ASSBLY-D)

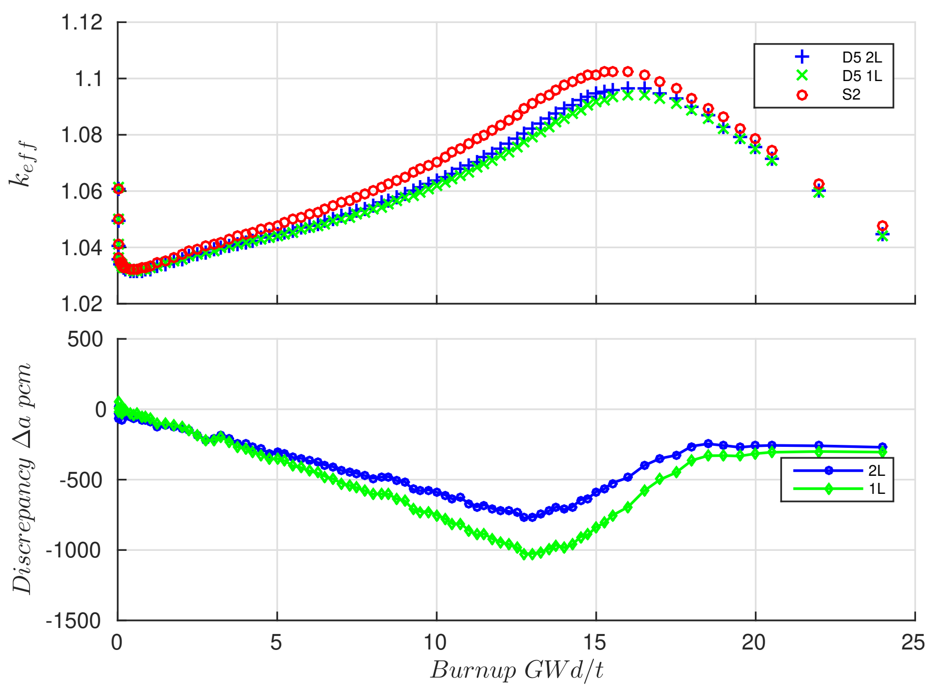

Figure 3.28 Evolution of k_{eff} up to $25GWd/t$ (ASSBLY-D)

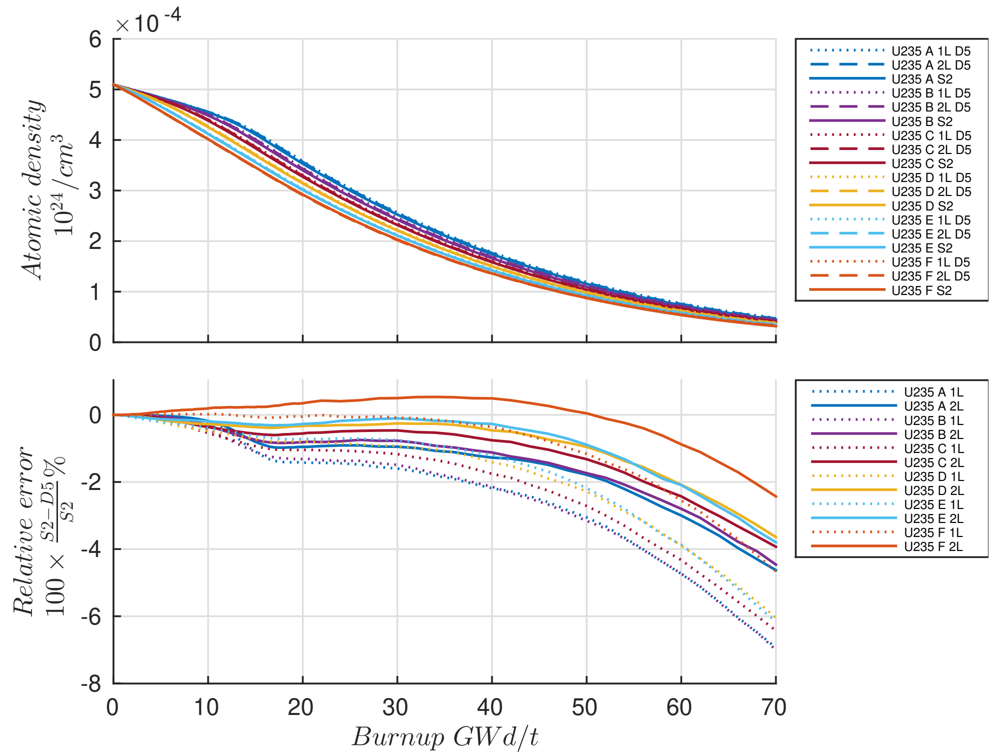

Figure 3.29 Atomic density of ^{235}U (ASSBLY-D, C0301)

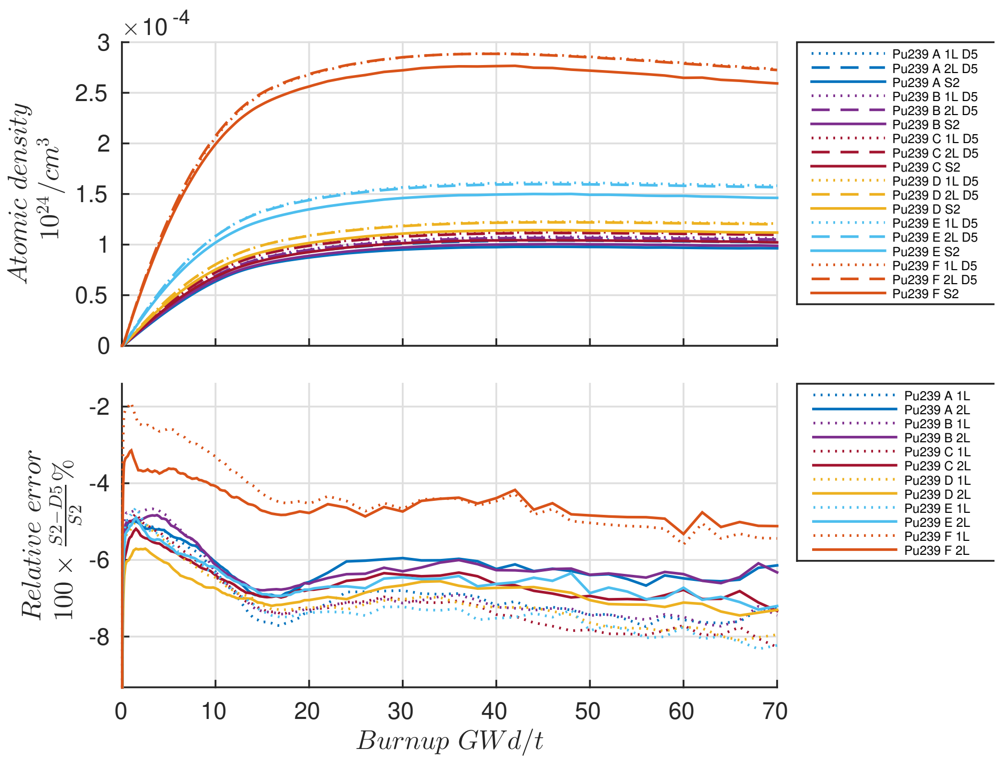

Figure 3.30 Atomic density of ^{239}Pu (ASSBLY-D, C0301)

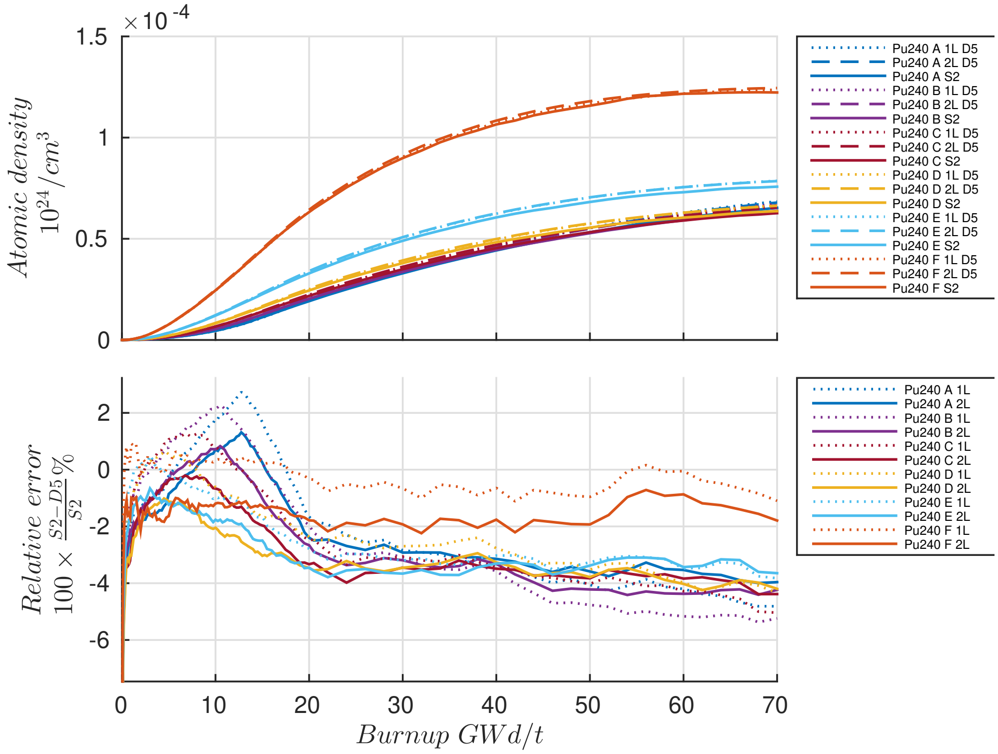

Figure 3.31 Atomic density of ^{240}Pu (ASSBLY-D, C0301)

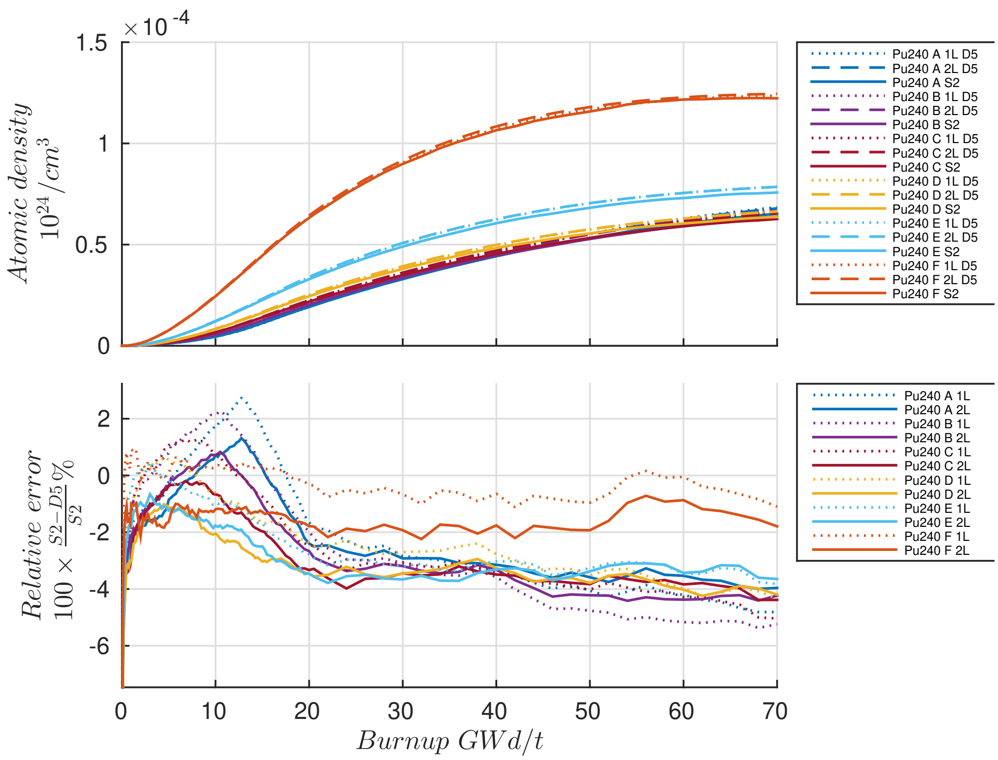

Figure 3.32 Atomic density of ^{241}Pu (ASSBLY-D, C0301)

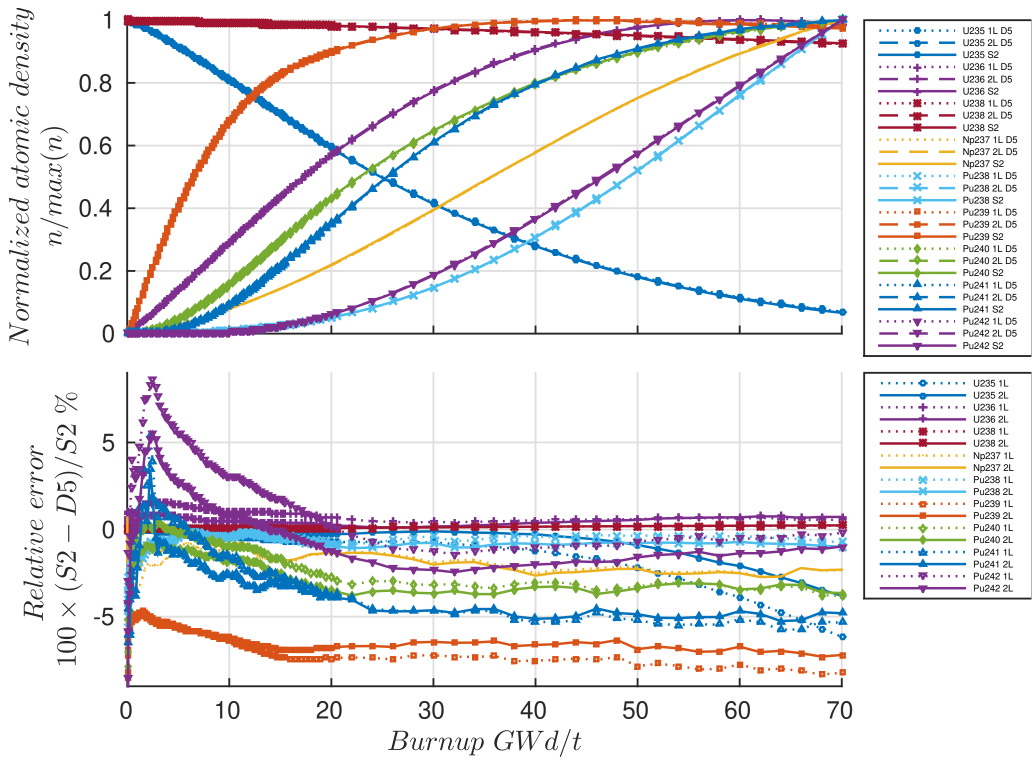

Figure 3.33 Pin-wise average density of actinides (ASSBLY-D, C0301)

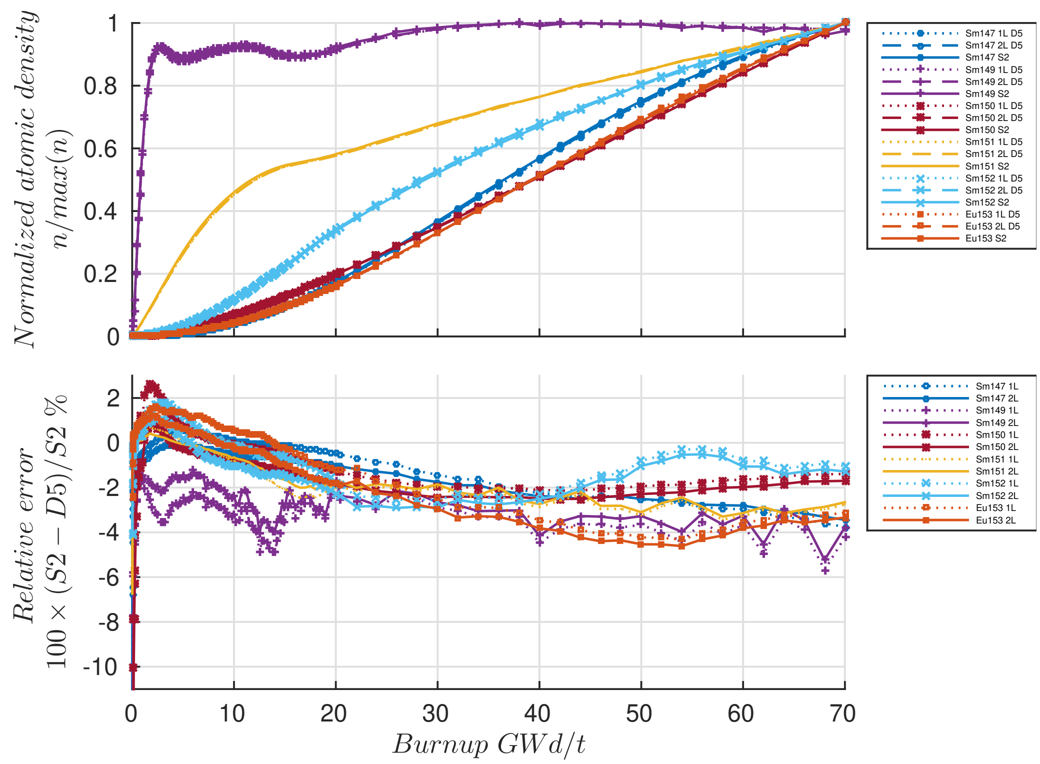

Figure 3.34 Pin-wise average density of fission products (ASSBLY-D, C0301)

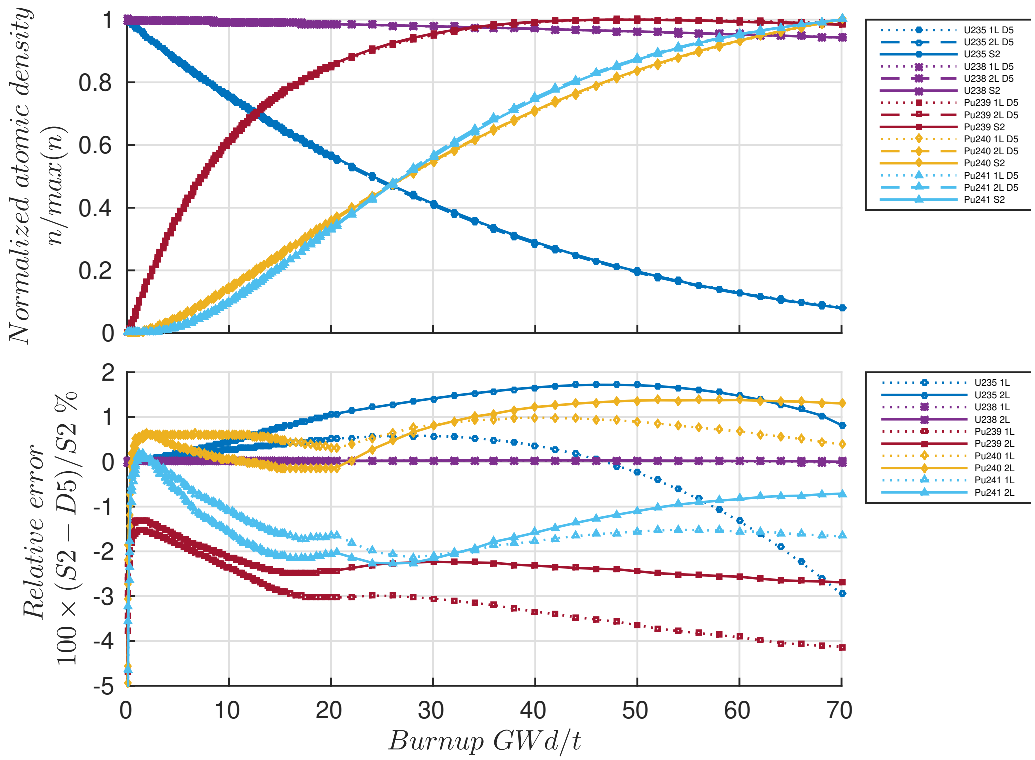

Figure 3.35 Assembly-wise average atomic densities (ASSBLY-D)

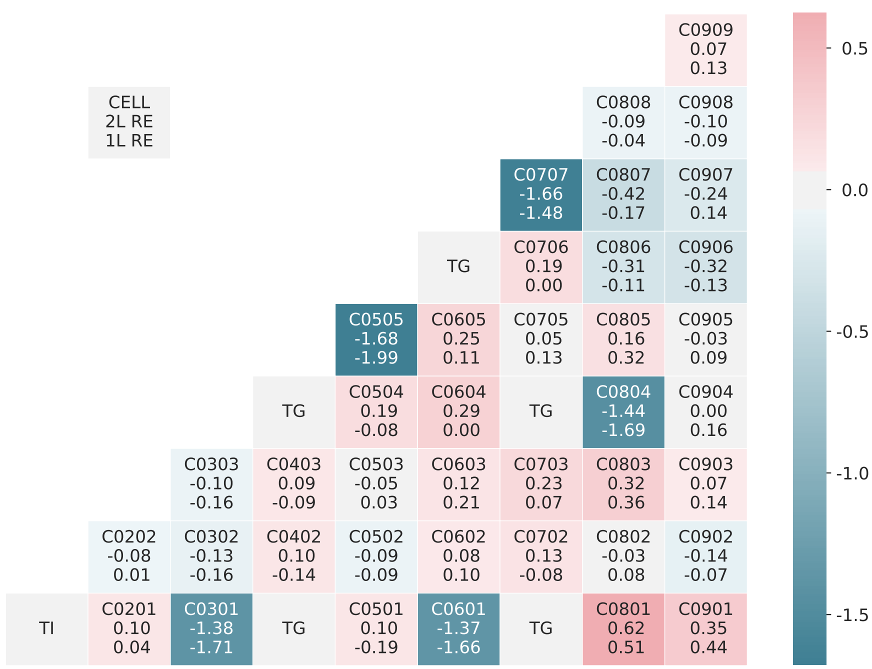

Figure 3.36 Relative discrepancies of the fission reaction map at zero burnup (ASSBLY-D)

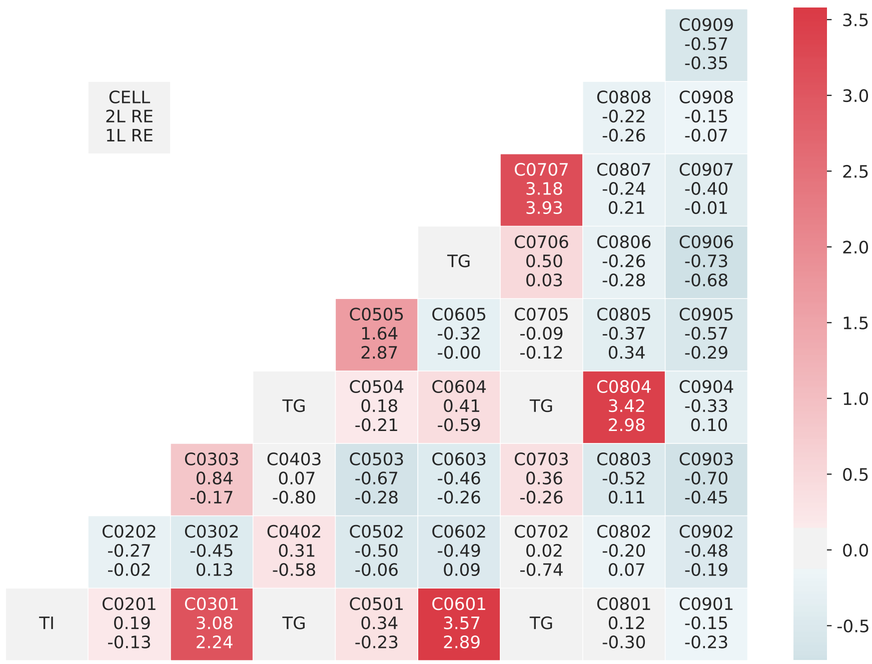

Figure 3.37 Relative discrepancies of the capture reaction map at zero burnup (ASSBLY-D)

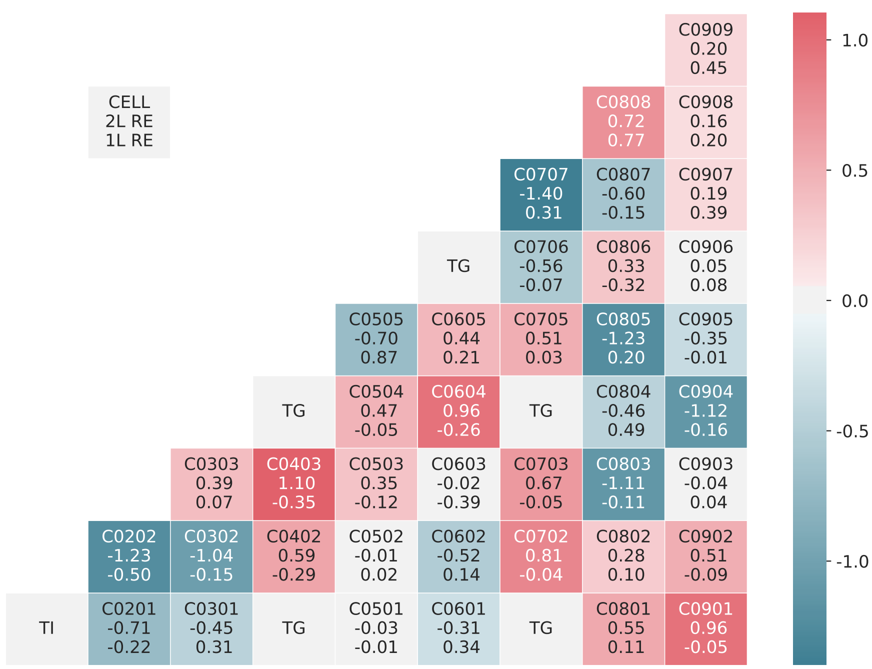

Figure 3.38 Relative discrepancies of the fission reaction map at maximum k_{eff} (ASSBLY-D)

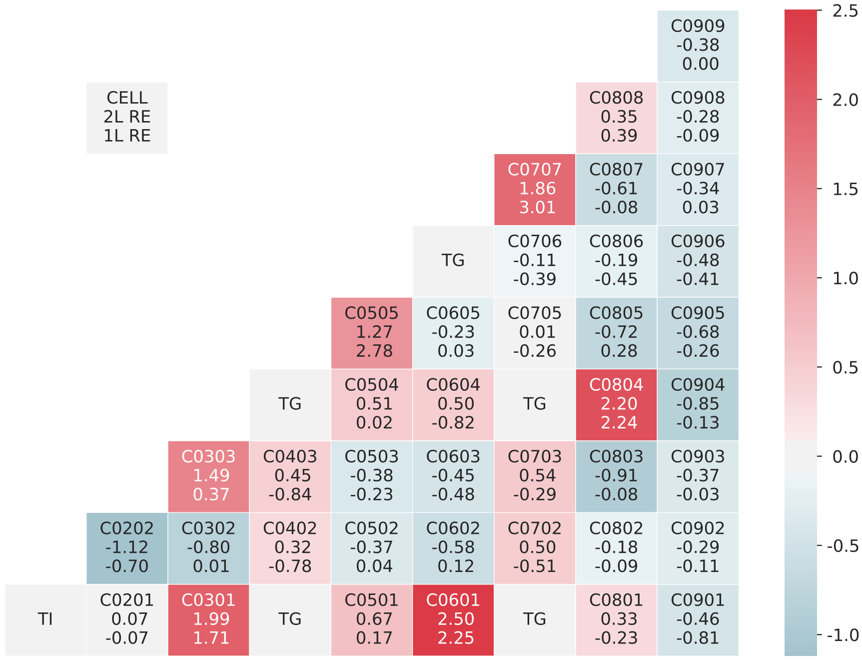

Figure 3.39 Relative discrepancies of the capture reaction map at maximum k_{eff} (ASSBLY-D)

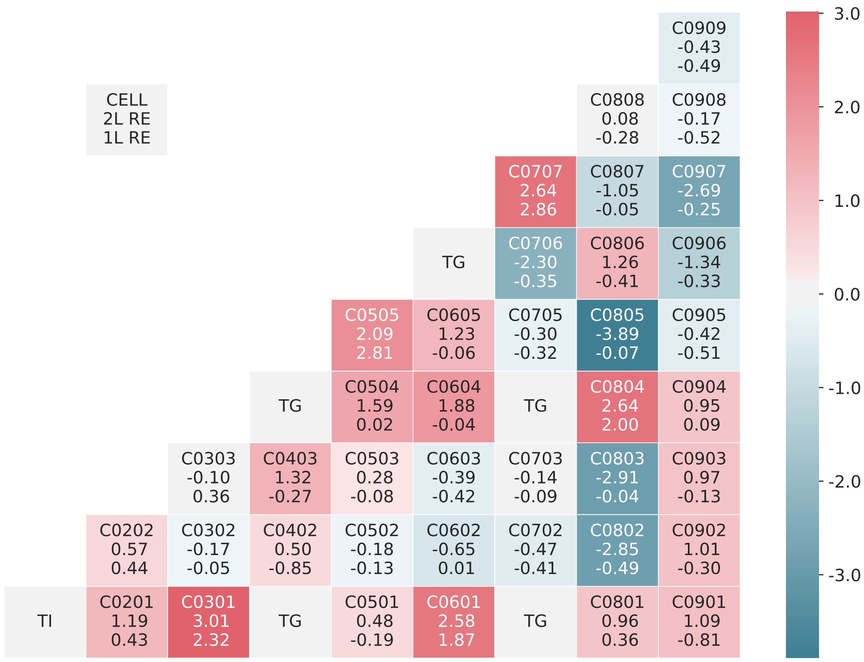

Figure 3.40 Relative discrepancies of the fission reaction map at maximum burnup (ASSBLY-D)

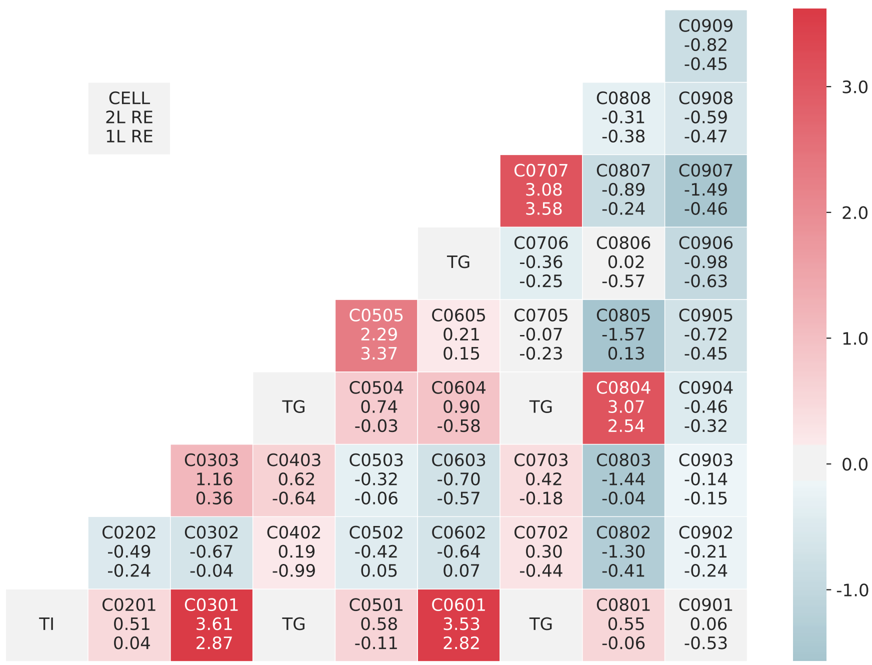

Figure 3.41 Relative discrepancies of the capture reaction map at maximum burnup (ASSBLY-D)

Table 3.14 Maximum and average absolute relative error in fission and capture reaction rates

	Zero BU		**BU at $k_{\mathrm{eff-max}}$**		**Max BU**	
	max %	*ave* %	*max* %	*ave* %	*max* %	*ave* %
ASSBLY-A						
Fission 1*L*	0.41	0.12	-	-	0.48	0.19
Fission 2*L*	0.41	0.14	-	-	2.63	0.73
Capture 1*L*	0.53	0.16	-	-	0.55	0.19
Capture 2*L*	0.83	0.28	-	-	0.91	0.38
ASSBLY-B						
Fission 1*L*	1.97	0.20	1.53	0.31	3.01	0.28
Fission 2*L*	1.88	0.21	2.02	0.54	2.95	0.87
Capture 1*L*	3.66	0.30	1.42	0.26	3.55	0.35
Capture 2*L*	3.21	0.49	1.41	0.43	3.16	0.53
ASSBLY-C						
Fission 1*L*	1.93	0.24	0.57	0.21	3.00	0.39
Fission 2*L*	1.75	0.22	1.59	0.59	2.57	0.88
Capture 1*L*	4.57	0.45	2.50	0.33	3.54	0.46
Capture 2*L*	3.88	0.56	2.18	0.56	3.03	0.59
ASSBLY-D						
Fission 1*L*	1.99	0.34	0.87	0.22	2.86	0.55
Fission 2*L*	1.68	0.34	1.40	0.57	3.89	1.25
Capture 1*L*	3.93	0.60	3.01	0.55	3.58	0.66
Capture 2*L*	3.57	0.70	2.50	0.68	3.61	0.93

3.3.3 Accuracy of one- and two-level computational schemes in Gd pins

In this section we compare the results of ASSBLY-A and ASSBLY-D for both one- and two-level schemes. Larger deviations from SERPENT2 results due to Gd pins are being discussed.

Table 3.15 presents the effective multiplication factor for each of the assembly calculations. This table suggest that due to addition of Gd pins the maximum deviation from SERPENT2 has doubled in both schemes. At the same time the 2L scheme still performs better than 1L scheme. From the table the maximum deviation for ASSBLY-D is about 250 pcm lower for 2L than for 1L scheme.

Table 3.15 k_{eff} and absolute discrepancies for assembly benchmarks

Case	*Burnup* MWd/t	$k_{\text{eff}}(S2)$	$k_{\text{eff 2L}}(D5)$	$\Delta a_{2\text{L}}$ pcm	$k_{\text{eff 1L}}(D5)$	$\Delta a_{1\text{L}}$ pcm
	0.0	1.08069	1.08098	25	1.08012	-49
ASSBLY-A	54.0	0.76166	0.76370	351	0.76426	446
	70.0	0.74192	0.74373	329	0.74427	426
	0.0	1.04956	1.05090	122	1.05046	81
ASSBLY-B	9.5	1.01233	1.00521	-700	1.00316	-903
	70.0	0.74395	0.74397	3	0.74412	31
	0.0	1.07730	1.07843	97	1.07820	78
ASSBLY-C	11.25	1.04568	1.03822	-688	1.03586	-907
	70.0	0.75272	0.75328	99	0.75345	129
	0.0	1.06114	1.06098	-14	1.06144	26
ASSBLY-D	12.75	1.08922	1.08029	-759	1.07735	-1012
	70.0	0.78783	0.78705	-126	0.78925	229

Relative errors of isotopic densities inside all fuel pins are presented in Figures 3.42, 3.43, 3.44, 3.45.

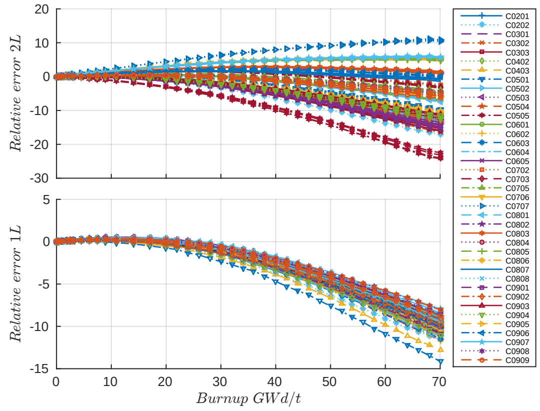

(a) ASSBLY-A

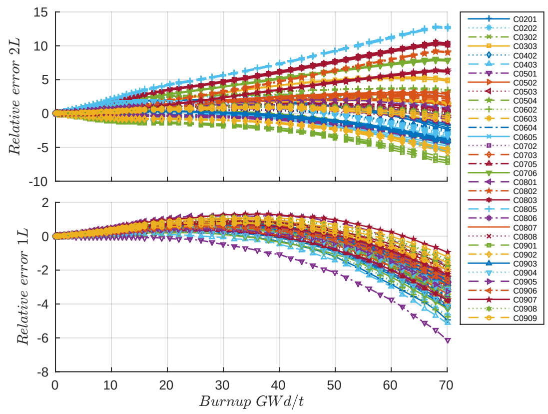

(b) ASSBLY-D (UOX pins)

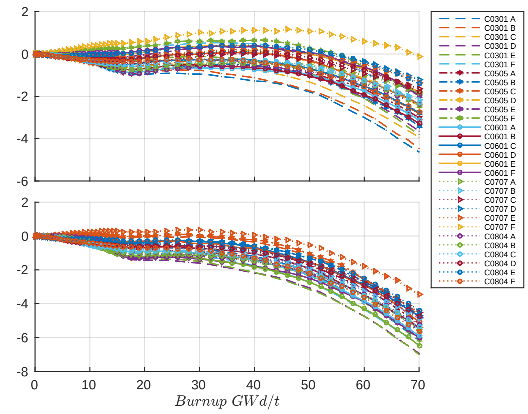

(c) ASSBLY-D (Gd pins)

Figure 3.42 Relative errors in U235 isotopic densities in all rings of all fuel pins

Figure 3.42 suggest that 2L scheme makes the relative error more symmetric. At the same time 1L scheme mostly overestimates the isotopic densities calculated by SERPENT2. Furthermore, in Figure 3.42 for ASSBLY-D we observe maximum error of ≈7% in 1L scheme of a Gd pin. However, the maximum error of ≈13% in 2L scheme is observed inside a UOX pin.

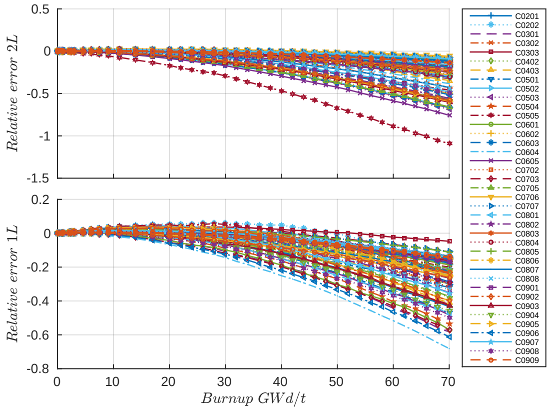

(a) ASSBLY-A

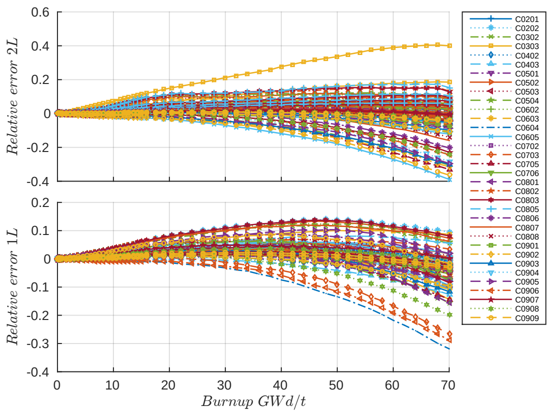

(b) ASSBLY-D (UOX pins)

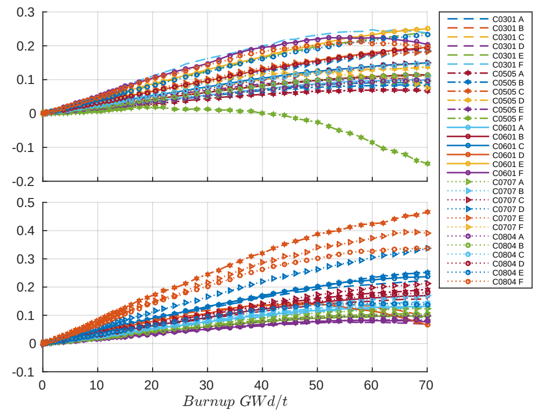

(c) ASSBLY-D (Gd pins)

Figure 3.43 Relative errors in U238 isotopic densities in all rings of all fuel pins

Figure 3.43 suggests that for U238 isotope the maximum error for 1L scheme is in Gd pin, whereas for 2L scheme it is located in UOX pin.

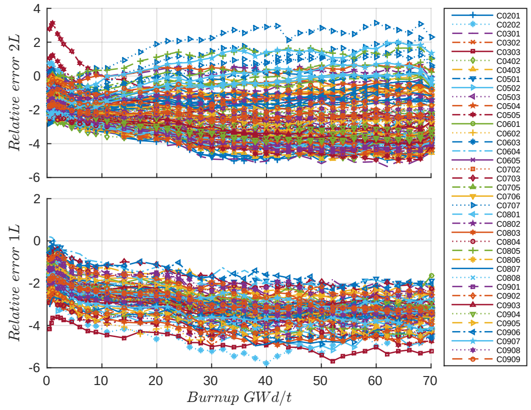

(a) ASSBLY-A

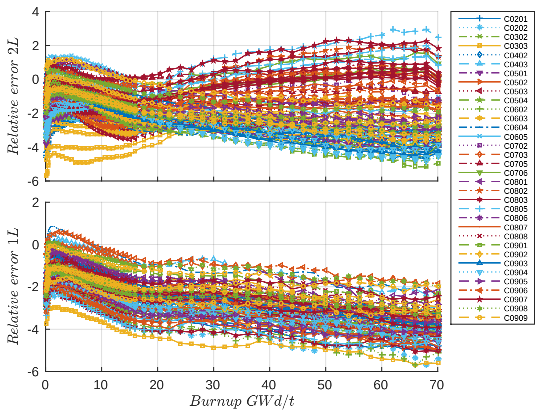

(b) ASSBLY-D (UOX pins)

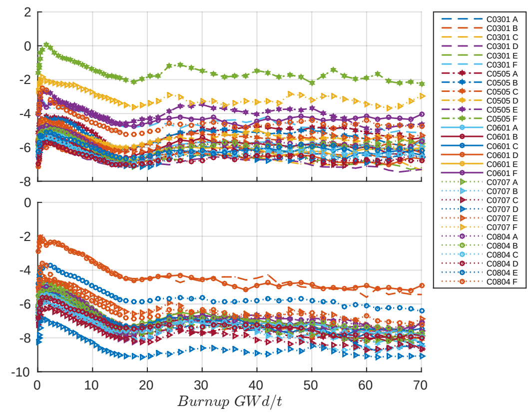

(c) ASSBLY-D (Gd pins)

Figure 3.44 Relative errors in Pu239 atomic densities in all rings of all fuel pins

Figure 3.44 suggests that for 1L scheme DRAGON5 constantly overestimates SERPENT2 in ASSBLY-A. This effect is somewhat shifted up in 2L scheme. Therefore, the accumulative relative error in 2L scheme is lower than in 1L scheme. The same observation is true for ASSBLY-D. We observe maximum relative error inside Gd pins for both schemes. The maximum relative error in UOX pins is about 5% for both schemes, whereas in Gd pins we observe an error of 9% and 7% for 1L and 2L schemes respectively. Overall, for Pu239 isotope the 2L scheme performs better than the 1L scheme. In general, the behaviour of each scheme varies from one isotope to another.

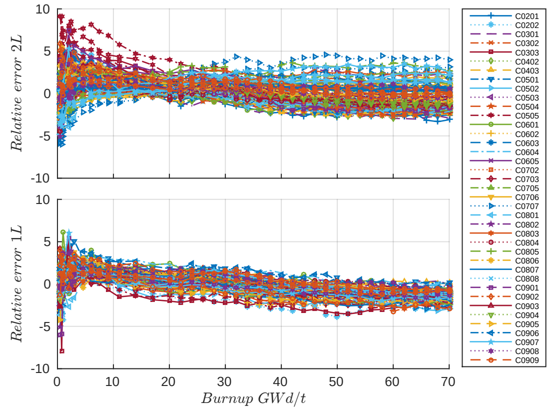

(a) ASSBLY-A

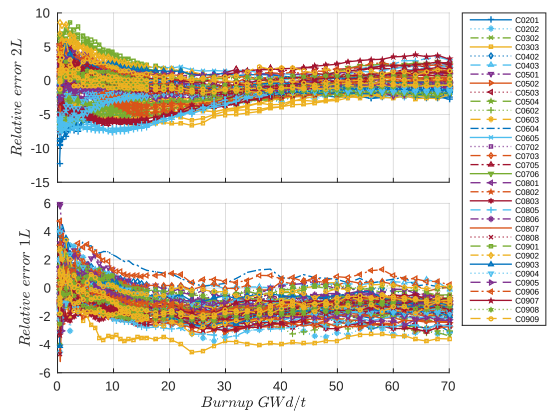

(b) ASSBLY-D (UOX pins)

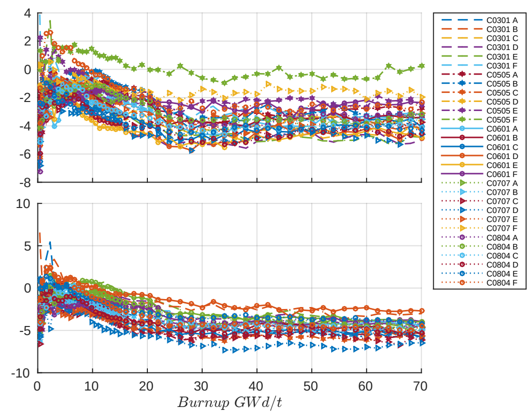

(c) ASSBLY-D (Gd pins)

Figure 3.45 Relative errors in Pu241 atomic densities in all rings of all fuel pins

Figure 3.45 shows that the maximum relative errors in ASSBLY-A are 6% and 7% for 1L and 2L schemes respectively. For ASSBLY-D we observe maximum relative error of about 14% inside UOX pins for 2L schemes. At the same time, for 1L scheme the 9% maximum error is located inside Gd pins.

The above observations are quantitatively supported in Figure 3.46. Here, we can clearly discern that 2L scheme reduces assembly-wise relative error. For Pu241 we observe increase in relative error for 2L scheme up to the point where Gd is fully burned. After this point in time 2L scheme starts recovering and reduces error more efficiently compared to 1L scheme.

Table 3.14 suggests that due to addition of Gd the average absolute relative error has increased in both schemes. At the same time the data shows that 2L scheme has somewhat higher average absolute error than 1L scheme. This observation is in agreement with the behaviour of the isotopic densities shown and discussed above.

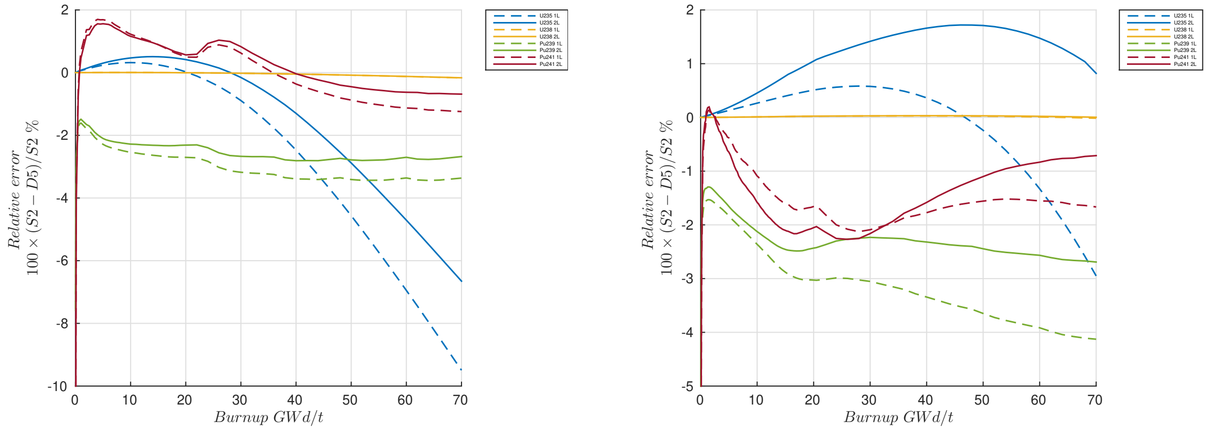

(a) ASSBLY-A (b) ASSBLY-D

Figure 3.46 Assembly-wise average relative errors of atomic densities

Figure 3.47 shows relative errors of assembly-wise averaged densities of fission products. Overall, the maximum average relative error in both assemblies is about 3%. The worst performing isotope is $Sm152$ in ASSBLY-A and $Eu153$ in ASSBLY-D. More detailed observation of relative errors of these two isotopes are shown in Figures 3.48, 3.49. Here we observe that for ASSBLY-A the maximum error of $Sm152$ is about 5% for both schemes. However, there is one ring inside C0505 pin which shows an error of ≈8%. For $Eu153$ isotope inside ASSBLY-A 1L scheme shows a better performance with about 2% error, whereas in 2L scheme the error is about 4%. Nonetheless, the assembly-wise average maximum error for $Eu153$ is about 0.5% for both schemes (Figure 3.47). It is important to note that the assembly-wise average error curves for $Sm152$ and $Eu153$ are almost identical.

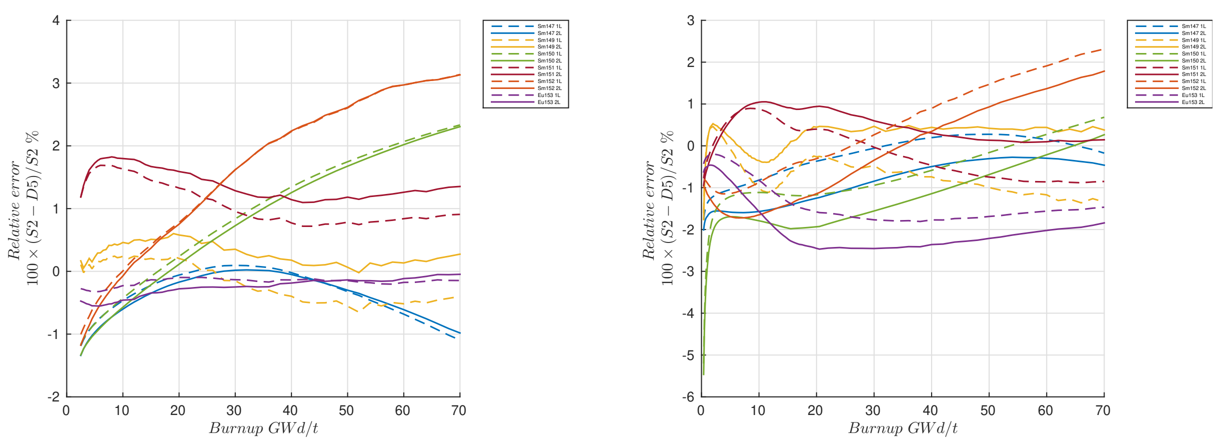

(a) ASSBLY-A (b) ASSBLY-D

Figure 3.47 Assembly-wise average relative errors of atomic densities for fission products

Figures 3.48, 3.49 show that for ASSBLY-D the presence of Gd pins have caused some error spikes in the fuel rings of both schemes. The spikes start to fade away after all Gd has been burned. The worst performing pins of 2L scheme for $Sm152$ and $Eu153$ are the pins which are the adjacent neighbours of the Gd pins.

The plots showing the relative errors of other isotopes and assembly calculations are presented in Appendix G.

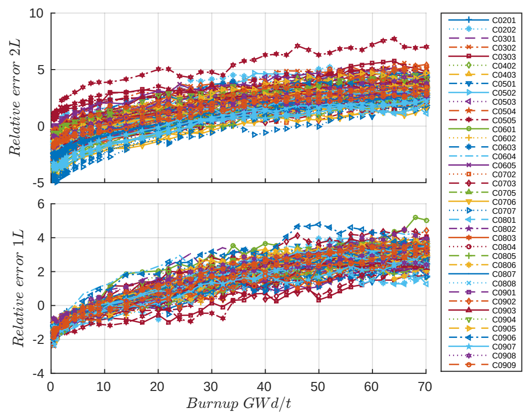

(a) ASSBLY-A Sm152

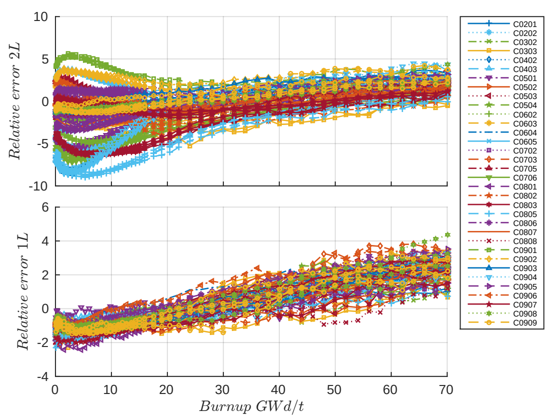

(b) ASSBLY-D Sm152 (UOX pins)

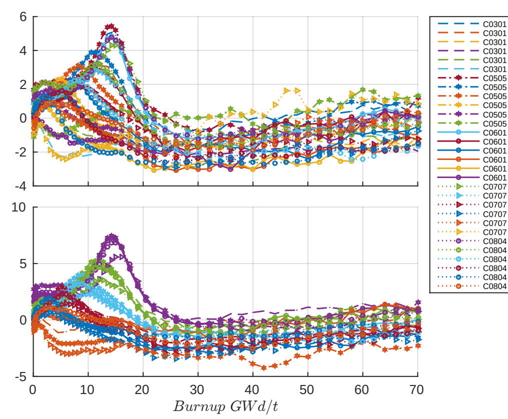

(c) ASSBLY-D Sm152 (Gd pins)

Figure 3.48 Relative errors in Sm152 atomic densities in all rings of all pins

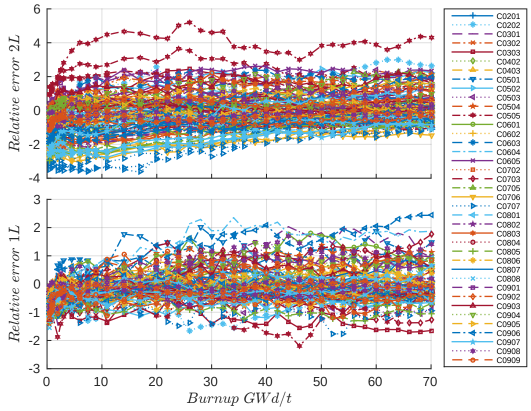

(a) ASSBLY-A Eu153

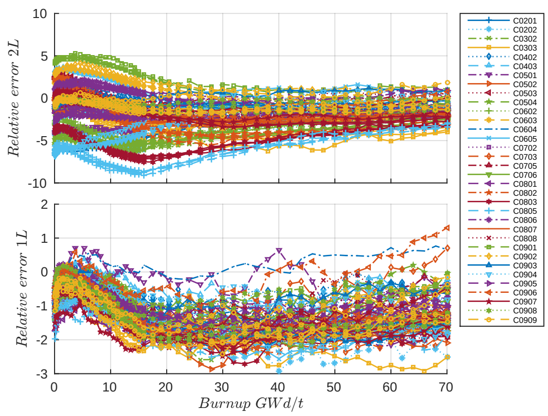

(b) ASSBLY-D Eu153 (UOX pins)

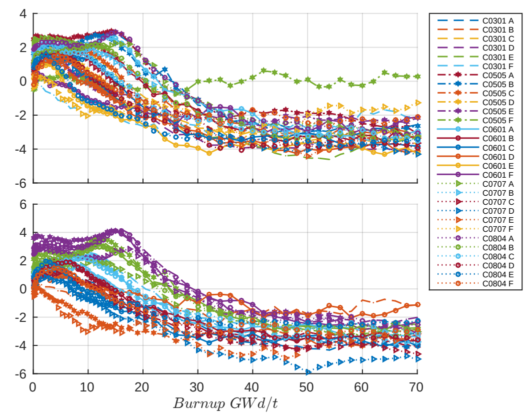

(c) ASSBLY-D Eu153 (Gd pins)

Figure 3.49 Relative errors in Eu153 atomic densities in all rings of all pins

Here we present the absolute relative errors of fission and capture reaction rates in ASSBLY-A and ASSBLY-D using step plots. We observe in Figure 3.50 that the fission rate error at zero burnup is about 0.4% in ASSBLY-A and about 2% in ASSBLY-D. Here, both 1L and 2L schemes perform closely without any observable differences. Furthermore, for ASSBLY-D the worst performing pins are those containing Gd. These Gd pins are responsible for the increase of relative error from less than 0.5% up to 2% (Figure 3.50 (b)). For capture rates in ASSBLY-A at zero burnup we observe clear difference between two schemes. Overall, maximum relative error for 2L scheme is ≈0.8% compared to ≈0.5% of 1L scheme. At the same time capture rates in ASSBLY-D show almost no difference between 1L and 2L schemes. Furthermore, the relative error is ≈4.0% due to presence of Gd pins.

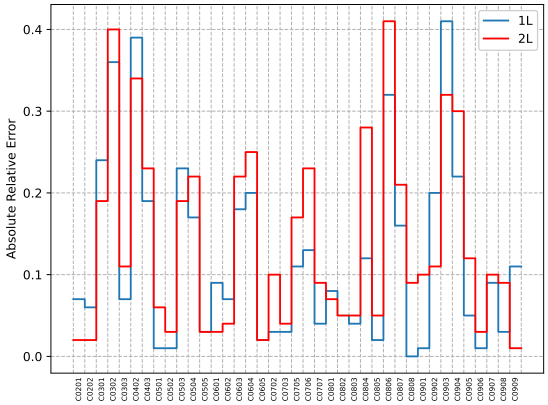

(a) ASSBLY-A fission rate

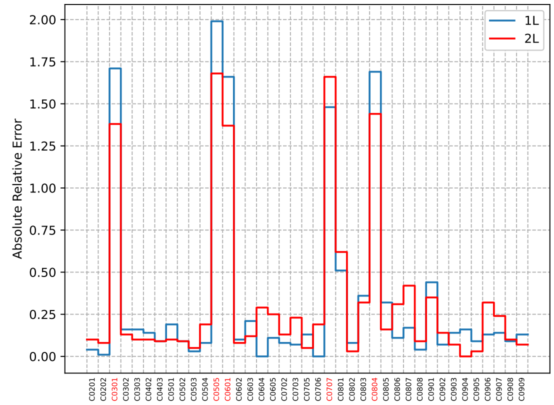

(b) ASSBLY-D fission rate

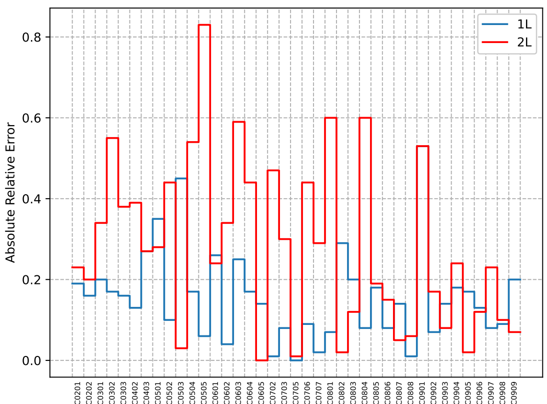

(c) ASSBLY-A capture rate

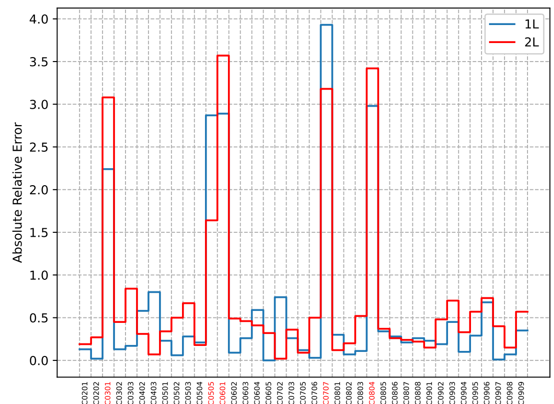

(d) ASSBLY-D capture rate

Figure 3.50 Relative errors in fission and capture rates in assembly pins at zero burnup

Relative errors of fission and capture reaction rates at maximum burnup are shown in Figure 3.51. Relative error of fission rate in ASSBLY-A shows clear distinction between 1L and 2L schemes. 1L scheme provides less than 0.5% error compared to ≈2.5% of 2L scheme. Relative error of capture rate in ASSBLY-A is quit similar to the case of zero burnup (Figure 3.50 (c)) and shows some minor degradation in 2L scheme. Relative error of fission rate in ASSBLY-D has degraded up to 3-4% compared to 2% at zero burnup. Here we observe that for 2L scheme the errors have spread away from Gd pins, whereas for 1L scheme the errors stayed local to Gd pins. In 1L scheme Gd pins are responsible for the increase of error from 0.5% up to 3%. For capture rates in ASSBLY-D at maximum burnup we again observe localized errors at Gd pins of ≈3.5%. Also, there is a small degradation in the results of 2L scheme compared to 1L scheme.

The relative errors of fission and capture rates at maximum k_{eff} for ASSBLY-D are shown in

Figure 3.52. The results are fairly similar to the ones discussed above.

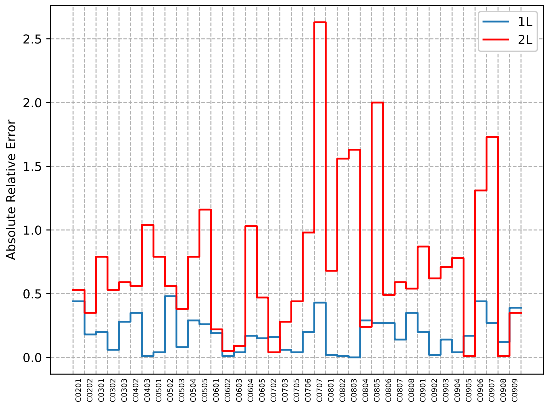

(a) ASSBLY-A fission rate

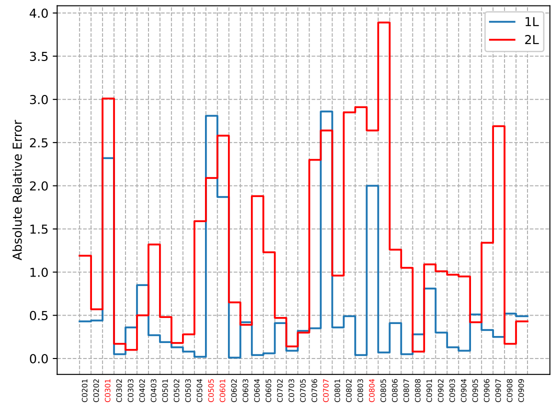

(b) ASSBLY-D fission rate

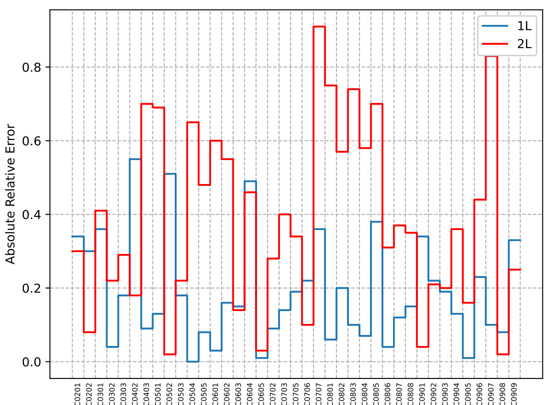

(c) ASSBLY-A capture rate

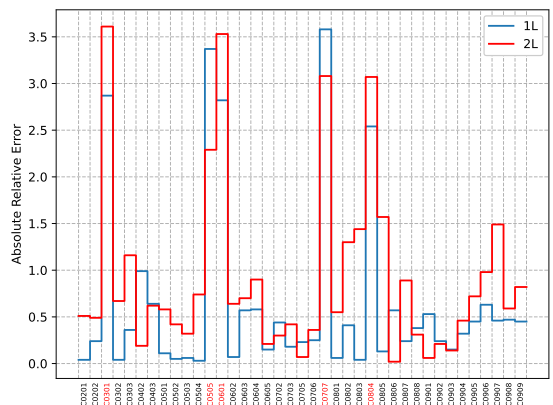

(d) ASSBLY-D capture rate

Figure 3.51 Relative errors in fission and capture rates in assembly pins at maximum burnup

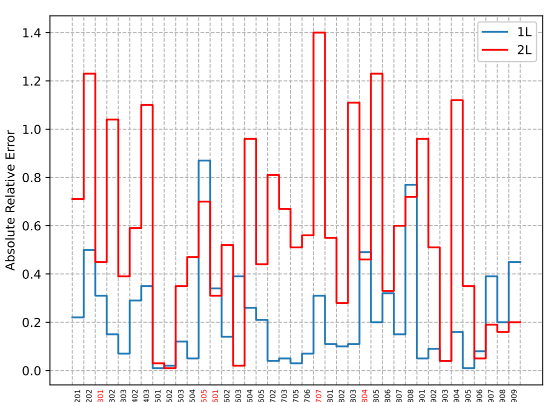

(a) ASSBLY-D fission rate

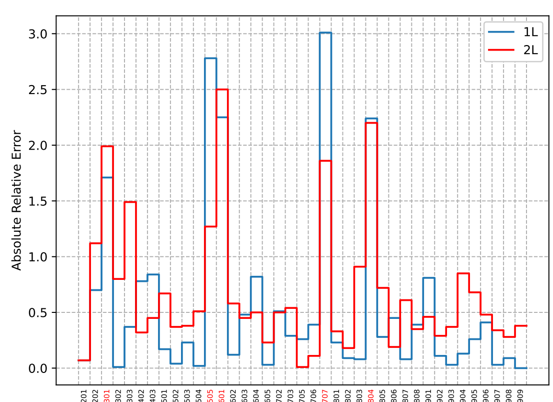

(b) ASSBLY-D capture rate

Figure 3.52 Relative errors in fission and capture rates in assembly pins at maximum k_{eff}

CHAPTER 4 CONCLUSION

4.1 Summary

A benchmark problem suite designed for light water reactors with extended high burnup fuels was used to validate DRAGON5 two-level and one-level calculation schemes using SERPENT2 code. The benchmark consists of 7 problems from which 4 are PWR UOX fuel assembly calculations with and without Gd pins. The other 3 are UOX fuel pin calculations. Here we compare DRAGON5 two-level calculation scheme with the one-level scheme and those of SERPENT2 Monte Carlo code. The validation results are presented by comparing multiplication factor, atomic densities and fission/capture reaction rates at different burnups.

The two-level scheme accelerates the overall burnup calculation about 2-3 times, yet providing accuracy comparable to the results of one-level scheme. The acceleration is due to the use of MOC method on an energy mesh with 26 groups.

Pin-cell calculations show excellent agreement between SERPENT2 and DRAGON5. Here we observe a maximum discrepancy between multiplication factors of ≈300pcm. Simultaneously, for isotopic densities the maximum relative error is below 5.5%.

Table 4.1 Maximum discrepancies of k_{eff} in assembly calculations

Case	$\Delta a_{2\mathrm{L\ MAX}}$	$\Delta a_{1\mathrm{L\ MAX}}$
ASSBLY-A	351	446
ASSBLY-B	-700	-903
ASSBLY-C	-688	-907
ASSBLY-D	-759	-1012

Assembly calculations show reasonable agreement with UOX fuels without Gd pins (Table 4.1). Fission and capture rates for UOX assemblies without Gd pins show less than 1% of maximum relative error for both schemes (Table 3.14). Overall, the optimized two-level scheme is capable of performing a PWR assembly calculation essentially faster without any significant loss of calculation precision.

4.2 Limitations

The assembly calculations containing Gd pins show overall degradation of the results. The atomic densities inside specific fuel rings of some transuranic isotopes show relative errors of ≈13% in two-level scheme and ≈10% in one-level scheme. The k_{eff} multiplication factor shows a deviation from SERPENT2 of ≈800pcm for two-level scheme and ≈1000pcm for one-level scheme. Meanwhile, the divergences of multiplication factors go below 100pcm when the Gd isotopes are fully consumed.

The maximum relative error in fission and capture rates peaks at 4-5% as shown in Table 3.14 for all assembly calculations with Gd pins. Meanwhile, the error is less than 1% for UOX only assembly.

A similar research was published by Canbakan [2]. The author reports about 550pcm discrepancy of multiplication factor for a somewhat similar PWR assembly simulation using the 2L scheme and 1.5 Gd pins. The closest case in our benchmark suit is ASSBLY-C with 1.5 Gd pins. Here the maximum divergence was about 700pcm. The difference can be explained due to multiple factors, such as the relative close positioning of Gd pins. Another factor is that the isotopic vector of Gd pins used by Canbakan is ≈9% lower than in ASSBLY-C. The article also reports about 20% divergence for Pu239 isotope at the end of the burnup in a specific pin. For ASSBLY-C we observe maximum deviation of ≈9.5% in a Gd pin (Table 4.2).

Thus, the study shows that the presence of gadolinium results in overall degradation of both 1L and 2L schemes.

Table 4.2 Maximum relative errors of Pu239 in assembly calculations

Case	$1L(\%)$	$2L(\%)$
CANBAKAN	-	20
ASSBLY-A	6	5
ASSBLY-B	9	8
ASSBLY-C	9.5	8
ASSBLY-D	9	7

4.3 Future Research

This study clearly show that the presence of Gd isotopes in specific pins causes overall assembly-wise degradation of both one- and two-level schemes. Thus a work should be done to identify and fix the major deviation factors due to Gd isotopes in DRAGON5 calculations. Both 1L and 2L computational schemes should be fixed accordingly. The 1L and 2L computational schemes may easily be completed including leakage effects due to buckling and branching calculations for a set of local parameter variations around each nominal burnup point. Such a variation was recently investigated for the BEAVRS benchmark by Fröhlicher et al. [21]. Finally, the effect of the errors on Gd isotope representation at the PWR full-core simulation level should be investigated.

REFERENCES

[1] A. Hébert, "DRAGON5 and DONJON5, the contribution of École polytechnique de montréal to the SALOME platform," vol. 87, pp. 12–20. [Online]. Available: https://doi.org/10.1016/j.anucene.2015.02.033

[2] A. Canbakan and A. Hébert, "Accuracy of a 2-level scheme based on a subgroup method for pressurized water reactor fuel assembly models," *Ann. Nucl. Energy*, vol. 81, pp. 164–173, 07 2015. [Online]. Available: https://doi.org/10.1016/j.anucene.2015.03.034

[3] J. Leppänen, "Development of a new Monte Carlo reactor physics burnup calculation code," PhD thesis, Helsinki University of Technology, Espoo,Finland, 2011. [Online]. Available: http://lib.tkk.fi/Diss/2007/isbn9789513870195/isbn9789513870195.pdf

[4] J. Leppänen *et al.*, "The Serpent Monte Carlo code: Status, development and applications in 2013," vol. 82, pp. 142–150. [Online]. Available: https://doi.org/10.1016/j.anucene.2014.08.024

[5] A. Hébert, *Applied Reactor Physics*, 2nd ed. Presses internationales Polytechnique, 2016.

[6] Serpent - a Monte Carlo reactor physics burnup calculation code. [Online]. Available: http://montecarlo.vtt.fi/

[7] J. R. Askew, "A characteristics formulation of the neutron transport equation in complicated geometries." [Online]. Available: http://inis.iaea.org/Search/search.aspx?orig_q=RN:38027599

[8] A. Hébert, "Acceleration of step and linear discontinuous schemes for the method of characteristics in DRAGON5," vol. 49, no. 6, pp. 1135–1142. [Online]. Available: http://www.sciencedirect.com/science/article/pii/S1738573317303893

[9] R. M. Ferrer and J. D. R. III, "A linear source approximation scheme for the method of characteristics," vol. 182, no. 2, pp. 151–165. [Online]. Available: https://doi.org/10.13182/NSE15-6

[10] Y. Saad and M. Schultz, "GMRES: A generalized minimal residual algorithm for solving nonsymmetric linear systems," vol. 7, no. 3, pp. 856–869. [Online]. Available: https://epubs.siam.org/doi/abs/10.1137/0907058

[11] N. Lyoussi-Charrat, "Calcul de transport neutronique dans le code APOLLO2 par la méthode des probabilités de collision dans une géométrie cartésienne générale," 1994. [Online]. Available: https://www.polymtl.ca/merlin/downloads/Lyoussi_Charrat_thesis.pdf

[12] A. Hébert and G. Mathonnière, "Development of a third-generation superhomogénéisation method for the homogenization of a pressurized water reactor assembly," *Nuclear Science and Engineering*, vol. 115, no. 2, pp. 129–141, 1993. [Online]. Available: https://doi.org/10.13182/NSE115-129

[13] H. Noureddine, "Nouvelle méthodologie de calcul de l'absorption résonnante," thèse de doctorat, Université Louis Pasteur Strasbourg, France, Strasbourg, France, 2006. [Online]. Available: https://www.polymtl.ca/merlin/downloads/thesis_SHEM.pdf

[14] A. Hébert, "Development of the subgroup projection method for resonance self-shielding calculations," vol. 162, no. 1, pp. 56–75, publisher: Taylor & Francis. [Online]. Available: https://www.tandfonline.com/doi/10.13182/NSE162-56

[15] J.-F. Vidal *et al.*, "New modelling of LWR assemblies using the APOLLO2 code package," in *Proc. Joint Int. Top. Mtg. on Mathematics & Computation and Supercomputing in Nuclear Applications (M&C + SNA 2007)*, Monterey, California, USA, 15-19 april 2007. [Online]. Available: http://inis.iaea.org/Search/search.aspx?orig_q=RN:42109242

[16] R. M. Ferrer *et al.*, "CASMO5, a fuel assembly burnup program methodology manual," Tech. Rep. Proprietary SSP-08/405 Rev 3, 2014.

[17] G. Marleau, A. Hébert, and R. Roy, "A user guide for DRAGON Version5," École Polytechnique de Montréal, Tech. Rep., 05 2020. [Online]. Available: https://www.polymtl.ca/merlin/downloads/IGE335.pdf

[18] A. Yamamoto *et al.*, "Benchmark problem suite for reactor physics study of LWR next generation fuels," vol. 39, no. 8, pp. 900–912, publisher: Taylor & Francis. [Online]. Available: https://doi.org/10.1080/18811248.2002.9715275

[19] J.-F. Vidal *et al.*, "New modelling of LWR assemblies using the APOLLO2 code package," United States, 04 2007. [Online]. Available: http://inis.iaea.org/search/search.aspx?orig_q=RN:42109242

[20] DRAGON5 web site. [Online]. Available: https://www.polymtl.ca/merlin/version5.htm

[21] V. S. K. Fröhlicher and A. Hébert, “Investigating fission distribution behavior under various homogenization techniques for asymmetrical fuel assemblies and different reflector equivalence methods,” 2020, accepted for publication in Ann. Nucl. Energy.

APPENDIX A DRAGON5 ASSEMBLY MAPS

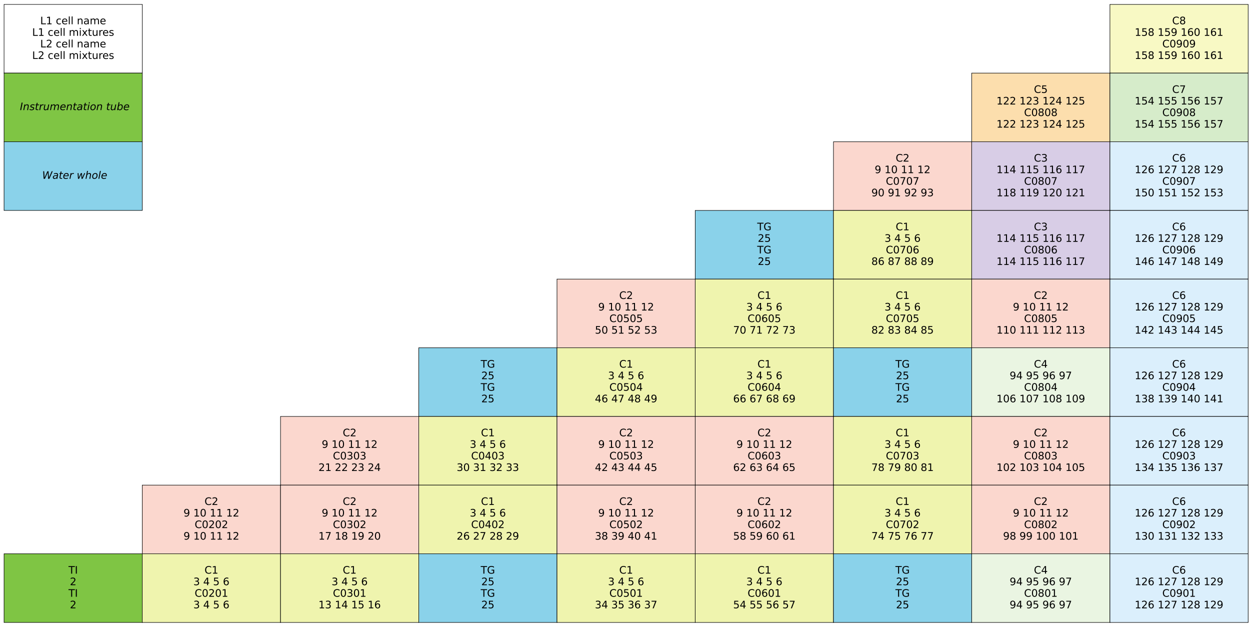

Figure A.1 2 level mixture map for ASSBLY-A

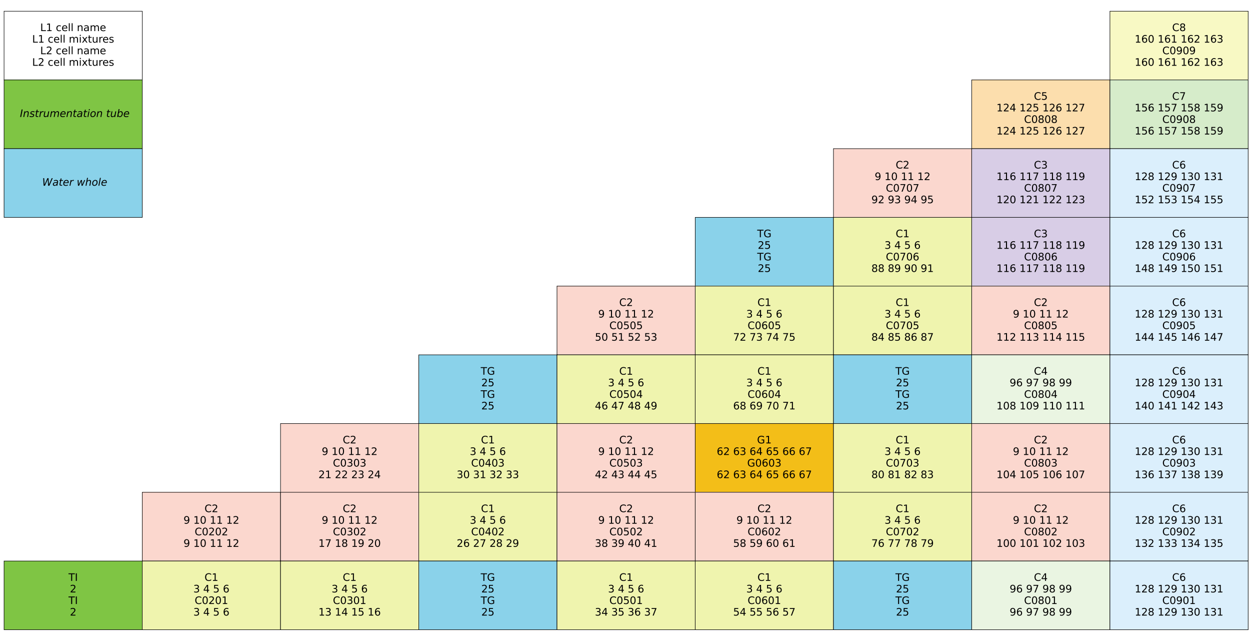

Figure A.2 2 level mixture map for ASSBLY-B

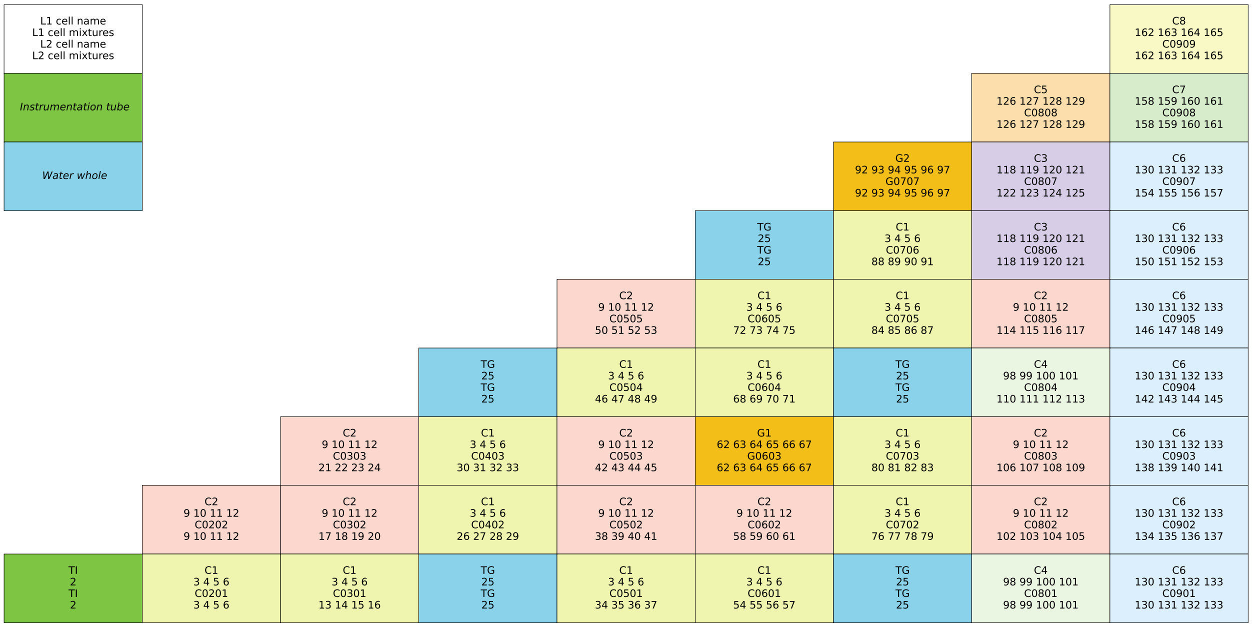

Figure A.3 2 level mixture map for ASSBLY-C

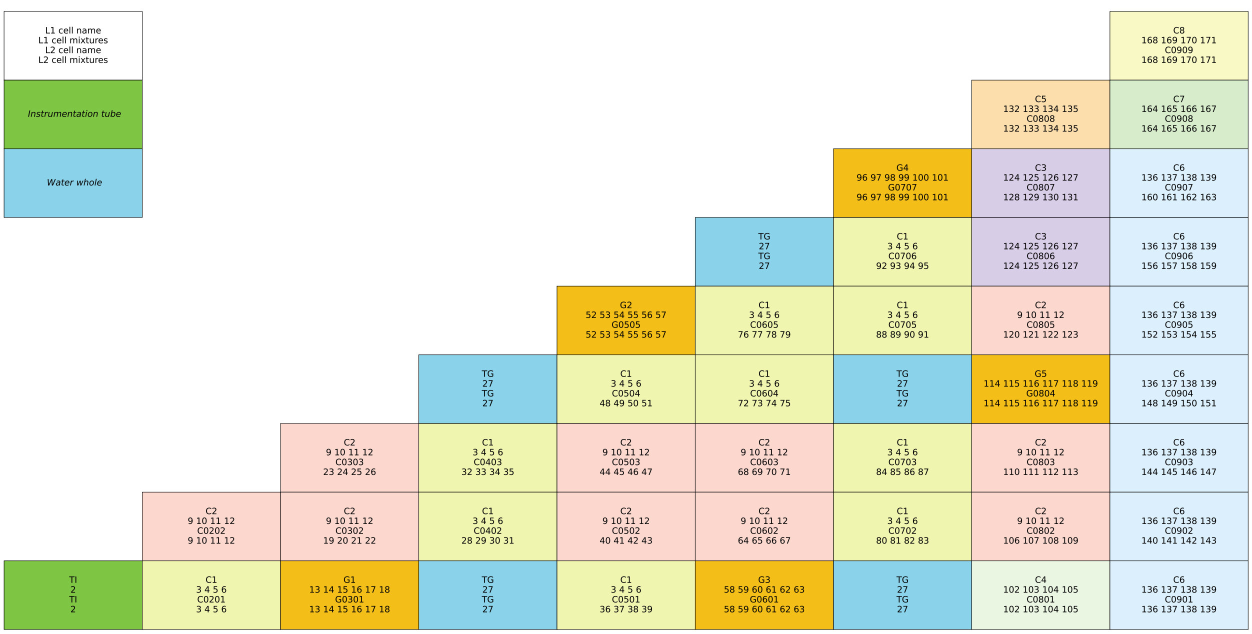

Figure A.4 2 level mixture map for ASSBLY-D

APPENDIX B PIN-A CALCULATION RESULTS

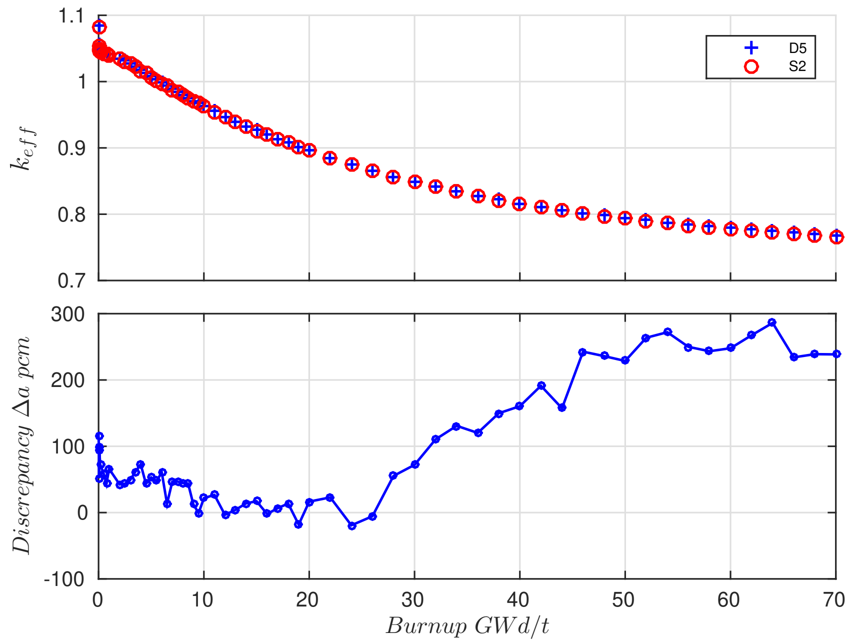

Figure B.1 Evolution of k_{eff} (PIN-A)

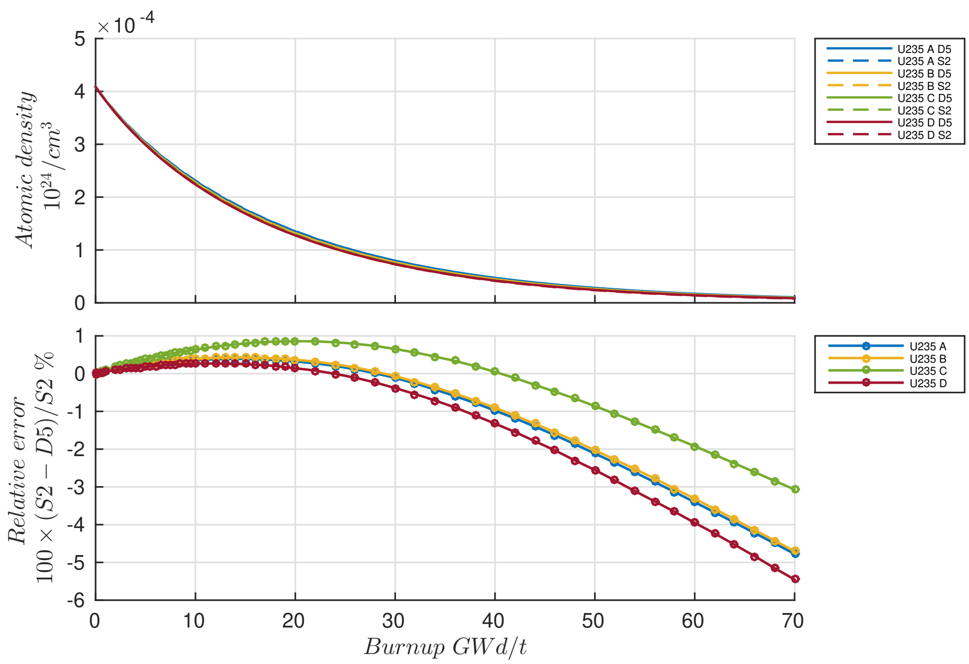

Figure B.2 Atomic density of ^{235}U (PIN-A)

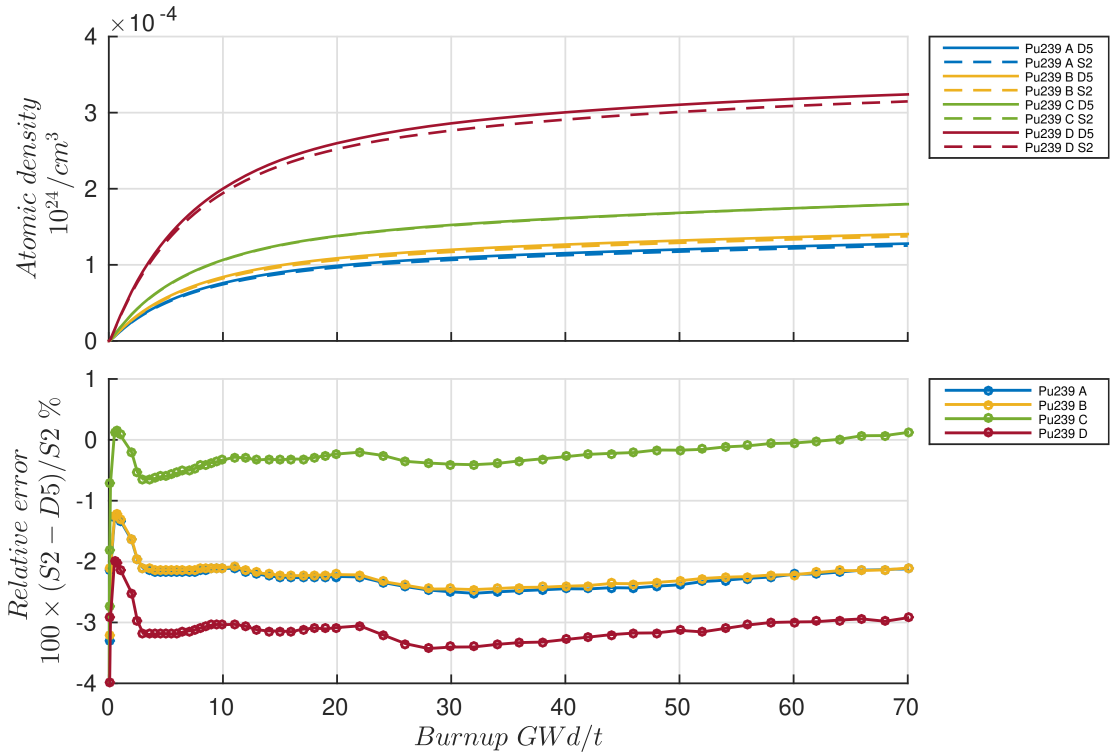

Figure B.3 Atomic density of ^{239}Pu (PIN-A)

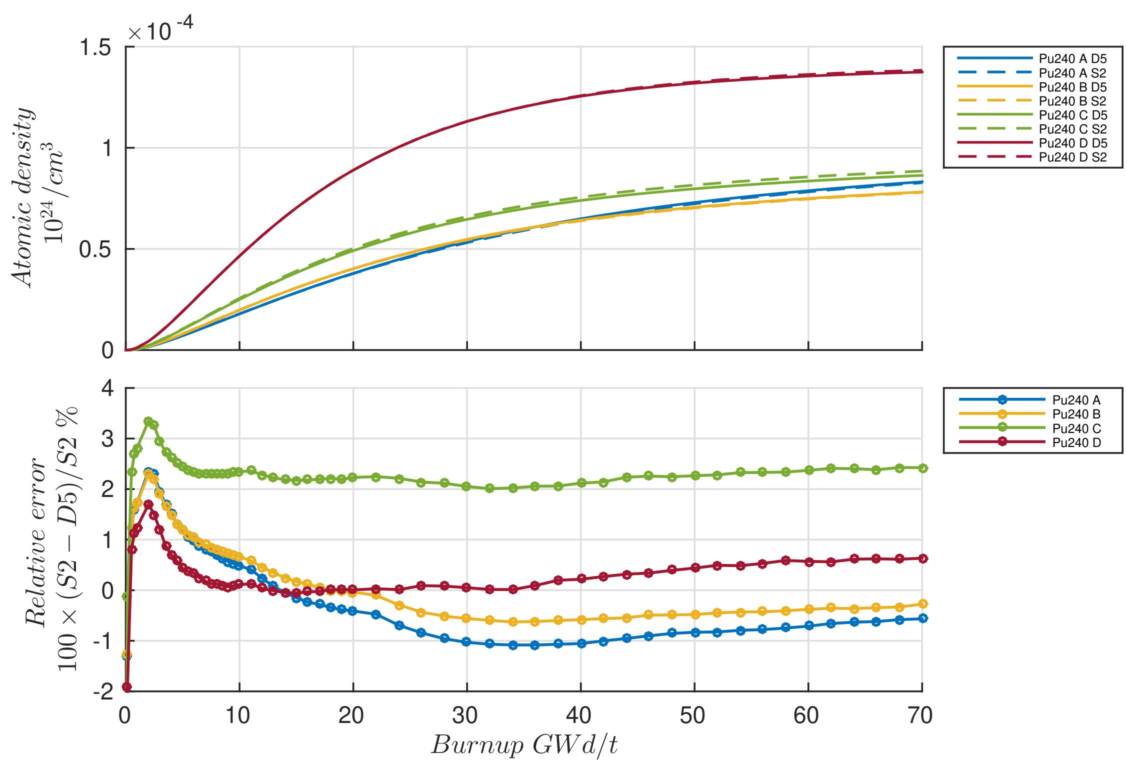

Figure B.4 Atomic density of ^{240}Pu (PIN-A)

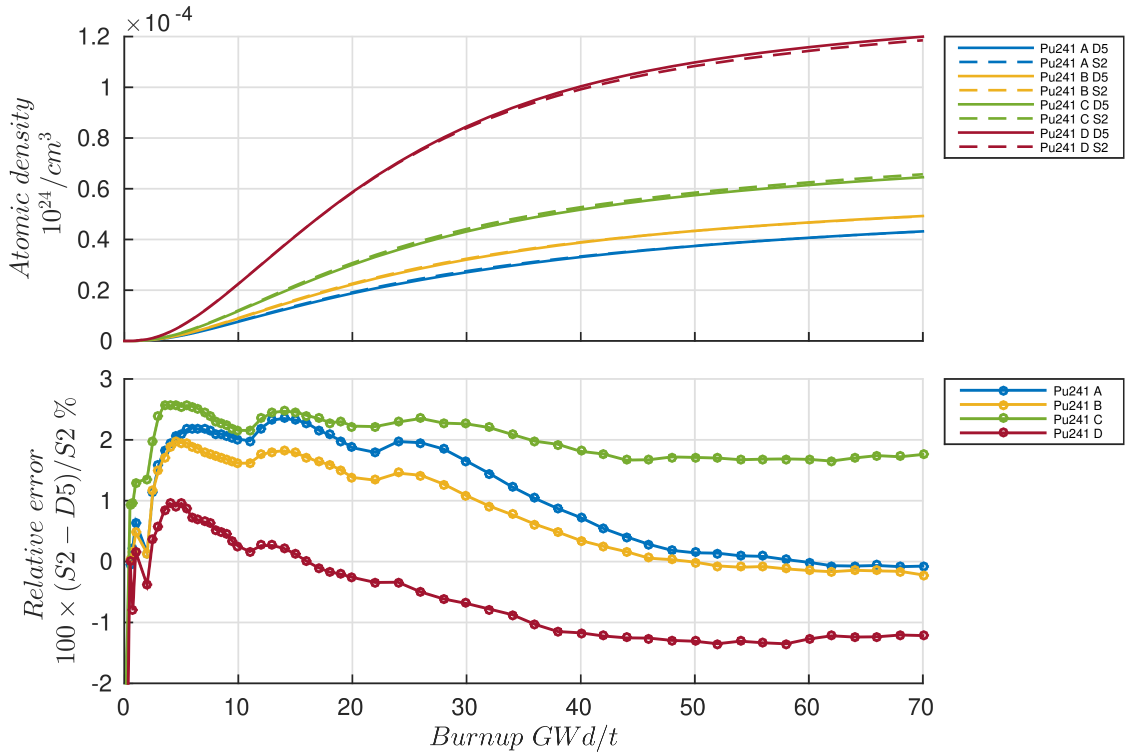

Figure B.5 Atomic density of ^{241}Pu (PIN-A)

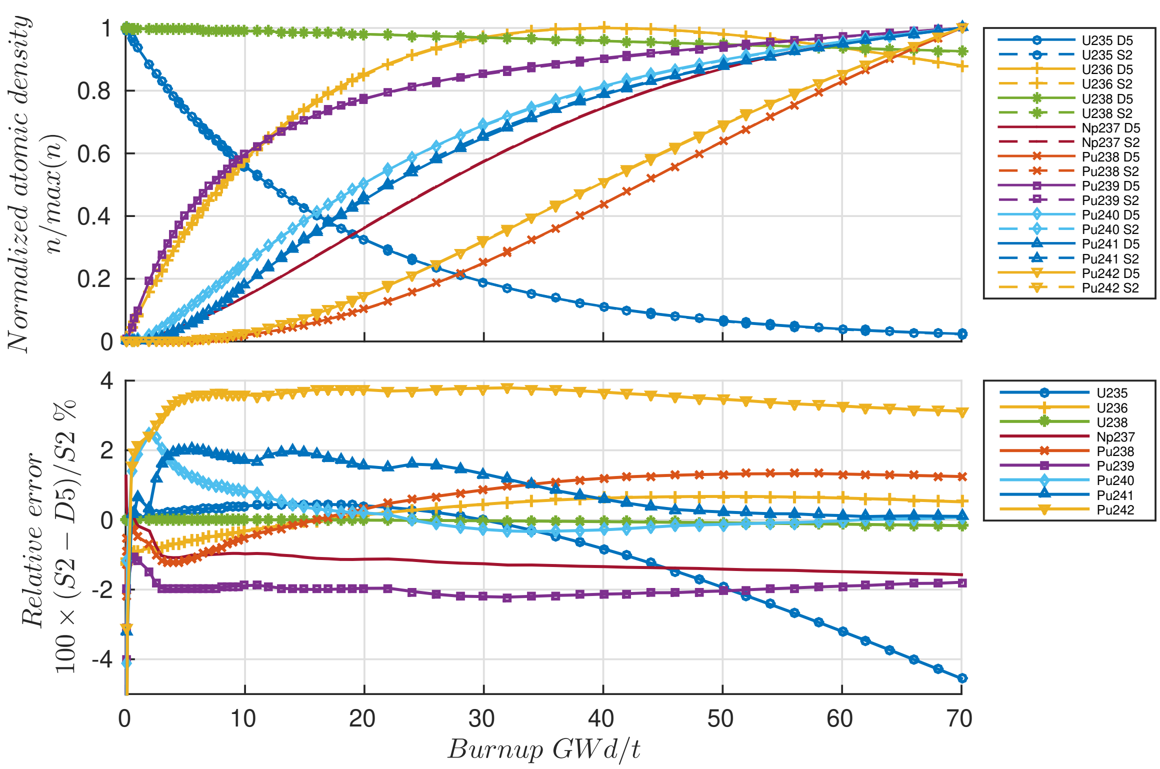

Figure B.6 Pin-wise average density of actinides (PIN-A)

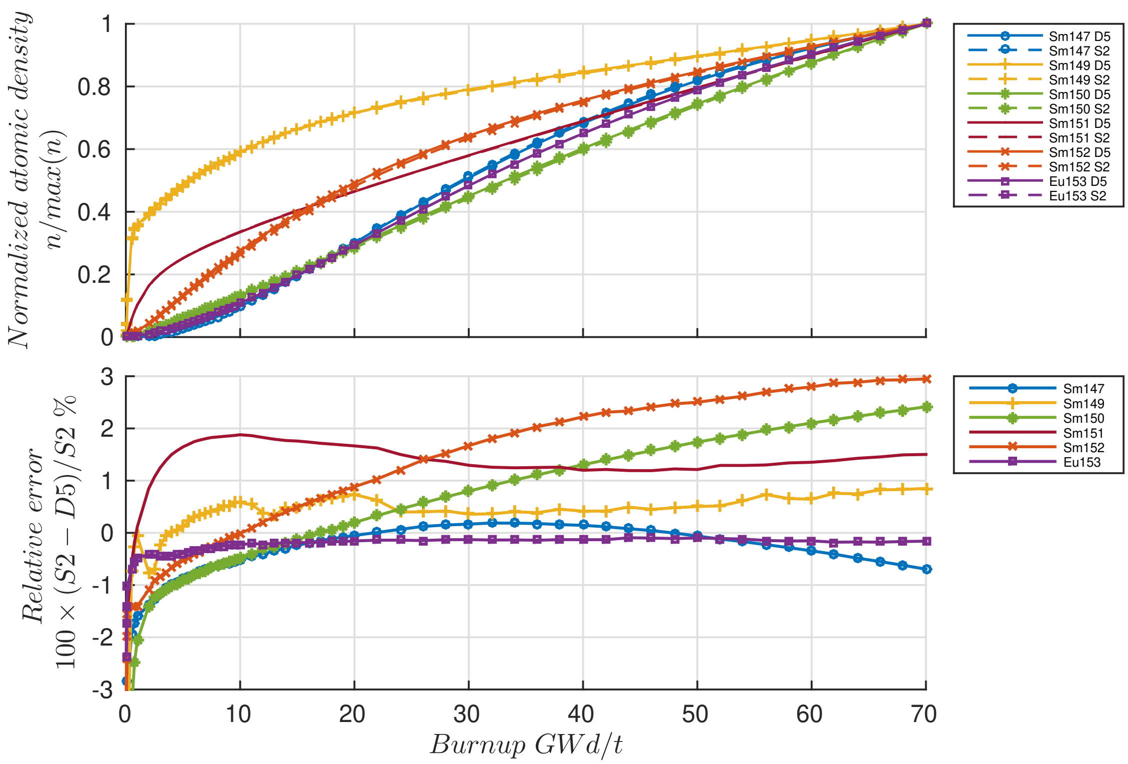

Figure B.7 Pin-wise average density of fission products (PIN-A)

APPENDIX C PIN-B CALCULATION RESULTS

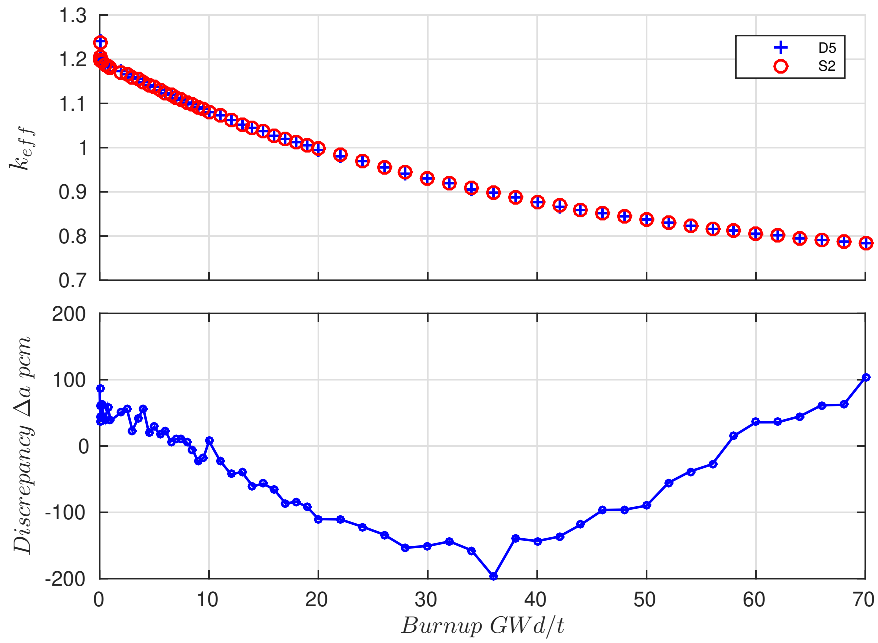

Figure C.1 Evolution of k_{eff} (PIN-B)

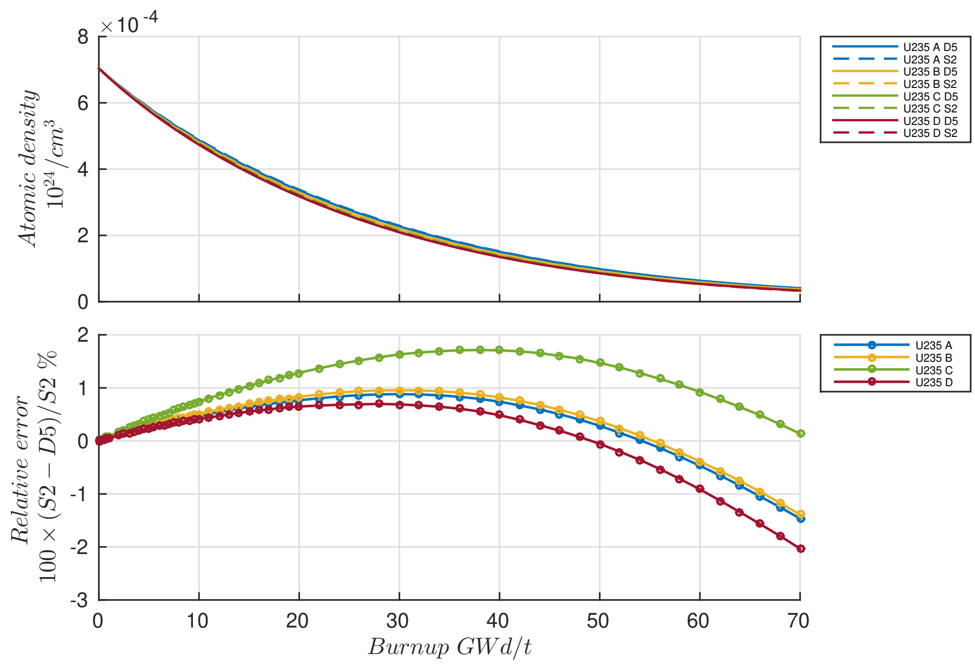

Figure C.2 Atomic density of ^{235}U (PIN-B)

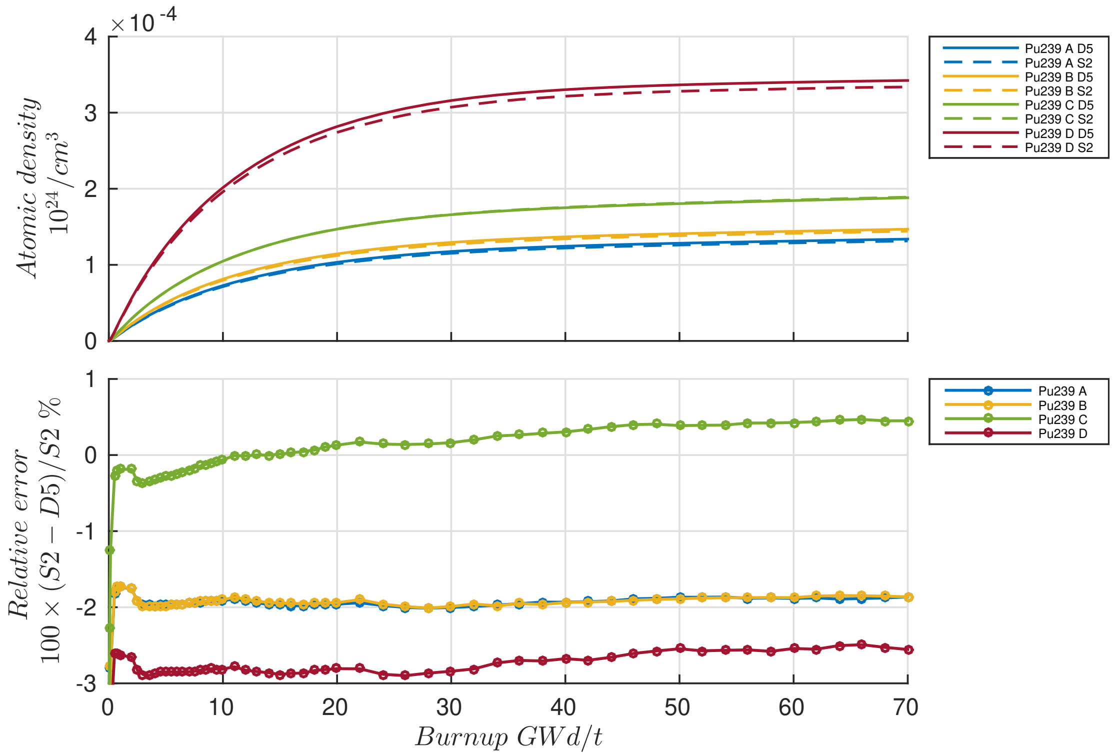

Figure C.3 Atomic density of ^{239}Pu (PIN-B)

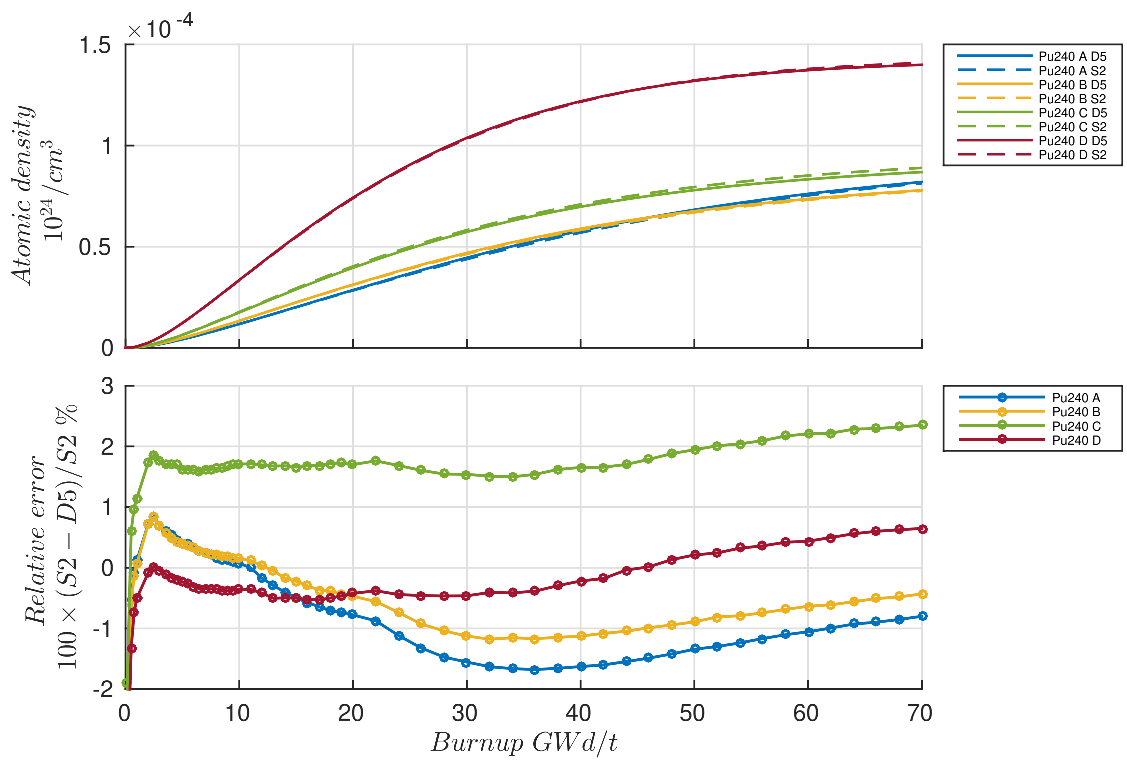

Figure C.4 Atomic density of ^{240}Pu (PIN-B)

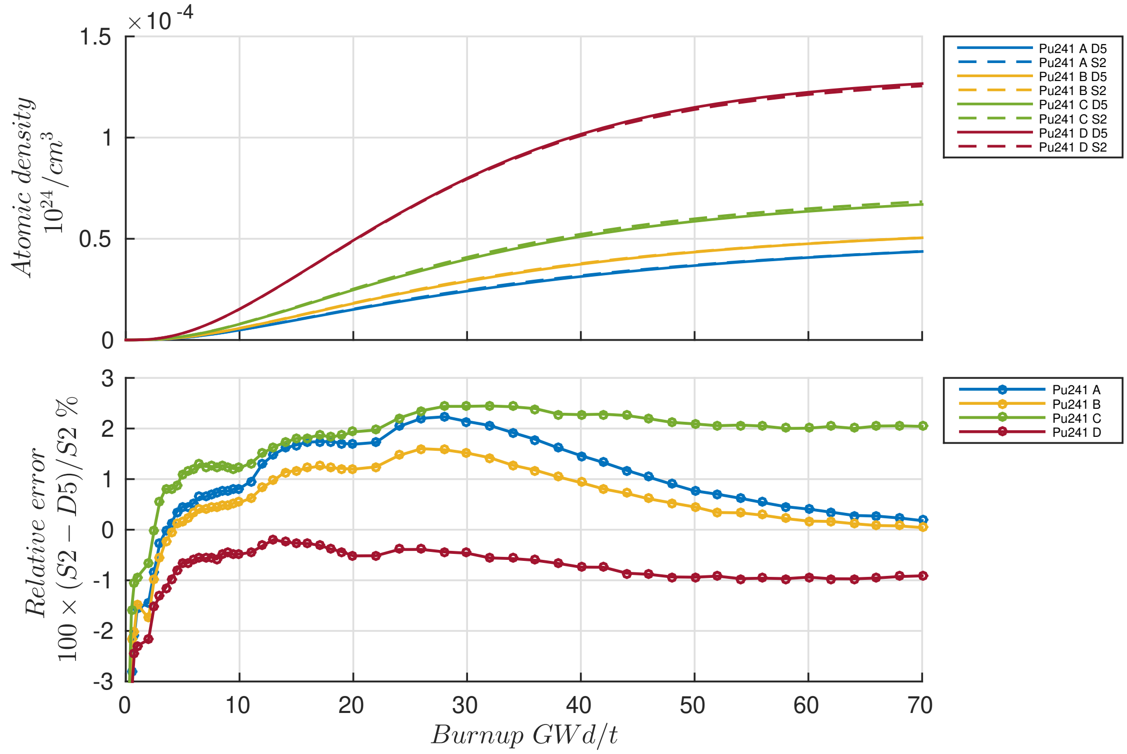

Figure C.5 Atomic density of ^{241}Pu (PIN-B)

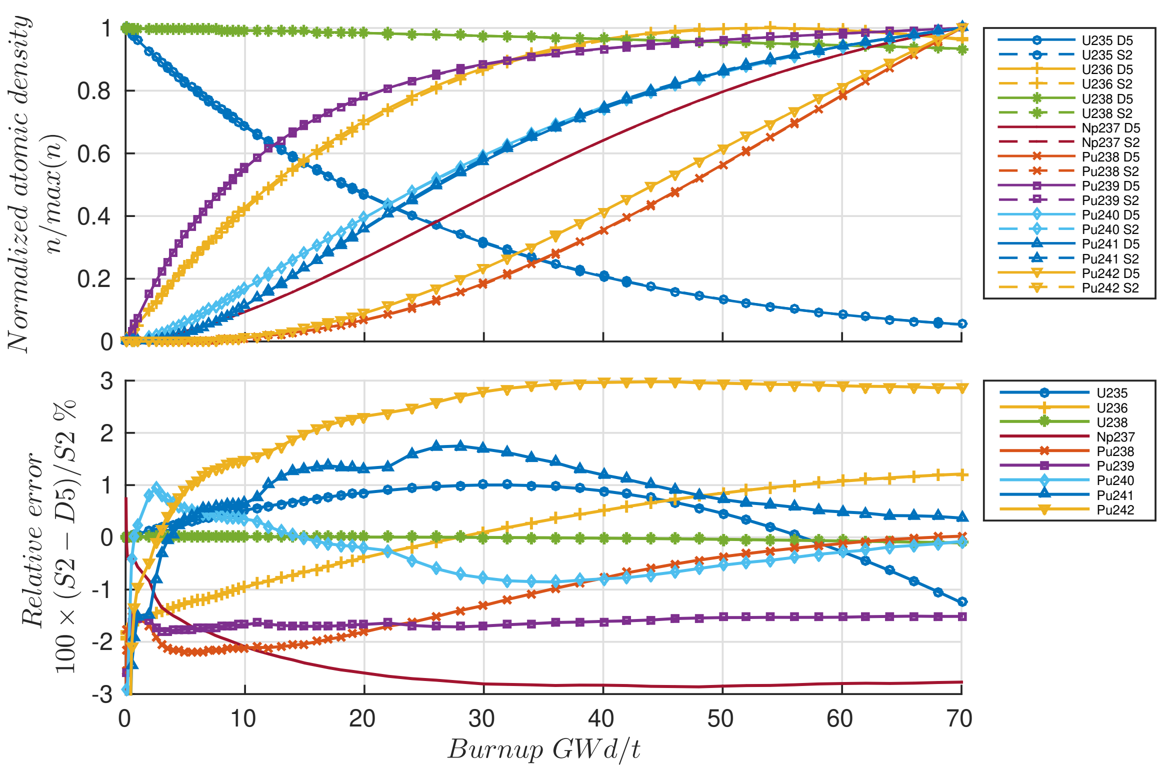

Figure C.6 Pin-wise average density of actinides (PIN-B)

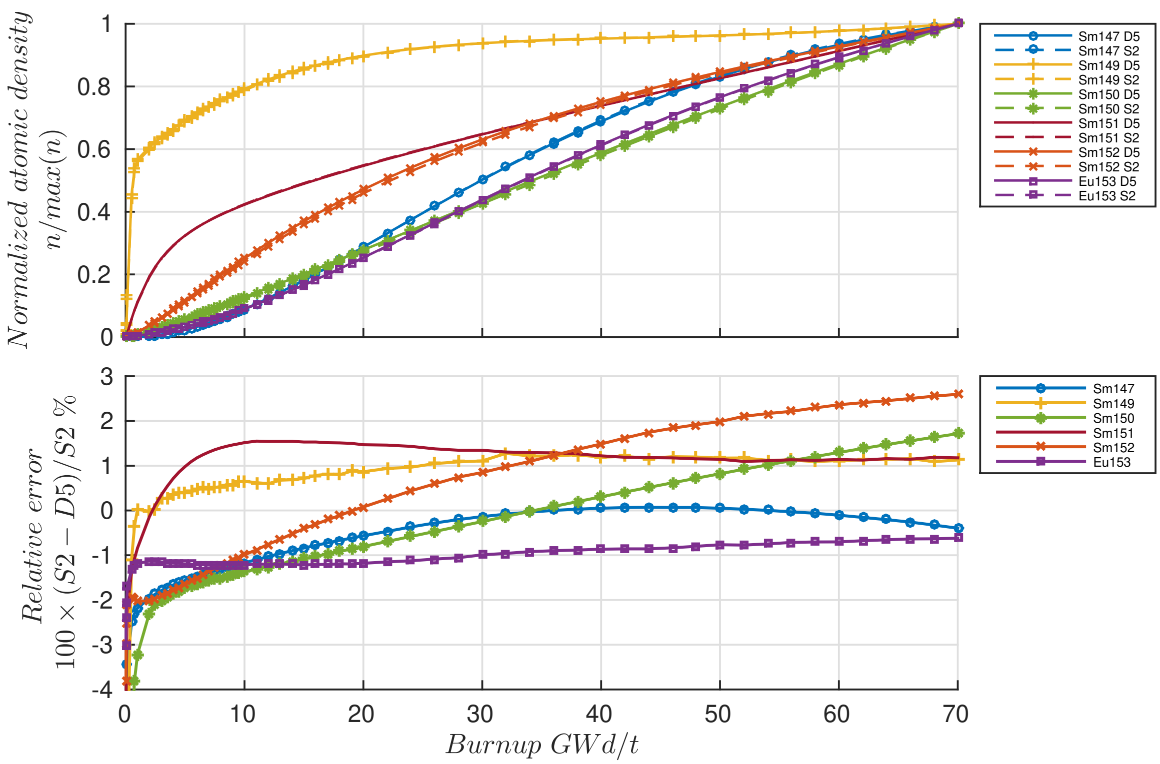

Figure C.7 Pin-wise average density of fission products (PIN-B)

APPENDIX D ASSBLY-B CALCULATION RESULTS

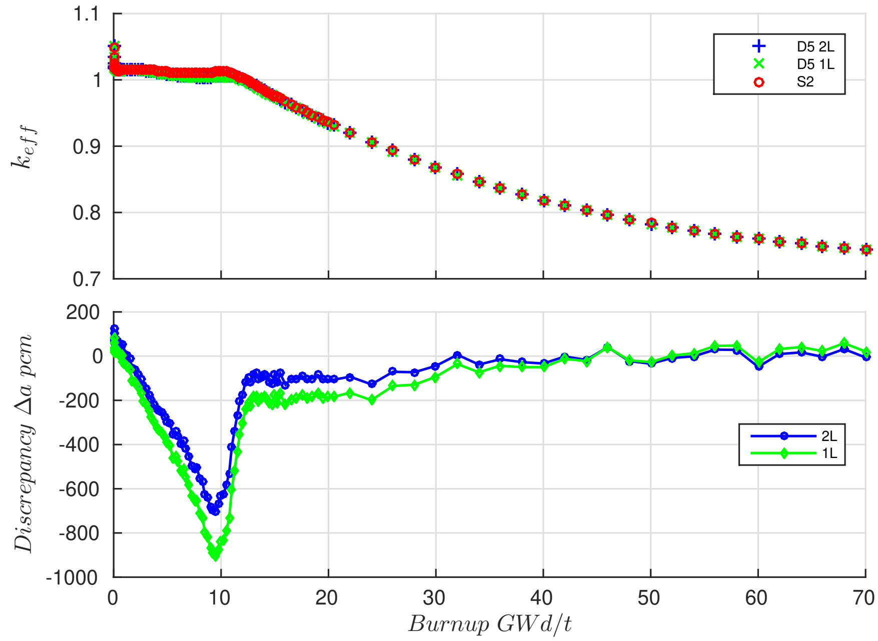

Figure D.1 Evolution of k_{eff} (ASSBLY-B)

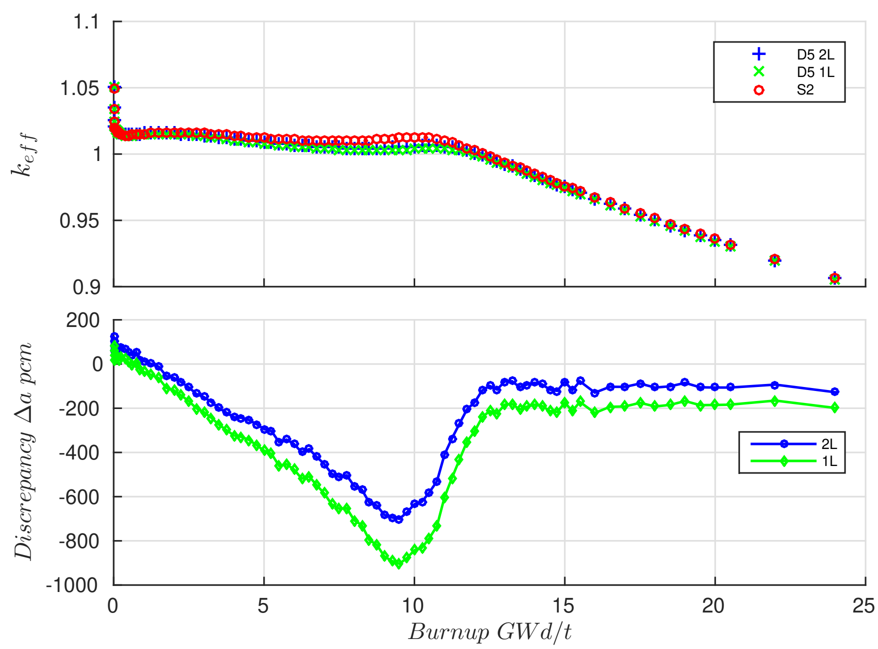

Figure D.2 Evolution of k_{eff} up to $25GWd/t$ (ASSBLY-B)

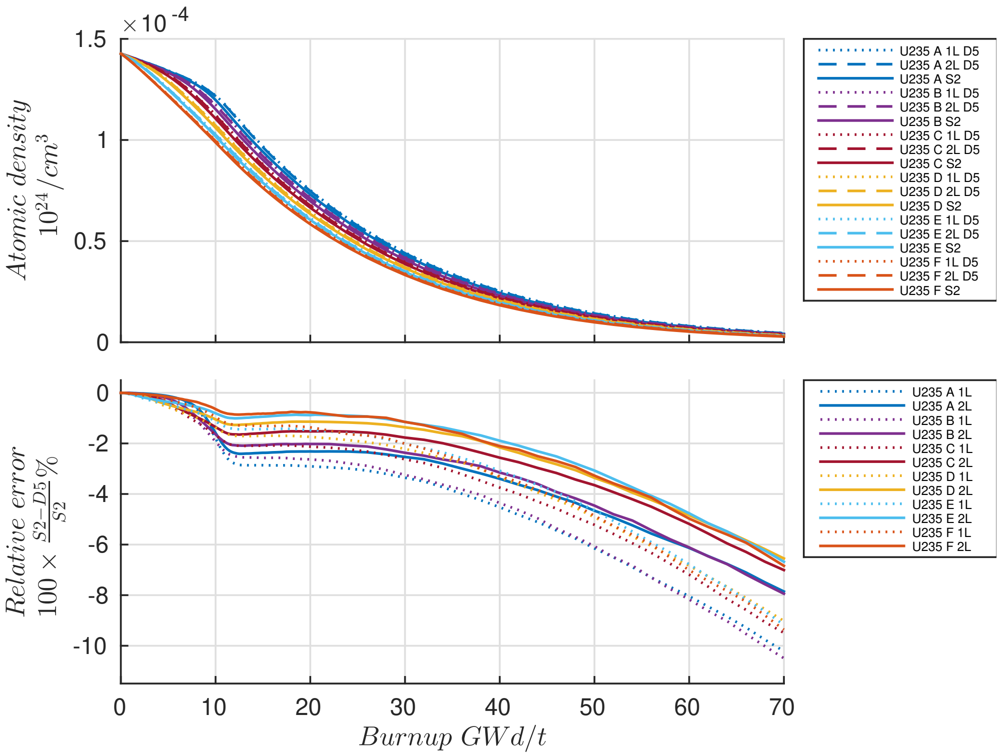

Figure D.3 Atomic density of ^{235}U (ASSBLY-B, C0603)

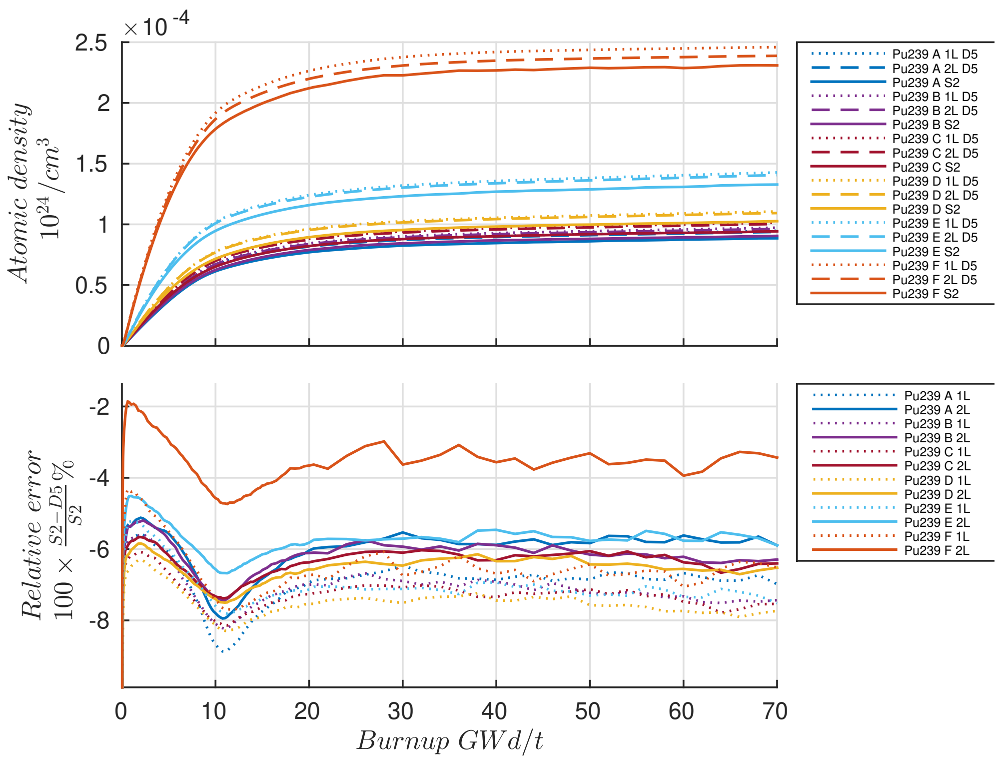

Figure D.4 Atomic density of ^{239}Pu (ASSBLY-B, C0603)

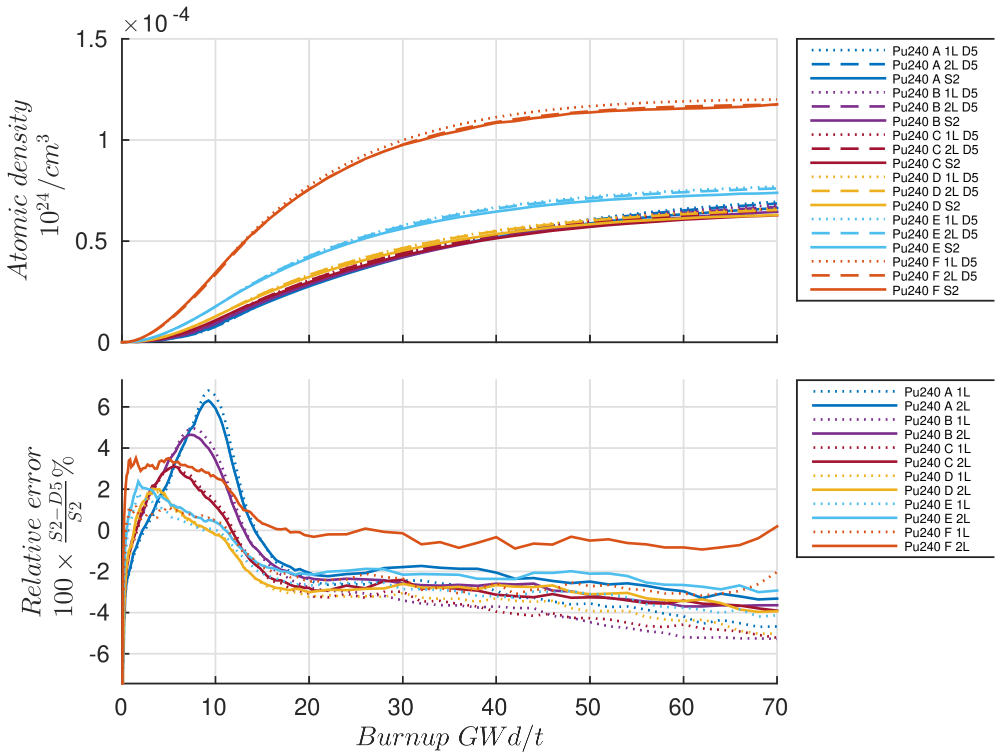

Figure D.5 Atomic density of ^{240}Pu (ASSBLY-B, C0603)

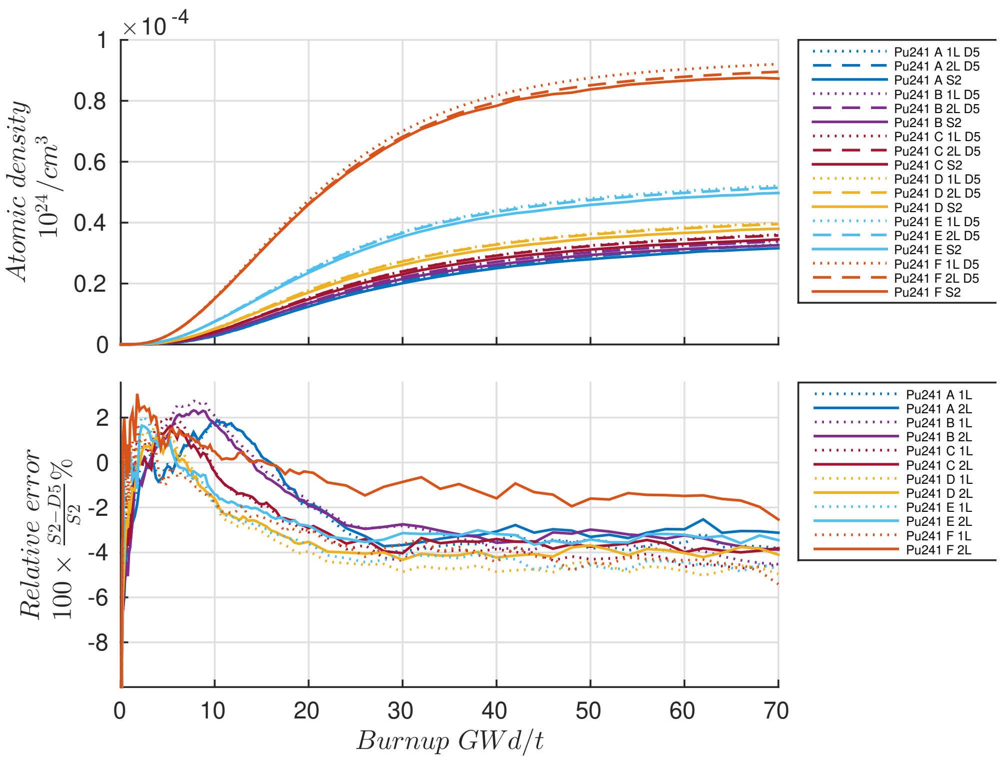

Figure D.6 Atomic density of ^{241}Pu (ASSBLY-B, C0603)

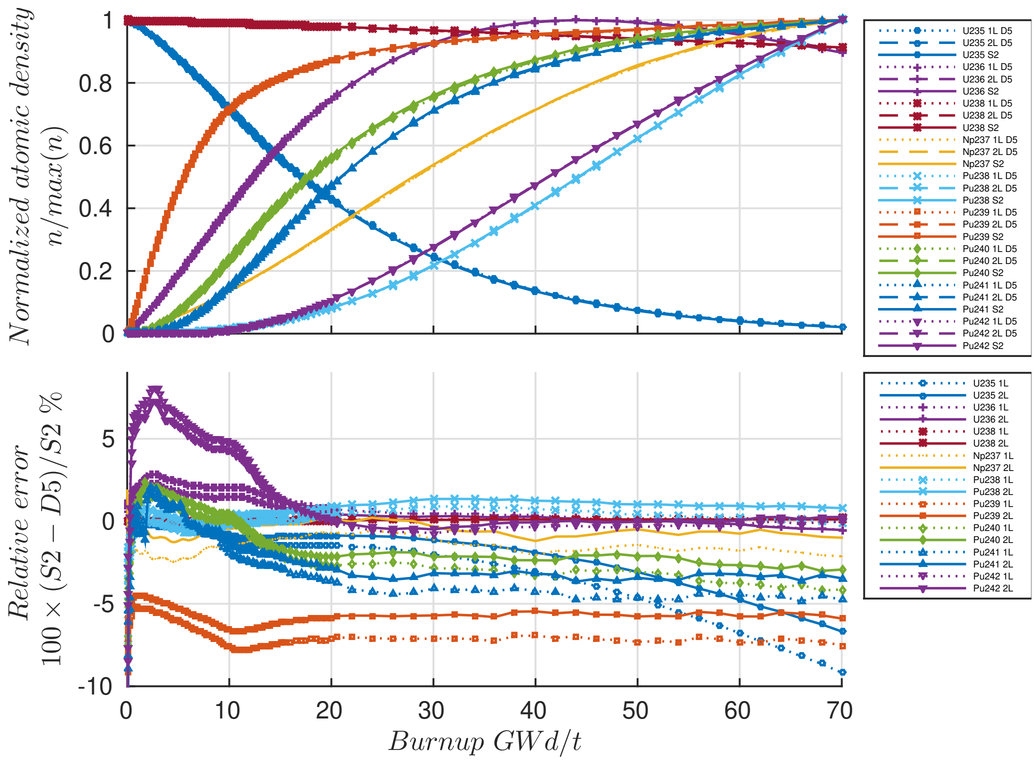

Figure D.7 Pin-wise average density of actinides (ASSBLY-B, C0603)

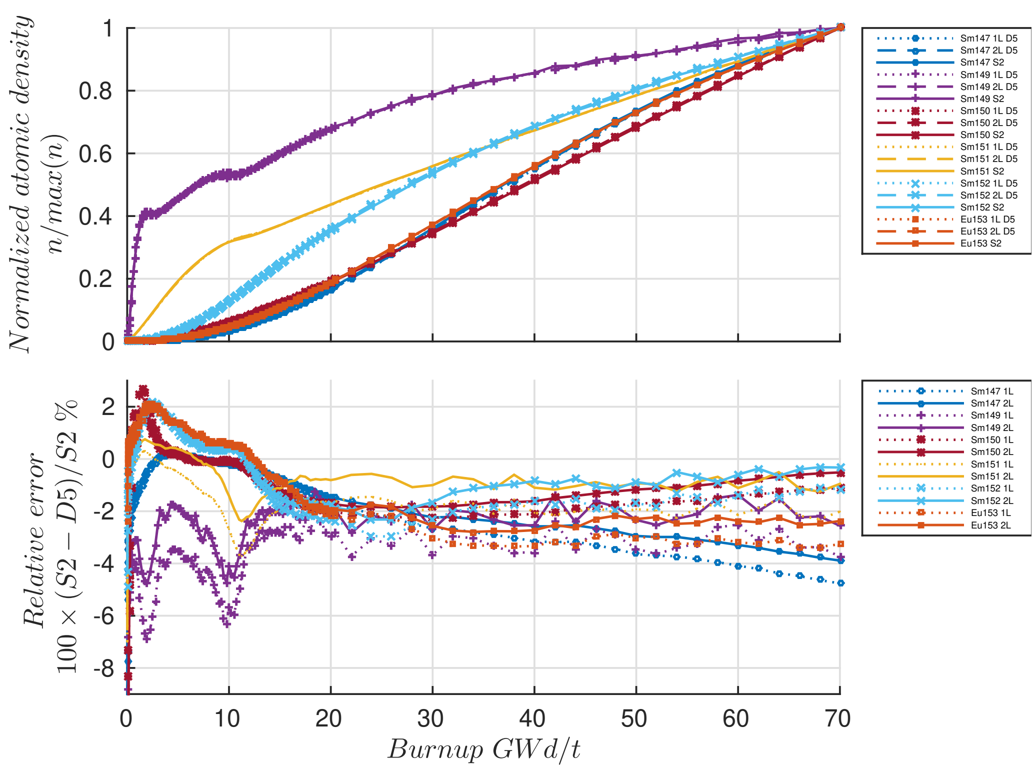

Figure D.8 Pin-wise average density of fission products (ASSBLY-B, C0603)

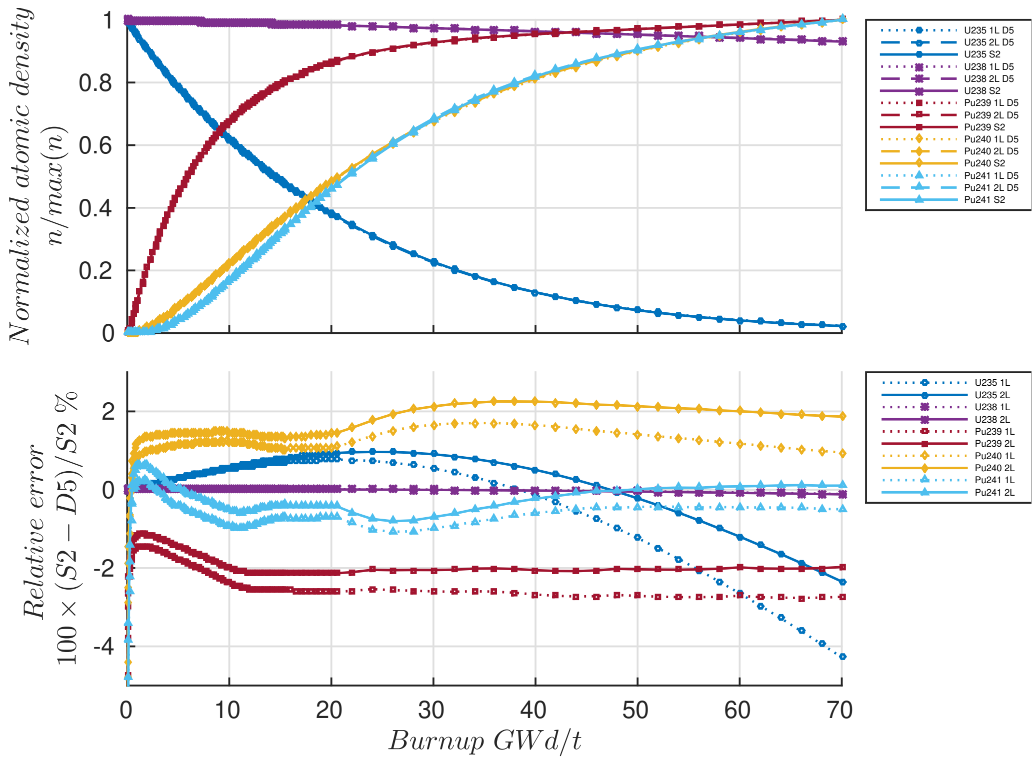

Figure D.9 Assembly-wise average atomic densities (ASSBLY-B)

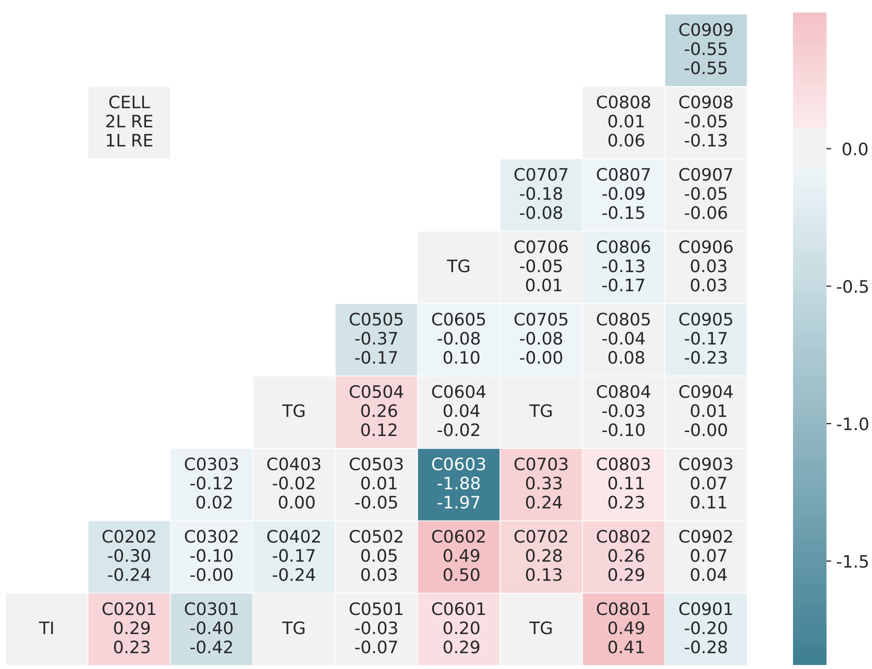

Figure D.10 Relative discrepancies in the fission reaction map at zero burnup (ASSBLY-B)

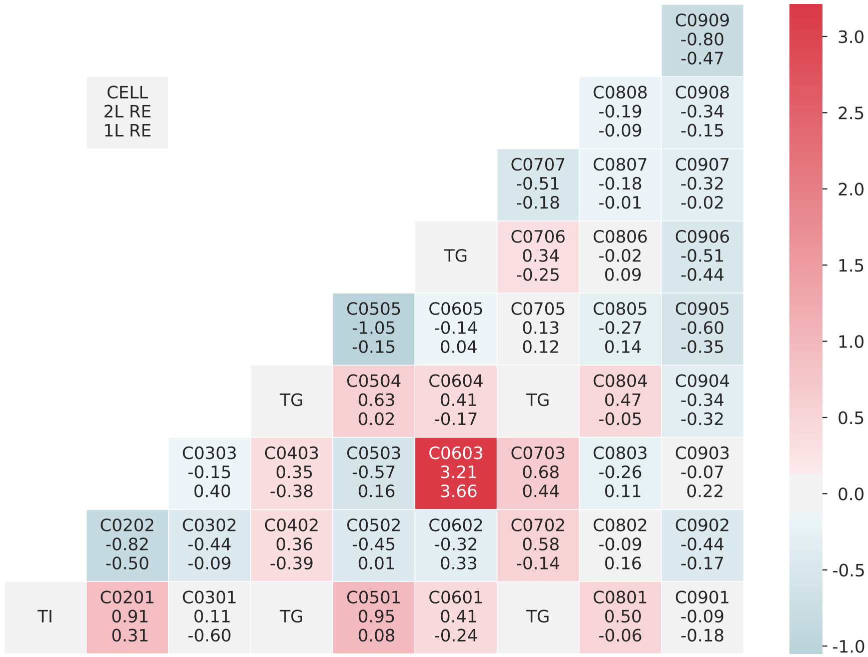

Figure D.11 Relative discrepancies of the capture reaction map at zero burnup (ASSBLY-B)

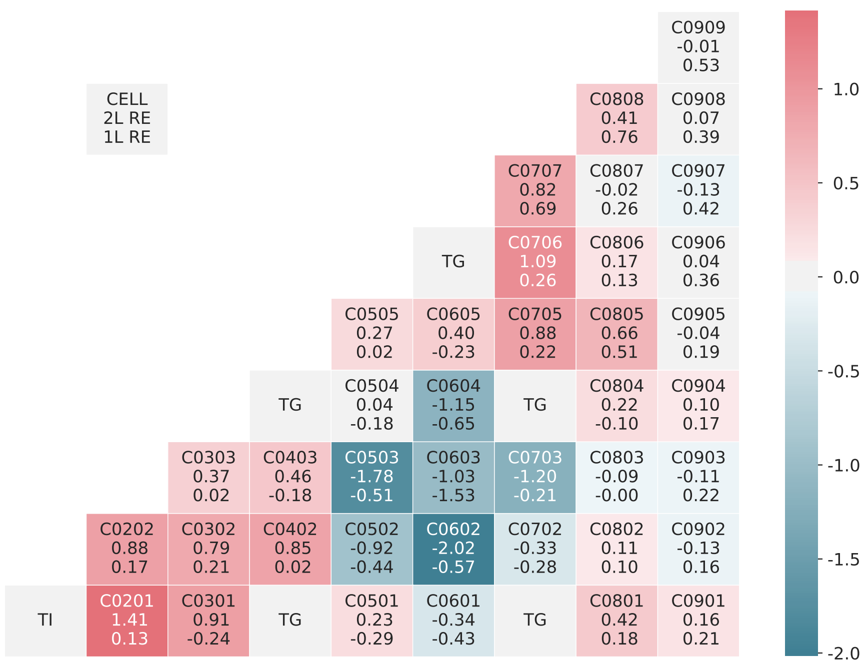

Figure D.12 Relative discrepancies in the fission reaction map at maximum k_{eff} (ASSBLY-B)

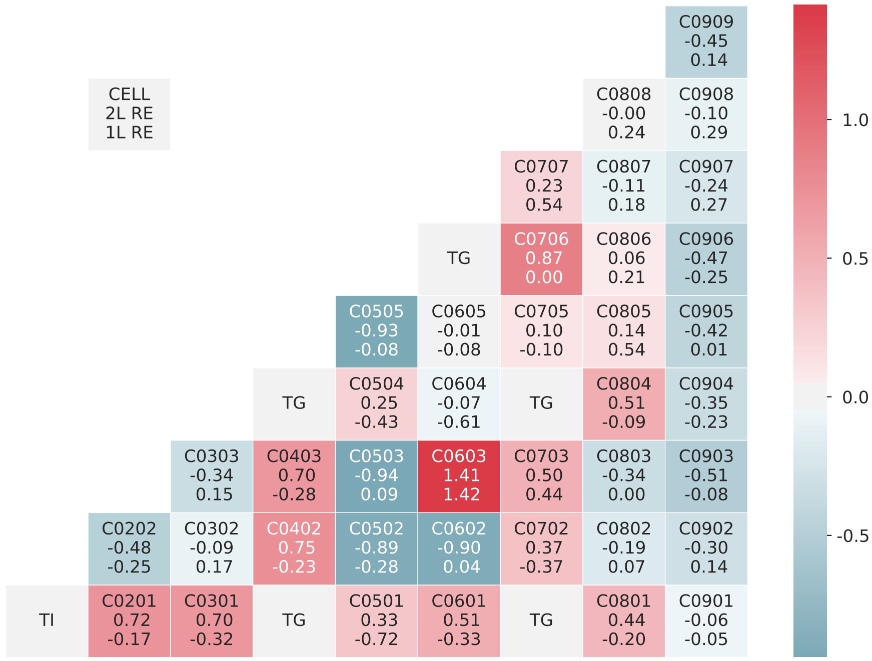

Figure D.13 Relative discrepancies in the capture reaction map at maximum k_{eff} (ASSBLY-B)

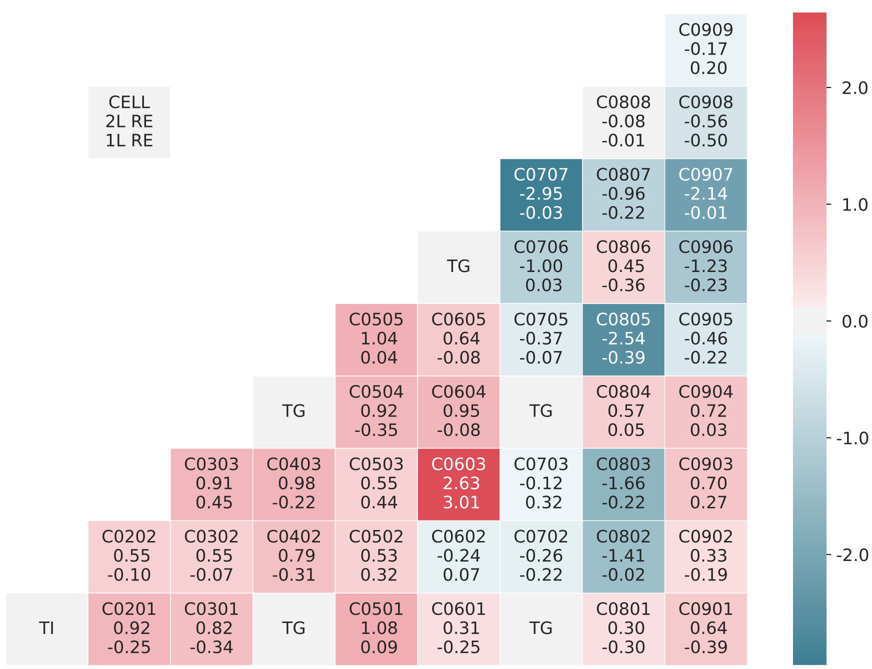

Figure D.14 Relative discrepancies in the fission reaction map at maximum burnup (ASSBLY-B)

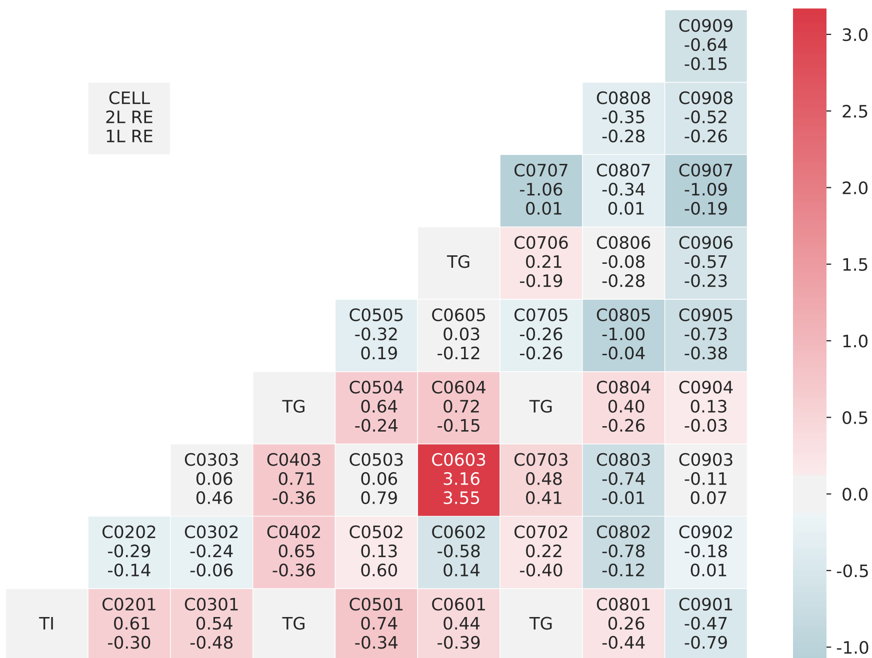

Figure D.15 Relative discrepancies in the capture reaction map at maximum burnup (ASSBLY-B)

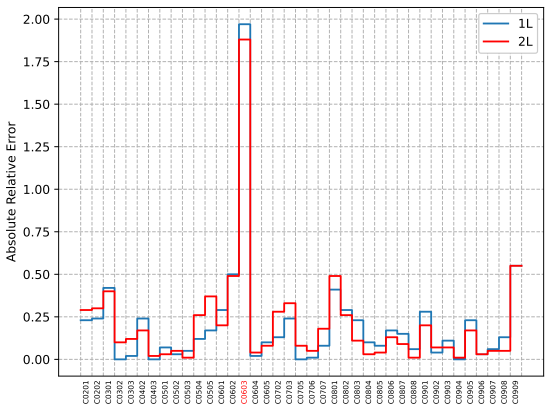

(a) fission rate at zero burnup

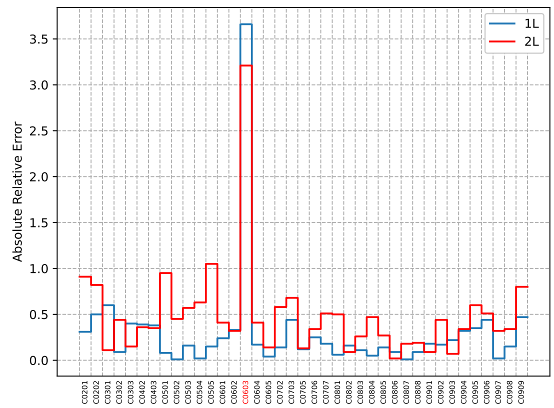

(b) first capture at zero burnup

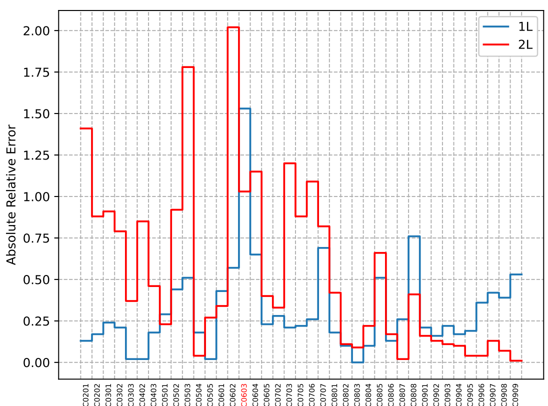

(c) fission rate at maximum k_{eff}

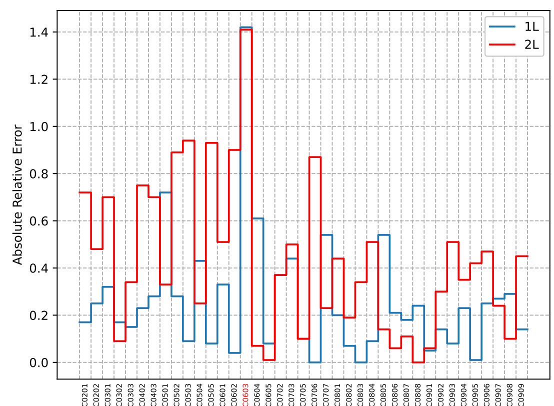

(d) capture rate at maximum k_{eff}

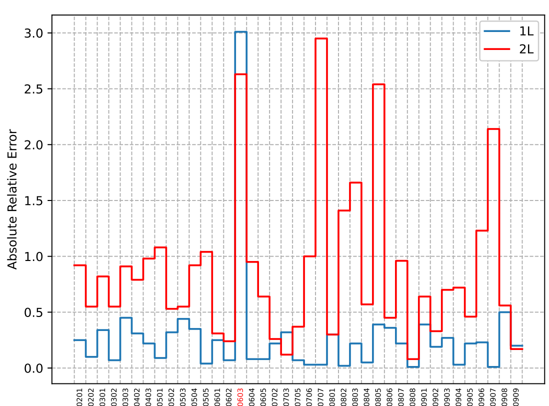

(e) fission rate at maximum burnup

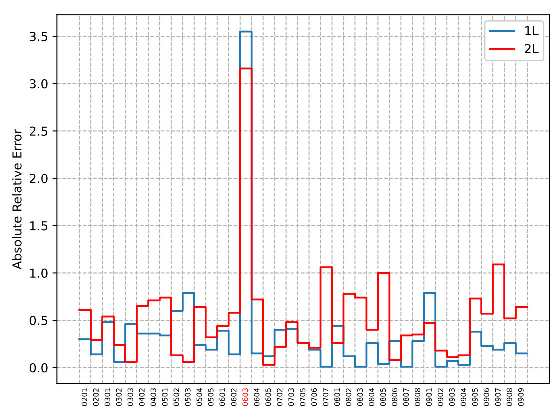

(f) capture rate at maximum burnup

Figure D.16 Absolute relative errors in fission and capture rates (ASSBLY-B)

APPENDIX E ASSBLY-C CALCULATION RESULTS

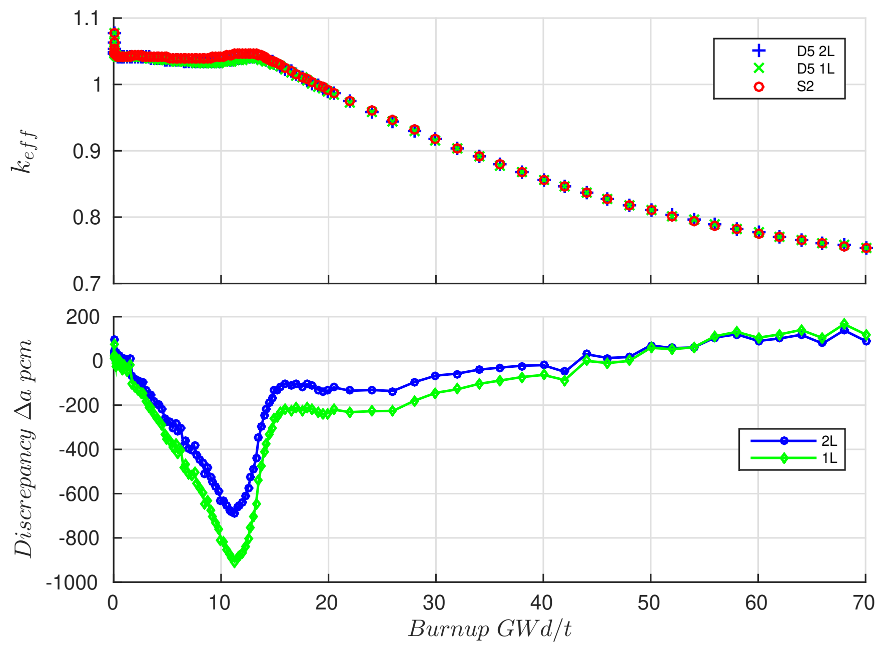

Figure E.1 Evolution of k_{eff} (ASSBLY-C)

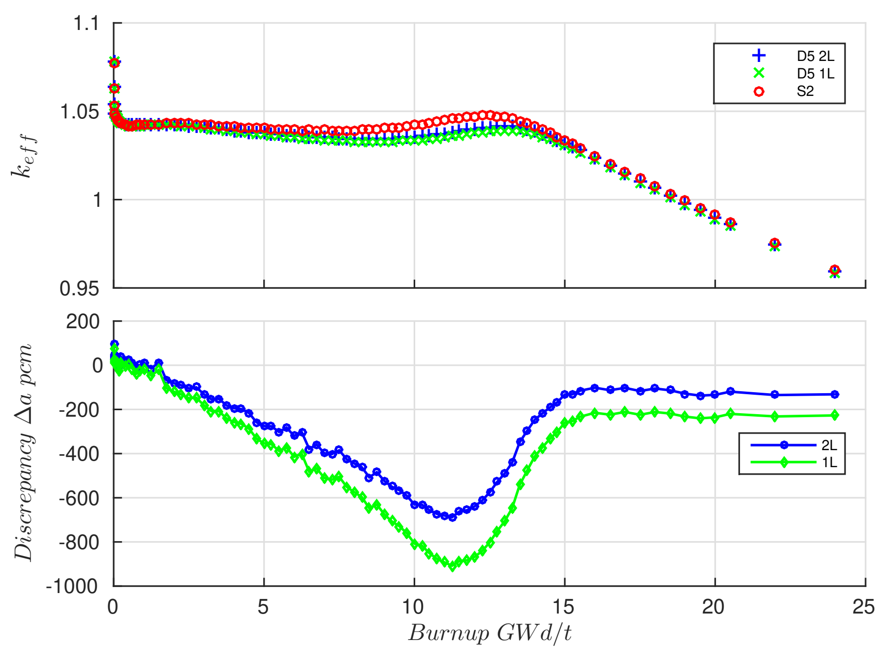

Figure E.2 Evolution of k_{eff} up to $25GWd/t$ (ASSBLY-C)

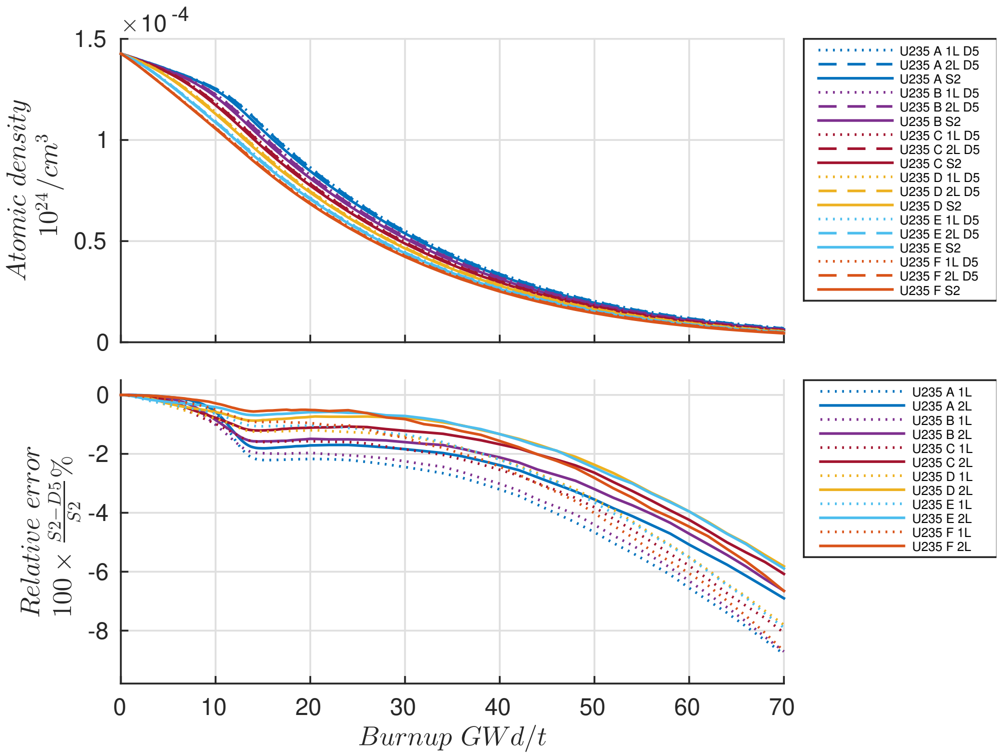

Figure E.3 Atomic density of ^{235}U (ASSBLY-C, C0603)

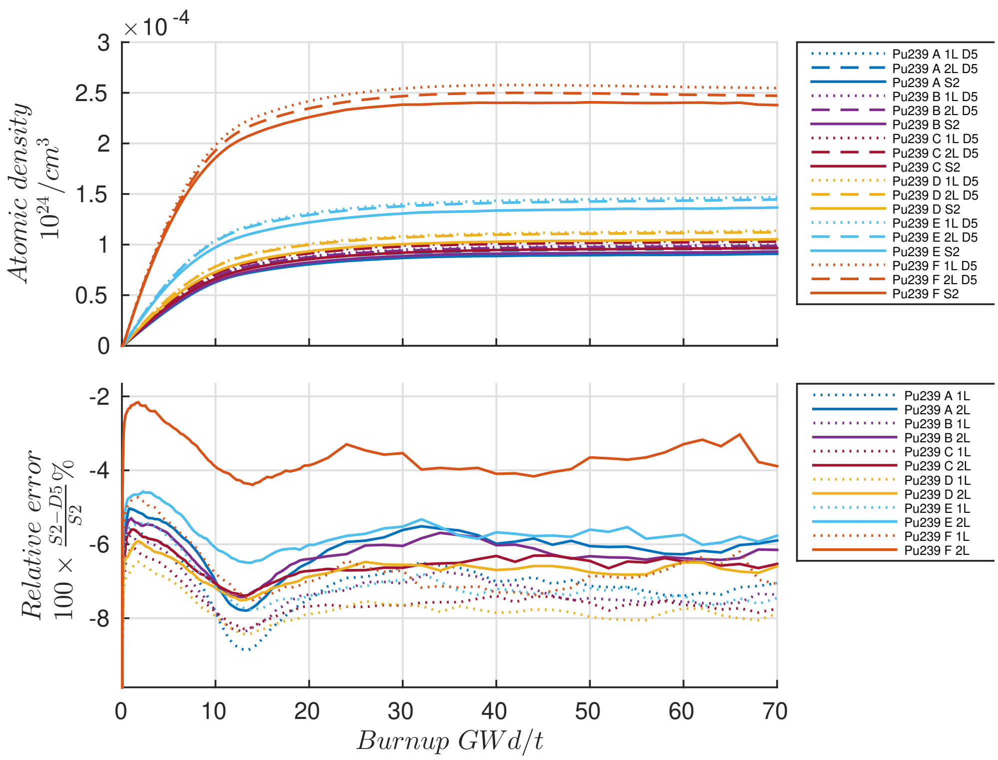

Figure E.4 Atomic density of ^{239}Pu (ASSBLY-C, C0603)

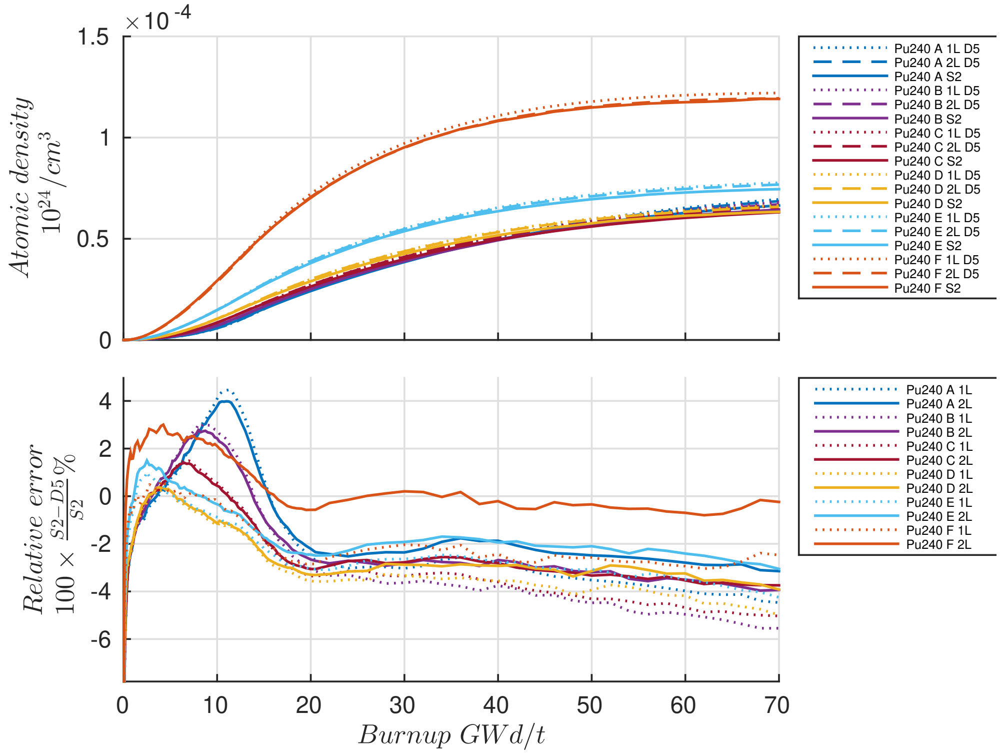

Figure E.5 Atomic density of ^{240}Pu (ASSBLY-C, C0603)

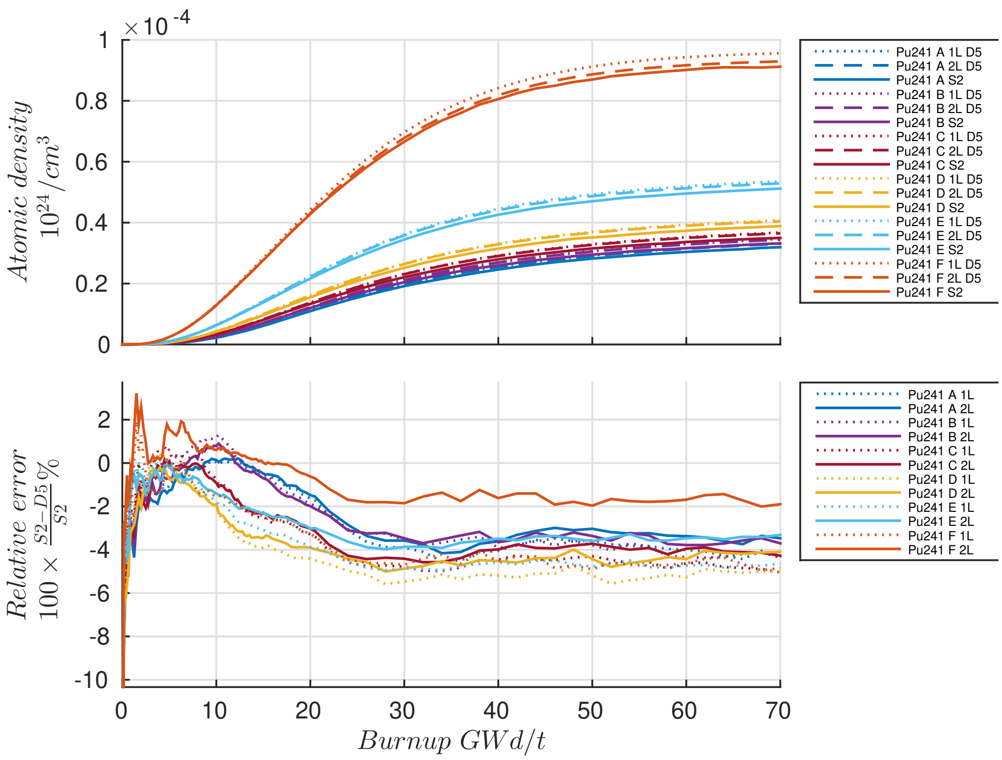

Figure E.6 Atomic density of ^{241}Pu (ASSBLY-C, C0603)

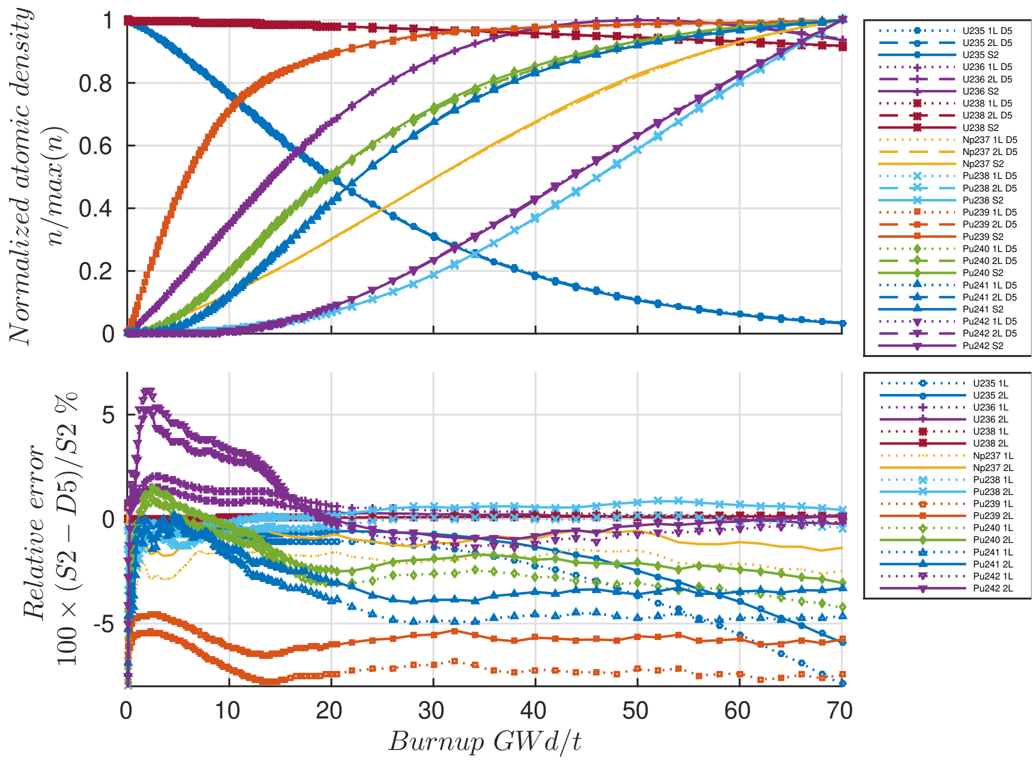

Figure E.7 Pin-wise average density of actinides (ASSBLY-C, C0603)

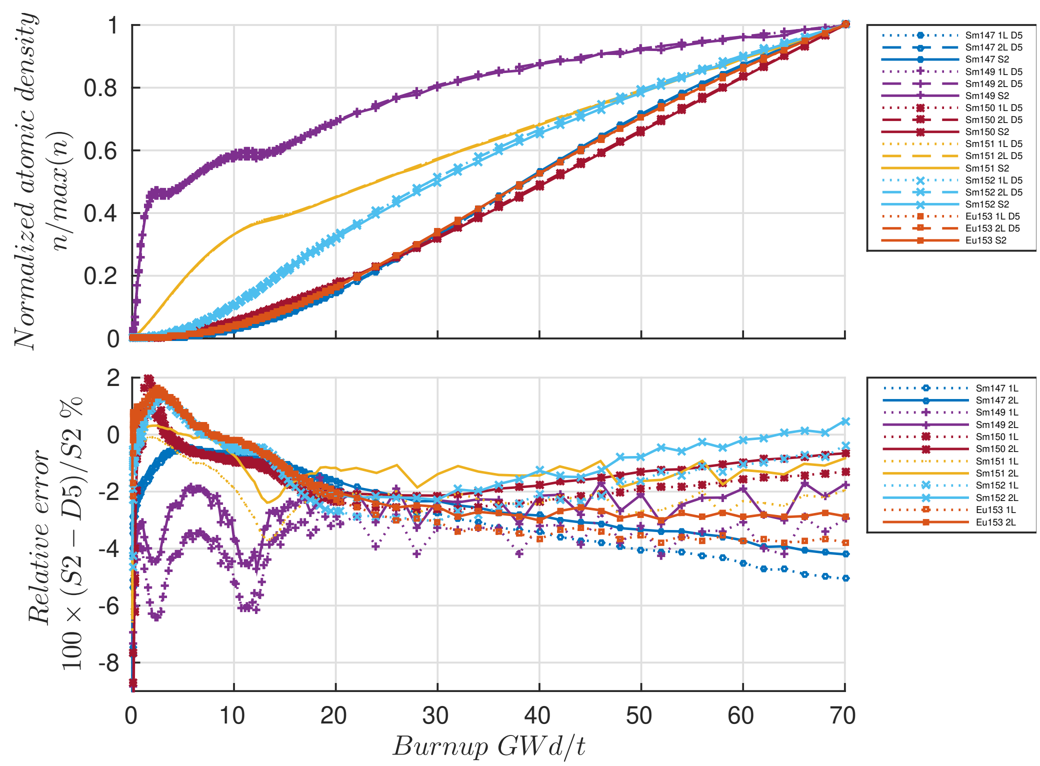

Figure E.8 Pin-wise average density of fission products (ASSBLY-C, C0603)

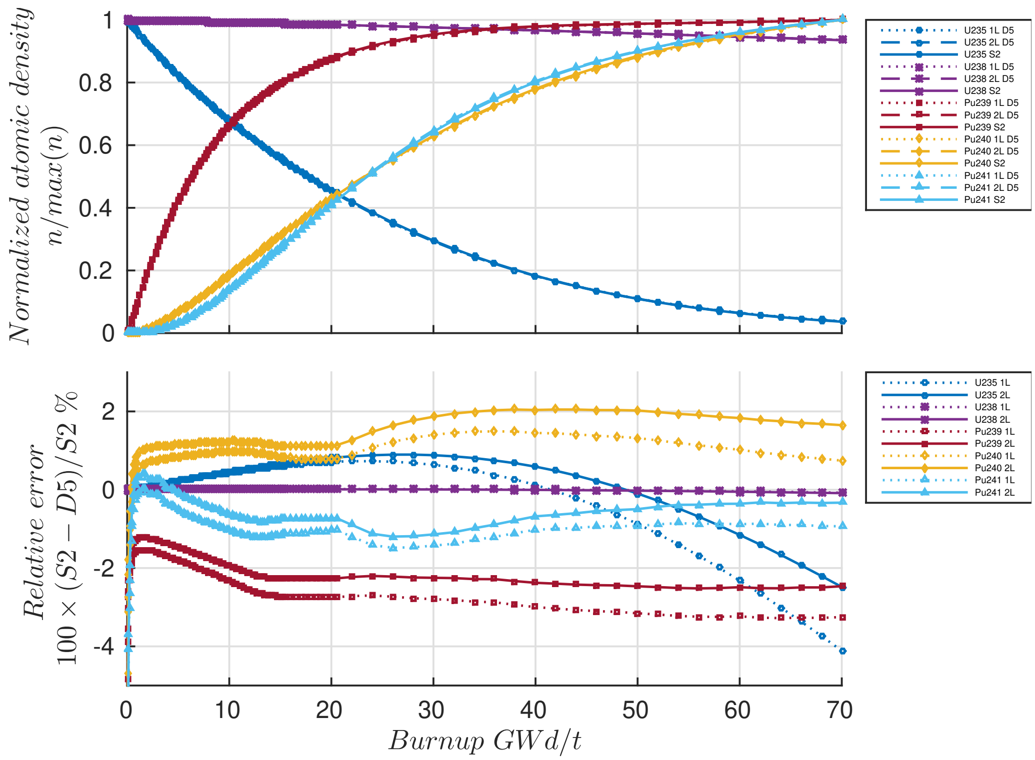

Figure E.9 Assembly-wise average atomic densities (ASSBLY-C)

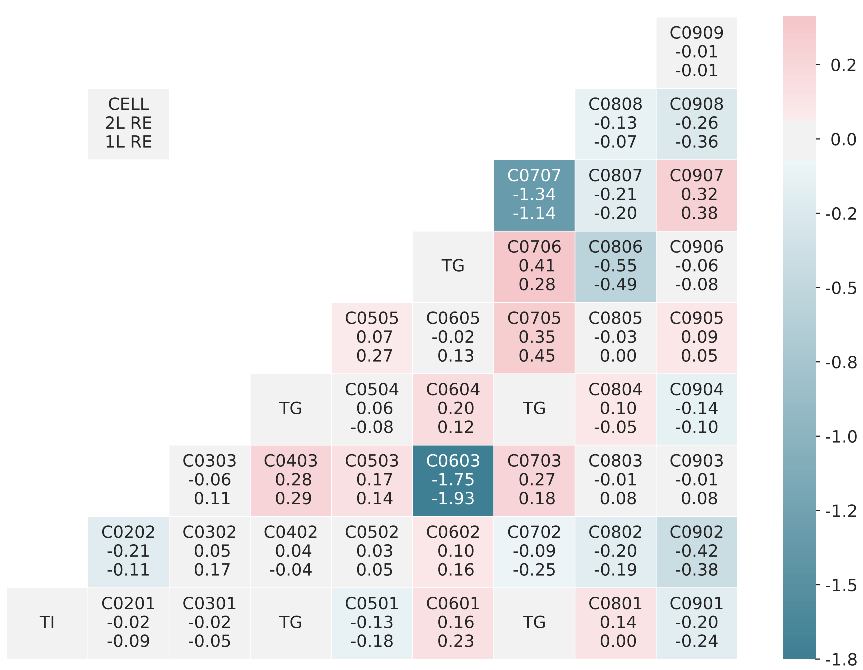

Figure E.10 Relative discrepancies in the fission reaction map at zero burnup (ASSBLY-C)

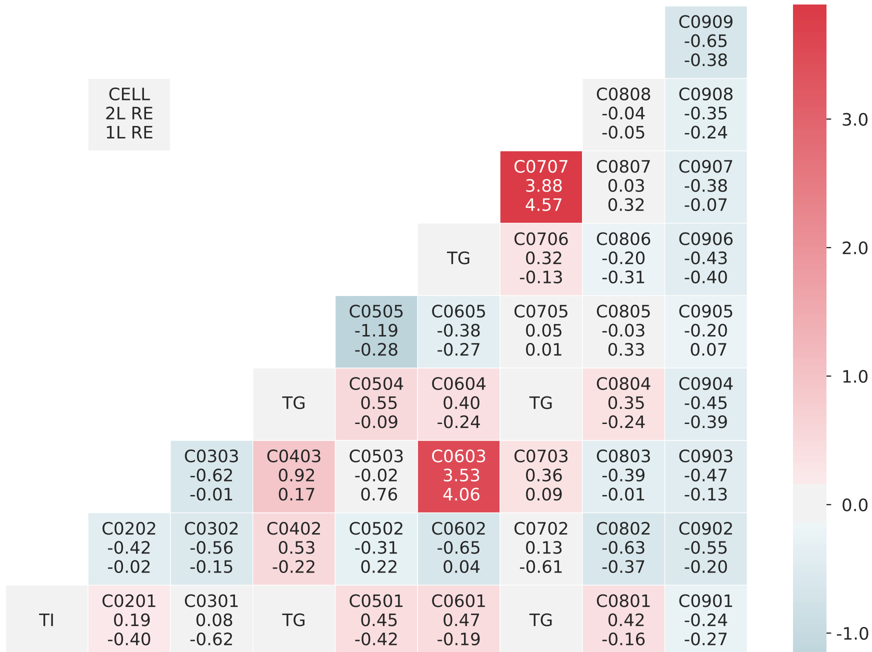

Figure E.11 Relative discrepancies in the capture reaction map at zero burnup (ASSBLY-C)

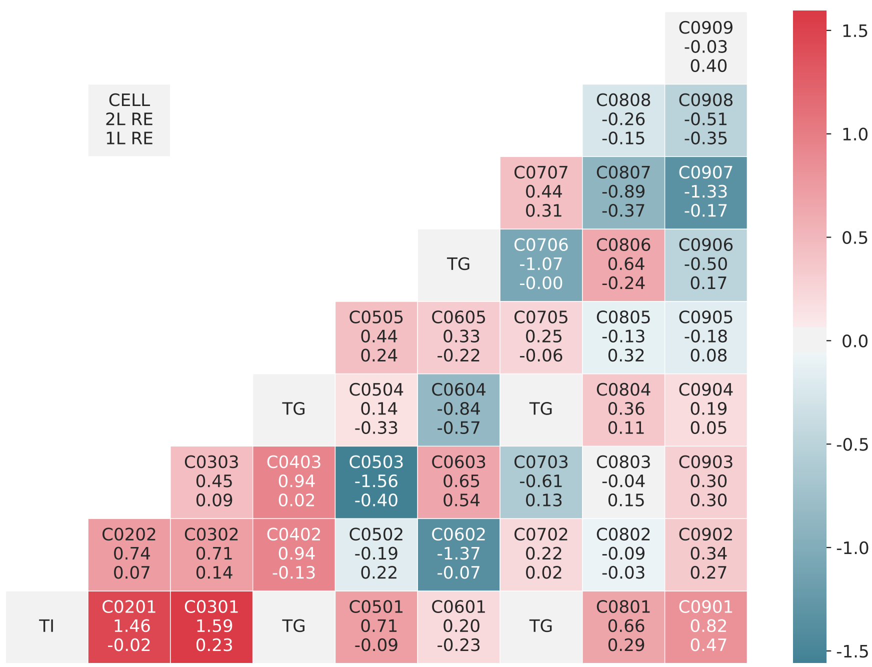

Figure E.12 Relative discrepancies in the fission reaction map at maximum k_{eff} (ASSBLY-C)

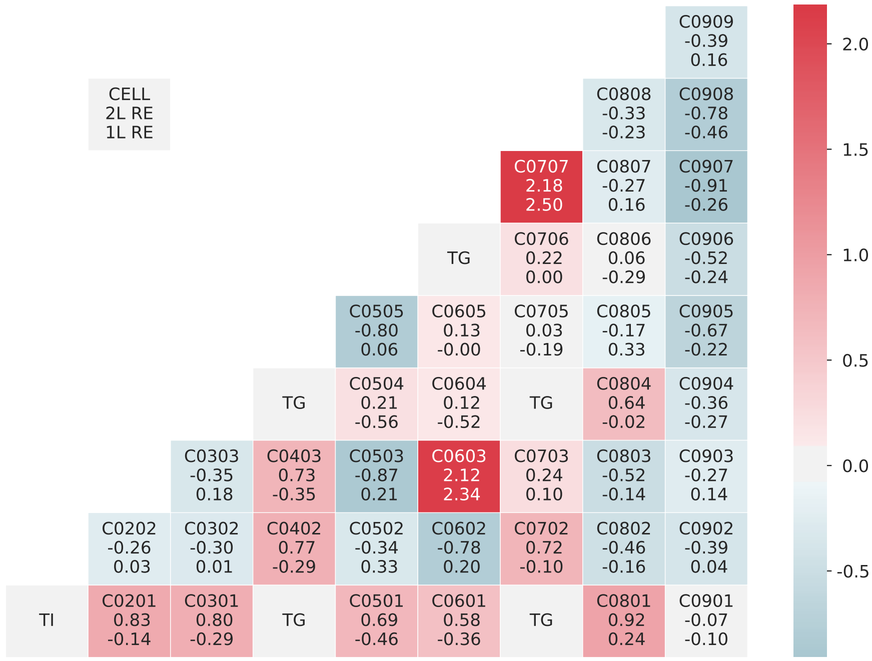

Figure E.13 Relative discrepancies in the capture reaction map at maximum k_{eff} (ASSBLY-C)

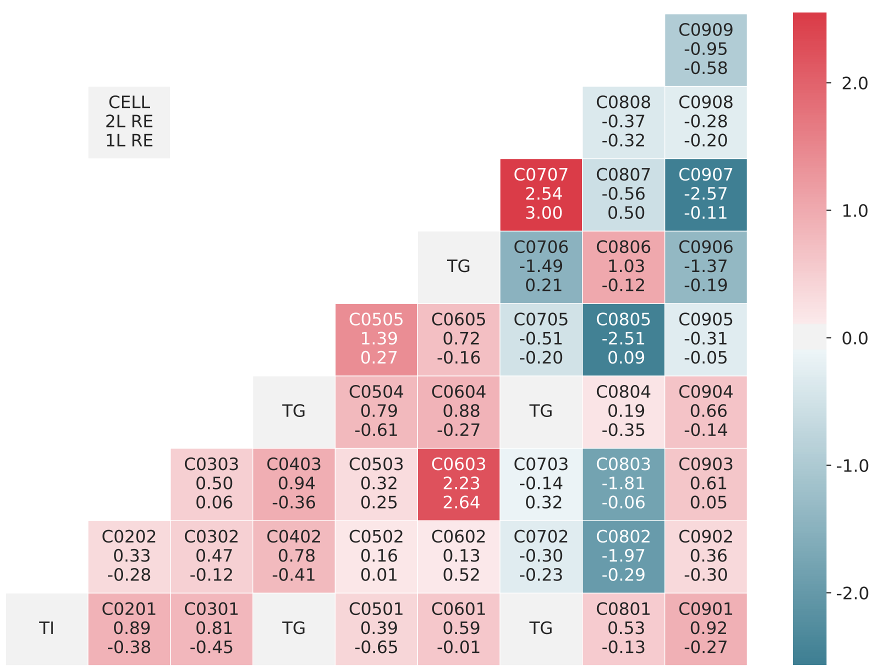

Figure E.14 Relative discrepancies in the fission reaction map at maximum burnup (ASSBLY-C)

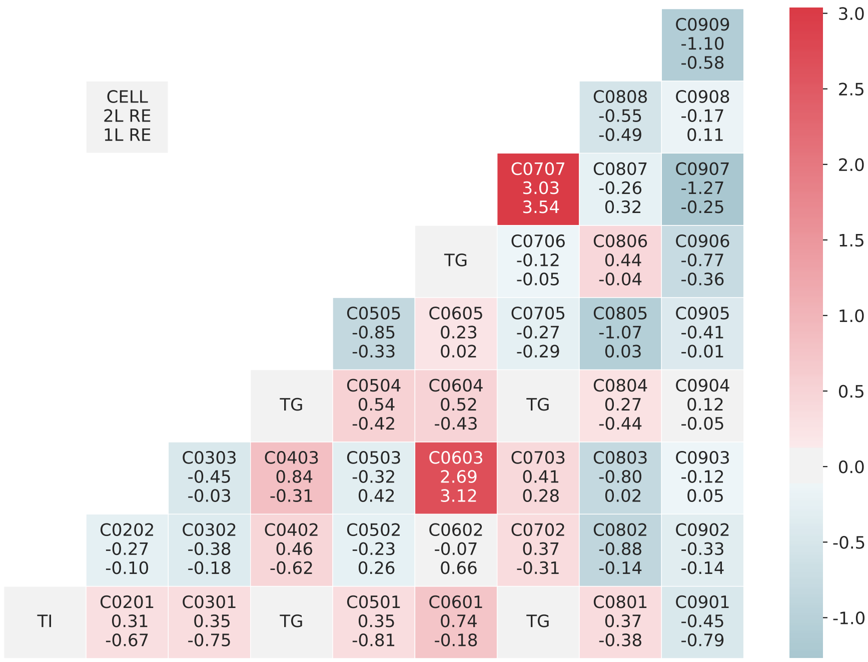

Figure E.15 Relative discrepancies in the capture reaction map at maximum burnup (ASSBLY-C)

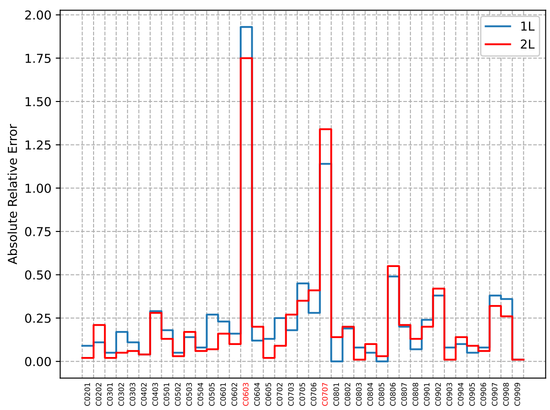

(a) fission rate at zero burnup

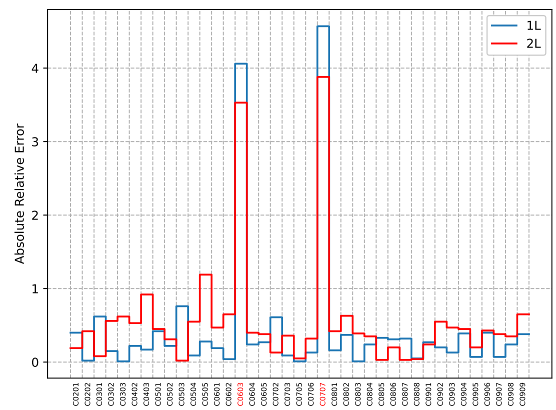

(b) first capture at zero burnup

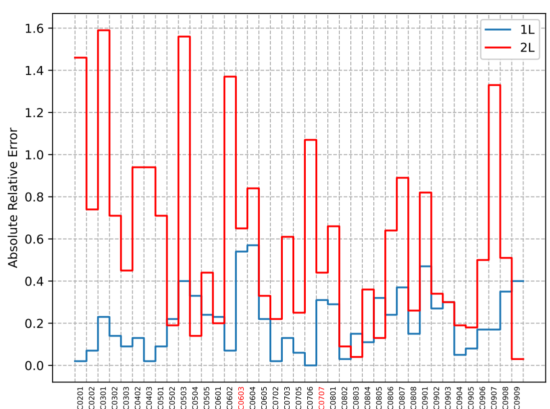

(c) fission rate at maximum k_{eff}

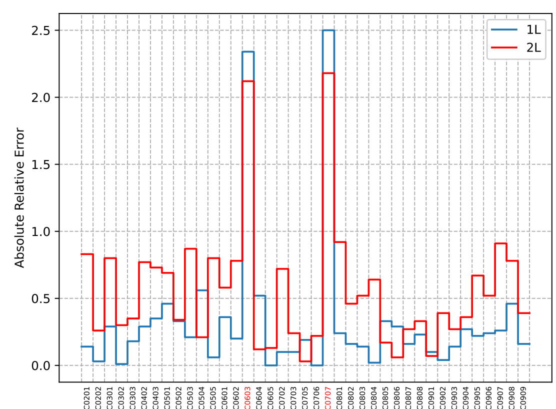

(d) capture rate at maximum k_{eff}

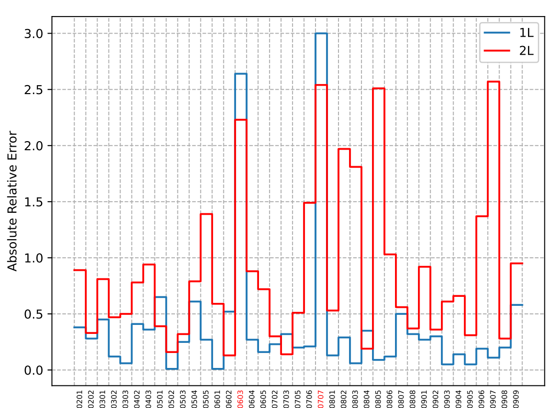

(e) fission rate at maximum burnup

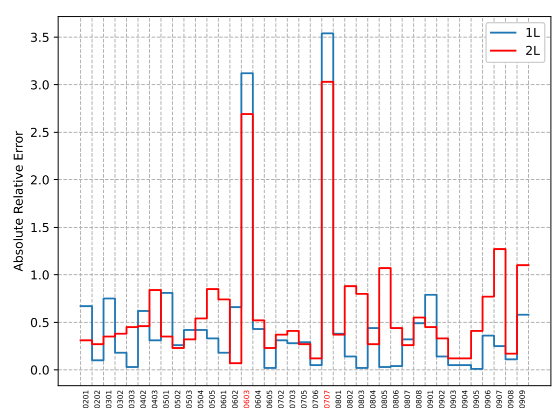

(f) capture rate at maximum burnup

Figure E.16 Absolute relative errors in fission and capture rates (ASSBLY-C)

APPENDIX F FISSION AND CAPTURE RATES

Table F.1 Comparison of fission rates between 1L and 2L schemes (ASSBLY-A)

	Zero BU			**Max BU**		
	R_f^{D5}	R_f^{S2}	Δr	R_f^{D5}	R_f^{S2}	Δr
U235						
$1L\ G1$	3.9728e-02	3.9886e-02	-0.40	8.2015e-04	7.5696e-04	8.35
$2L\ G1$	3.9712e-02	3.9886e-02	-0.44	8.0073e-04	7.5693e-04	5.79
$1L\ G2$	3.4013e-01	3.3940e-01	0.22	3.8857e-03	3.5528e-03	9.37
$2L\ G2$	3.4018e-01	3.3940e-01	0.23	3.8197e-03	3.5527e-03	7.52
U238						
$1L\ G1$	2.6374e-02	2.6950e-02	-2.14	3.8001e-02	3.8164e-02	-0.43
$2L\ G1$	2.6345e-02	2.6950e-02	-2.24	3.8016e-02	3.8163e-02	-0.38
$1L\ G2$	9.1507e-07	9.1544e-07	-0.04	6.4783e-07	6.4948e-07	-0.26
$2L\ G2$	9.1519e-07	9.1545e-07	-0.03	6.5228e-07	6.4946e-07	0.43
Pu239						
$1L\ G1$	-	-	-	1.7398e-02	1.6882e-02	3.06
$2L\ G1$	-	-	-	1.7315e-02	1.6881e-02	2.57
$1L\ G2$	-	-	-	2.0405e-01	2.0407e-01	-0.01
$2L\ G2$	-	-	-	2.0411e-01	2.0406e-01	0.02
Pu241						
$1L\ G1$	-	-	-	1.1299e-02	1.1211e-02	0.78
$2L\ G1$	-	-	-	1.1254e-02	1.1210e-02	0.39
$1L\ G2$	-	-	-	7.2980e-02	7.3799e-02	-1.11
$2L\ G2$	-	-	-	7.3108e-02	7.3797e-02	-0.93

Table F.2 Comparison of capture rates between 1L and 2L schemes (ASSBLY-A)

	Zero BU			**Max BU**		
	R_c^{D5}	R_c^{S2}	Δr	R_c^{D5}	R_c^{S2}	Δr
U235						
$1L\ G1$	1.8893e-02	1.8874e-02	0.11	4.0881e-04	3.7423e-04	9.24
$2L\ G1$	1.8881e-02	1.8835e-02	0.25	3.9911e-04	3.7410e-04	6.69
$1L\ G2$	5.9632e-02	5.9707e-02	-0.12	6.7709e-04	6.1811e-04	9.54
$2L\ G2$	5.9641e-02	5.9585e-02	0.09	6.6560e-04	6.1790e-04	7.72
U238						
$1L\ G1$	2.0144e-01	2.0138e-01	0.03	2.7533e-01	2.7518e-01	0.05
$2L\ G1$	2.0067e-01	2.0097e-01	-0.15	2.7473e-01	2.7509e-01	-0.13
$1L\ G2$	9.3277e-02	9.3285e-02	-0.01	6.6052e-02	6.5908e-02	0.22
$2L\ G2$	9.3289e-02	9.3095e-02	0.21	6.6506e-02	6.5885e-02	0.94
Pu239						
$1L\ G1$	-	-	-	1.0250e-02	9.8409e-03	4.16
$2L\ G1$	-	-	-	1.0200e-02	9.8375e-03	3.69
$1L\ G2$	-	-	-	1.1189e-01	1.1244e-01	-0.48
$2L\ G2$	-	-	-	1.1191e-01	1.1240e-01	-0.44
Pu241						
$1L\ G1$	-	-	-	3.5855e-03	3.5537e-03	0.89
$2L\ G1$	-	-	-	3.5743e-03	3.5525e-03	0.61
$1L\ G2$	-	-	-	2.6664e-02	2.6949e-02	-1.06
$2L\ G2$	-	-	-	2.6709e-02	2.6940e-02	-0.86

Table F.3 Comparison of fission rates between 1L and 2L schemes (ASSBLY-B)

	Zero BU			**BU at $k_{\mathrm{eff-max}}$**			**Max BU**		
	R_f^{D5}	R_f^{S2}	Δr	R_f^{D5}	R_f^{S2}	Δr	R_f^{D5}	R_f^{S2}	Δr
U235									
$1L$ $G1$	5.1926e-02	5.2146e-02	-0.42	3.2262e-02	3.2296e-02	-0.11	1.6436e-03	1.5873e-03	3.55
$2L$ $G1$	5.1887e-02	5.2144e-02	-0.49	3.2184e-02	3.2301e-02	-0.36	1.6152e-03	1.5872e-03	1.76
$1L$ $G2$	3.2727e-01	3.2647e-01	0.25	1.7154e-01	1.7144e-01	0.06	7.6612e-03	7.3093e-03	4.81
$2L$ $G2$	3.2720e-01	3.2645e-01	0.23	1.7199e-01	1.7147e-01	0.30	7.5951e-03	7.3091e-03	3.91
U238									
$1L$ $G1$	2.6898e-02	2.7483e-02	-2.13	2.8536e-02	2.8783e-02	-0.86	3.7765e-02	3.7825e-02	-0.16
$2L$ $G1$	2.6995e-02	2.7482e-02	-1.77	2.8574e-02	2.8787e-02	-0.74	3.7886e-02	3.7824e-02	0.17
$1L$ $G2$	6.6042e-07	6.6051e-07	-0.01	5.7780e-07	5.7662e-07	0.21	6.3119e-07	6.2964e-07	0.25
$2L$ $G2$	6.6022e-07	6.6049e-07	-0.04	5.7959e-07	5.7671e-07	0.50	6.3644e-07	6.2962e-07	1.08
Pu239									
$1L$ $G1$	-	-	-	9.3133e-03	9.0250e-03	3.20	1.7438e-02	1.6968e-02	2.77
$2L$ $G1$	-	-	-	9.2652e-03	9.0263e-03	2.65	1.7329e-02	1.6967e-02	2.13
$1L$ $G2$	-	-	-	1.2487e-01	1.2493e-01	-0.04	2.0175e-01	2.0172e-01	0.01
$2L$ $G2$	-	-	-	1.2460e-01	1.2495e-01	-0.28	2.0175e-01	2.0171e-01	0.02
Pu241									
$1L$ $G1$	-	-	-	1.5951e-03	1.5707e-03	1.55	1.1251e-02	1.1214e-02	0.33
$2L$ $G1$	-	-	-	1.5856e-03	1.5709e-03	0.93	1.1188e-02	1.1214e-02	-0.23
$1L$ $G2$	-	-	-	1.1607e-02	1.1681e-02	-0.64	7.1643e-02	7.2529e-02	-1.22
$2L$ $G2$	-	-	-	1.1586e-02	1.1683e-02	-0.83	7.1780e-02	7.2527e-02	-1.03

Table F.4 Comparison of capture rates between 1L and 2L schemes (ASSBLY-B)

	Zero BU			**BU at $k_{\mathrm{eff-max}}$**			**Max BU**		
	R_c^{D5}	R_c^{S2}	Δr	R_c^{D5}	R_c^{S2}	Δr	R_c^{D5}	R_c^{S2}	Δr
U235									
$1L\ G1$	2.4625e-02	2.4640e-02	-0.06	1.5635e-02	1.5651e-02	-0.10	8.1879e-04	7.8719e-04	4.01
$2L\ G1$	2.4585e-02	2.4577e-02	0.03	1.5585e-02	1.5603e-02	-0.12	8.0404e-04	7.8647e-04	2.23
$1L\ G2$	5.7551e-02	5.7694e-02	-0.25	3.0005e-02	3.0224e-02	-0.72	1.3352e-03	1.2765e-03	4.59
$2L\ G2$	5.7535e-02	5.7547e-02	-0.02	3.0079e-02	3.0132e-02	-0.18	1.3234e-03	1.2754e-03	3.77
U238									
$1L\ G1$	2.0329e-01	2.0304e-01	0.13	2.1157e-01	2.1036e-01	0.57	2.7414e-01	2.7346e-01	0.25
$2L\ G1$	2.0247e-01	2.0252e-01	-0.02	2.1038e-01	2.0972e-01	0.31	2.7327e-01	2.7321e-01	0.02
$1L\ G2$	6.7366e-02	6.7465e-02	-0.15	5.8932e-02	5.9085e-02	-0.26	6.4359e-02	6.4138e-02	0.35
$2L\ G2$	6.7347e-02	6.7294e-02	0.08	5.9113e-02	5.8904e-02	0.35	6.4894e-02	6.4079e-02	1.27
Pu239									
$1L\ G1$	-	-	-	5.4876e-03	5.3087e-03	3.37	1.0273e-02	9.9441e-03	3.31
$2L\ G1$	-	-	-	5.4562e-03	5.2925e-03	3.09	1.0201e-02	9.9351e-03	2.68
$1L\ G2$	-	-	-	6.9343e-02	7.0281e-02	-1.34	1.1072e-01	1.1163e-01	-0.82
$2L\ G2$	-	-	-	6.9163e-02	7.0067e-02	-1.29	1.1068e-01	1.1153e-01	-0.76
Pu241									
$1L\ G1$	-	-	-	5.0778e-04	5.0404e-04	0.74	3.5700e-03	3.5714e-03	-0.04
$2L\ G1$	-	-	-	5.0527e-04	5.0251e-04	0.55	3.5521e-03	3.5682e-03	-0.45
$1L\ G2$	-	-	-	4.2679e-03	4.3323e-03	-1.49	2.6188e-02	2.6596e-02	-1.54
$2L\ G2$	-	-	-	4.2594e-03	4.3191e-03	-1.38	2.6235e-02	2.6572e-02	-1.27

Table F.5 Comparison of fission rates between 1L and 2L schemes (ASSBLY-C)

	Zero BU			**BU at $k_{\text{eff}-\max}$**			**Max BU**		
	R_f^{D5}	R_f^{S2}	Δr	R_f^{D5}	R_f^{S2}	Δr	R_f^{D5}	R_f^{S2}	Δr
U235									
$1L\ G1$	6.2792e-02	6.3053e-02	-0.41	3.8754e-02	3.8833e-02	-0.20	3.3236e-03	3.2208e-03	3.19
$2L\ G1$	6.2744e-02	6.3050e-02	-0.49	3.8650e-02	3.8839e-02	-0.49	3.2757e-03	3.2206e-03	1.71
$1L\ G2$	3.1741e-01	3.1657e-01	0.27	1.7617e-01	1.7628e-01	-0.06	1.4908e-02	1.4346e-02	3.91
$2L\ G2$	3.1735e-01	3.1656e-01	0.25	1.7666e-01	1.7631e-01	0.20	1.4828e-02	1.4345e-02	3.36
U238									
$1L\ G1$	2.5981e-02	2.6566e-02	-2.20	2.7299e-02	2.7514e-02	-0.78	3.7067e-02	3.7157e-02	-0.24
$2L\ G1$	2.6080e-02	2.6565e-02	-1.82	2.7331e-02	2.7518e-02	-0.68	3.7186e-02	3.7156e-02	0.08
$1L\ G2$	4.9514e-07	4.9514e-07	0.00	4.6473e-07	4.6447e-07	0.06	5.9456e-07	5.9727e-07	-0.45
$2L\ G2$	4.9501e-07	4.9512e-07	-0.02	4.6626e-07	4.6454e-07	0.37	5.9971e-07	5.9724e-07	0.41
Pu239									
$1L\ G1$	-	-	-	9.8782e-03	9.5623e-03	3.30	1.7613e-02	1.7073e-02	3.16
$2L\ G1$	-	-	-	9.8213e-03	9.5638e-03	2.69	1.7498e-02	1.7072e-02	2.49
$1L\ G2$	-	-	-	1.1586e-01	1.1575e-01	0.10	1.9710e-01	1.9728e-01	-0.09
$2L\ G2$	-	-	-	1.1558e-01	1.1576e-01	-0.16	1.9712e-01	1.9727e-01	-0.08
Pu241									
$1L\ G1$	-	-	-	1.8351e-03	1.8047e-03	1.68	1.1262e-02	1.1186e-02	0.67
$2L\ G1$	-	-	-	1.8238e-03	1.8050e-03	1.04	1.1199e-02	1.1186e-02	0.12
$1L\ G2$	-	-	-	1.1534e-02	1.1592e-02	-0.50	6.9248e-02	7.0259e-02	-1.44
$2L\ G2$	-	-	-	1.1515e-02	1.1594e-02	-0.68	6.9405e-02	7.0256e-02	-1.21

Table F.6 Comparison of capture rates between 1L and 2L schemes (ASSBLY-C)

	Zero BU			**BU at $k_{\mathrm{eff-max}}$**			**Max BU**		
	R_c^{D5}	R_c^{S2}	Δr	R_c^{D5}	R_c^{S2}	Δr	R_c^{D5}	R_c^{S2}	Δr
U235									
$1L$ $G1$	2.9682e-02	2.9695e-02	-0.04	1.8754e-02	1.8807e-02	-0.28	1.6547e-03	1.5945e-03	3.77
$2L$ $G1$	2.9632e-02	2.9622e-02	0.03	1.8687e-02	1.8745e-02	-0.31	1.6296e-03	1.5931e-03	2.29
$1L$ $G2$	5.5958e-02	5.6090e-02	-0.23	3.0844e-02	3.1126e-02	-0.90	2.5984e-03	2.5026e-03	3.83
$2L$ $G2$	5.5943e-02	5.5951e-02	-0.01	3.0927e-02	3.1024e-02	-0.31	2.5841e-03	2.5003e-03	3.35
U238									
$1L$ $G1$	1.9435e-01	1.9413e-01	0.11	2.0113e-01	1.9992e-01	0.61	2.6921e-01	2.6838e-01	0.31
$2L$ $G1$	1.9361e-01	1.9365e-01	-0.02	1.9997e-01	1.9926e-01	0.35	2.6836e-01	2.6813e-01	0.08
$1L$ $G2$	5.0539e-02	5.0611e-02	-0.14	4.7418e-02	4.7641e-02	-0.47	6.0629e-02	6.0769e-02	-0.23
$2L$ $G2$	5.0525e-02	5.0486e-02	0.08	4.7573e-02	4.7485e-02	0.19	6.1153e-02	6.0713e-02	0.72
Pu239									
$1L$ $G1$	-	-	-	5.8156e-03	5.6240e-03	3.41	1.0373e-02	9.9825e-03	3.91
$2L$ $G1$	-	-	-	5.7786e-03	5.6056e-03	3.09	1.0298e-02	9.9734e-03	3.25
$1L$ $G2$	-	-	-	6.4738e-02	6.5529e-02	-1.21	1.0833e-01	1.0917e-01	-0.77
$2L$ $G2$	-	-	-	6.4555e-02	6.5315e-02	-1.16	1.0830e-01	1.0907e-01	-0.71
Pu241									
$1L$ $G1$	-	-	-	5.8376e-04	5.7953e-04	0.73	3.5720e-03	3.5559e-03	0.46
$2L$ $G1$	-	-	-	5.8076e-04	5.7763e-04	0.54	3.5543e-03	3.5526e-03	0.05
$1L$ $G2$	-	-	-	4.2581e-03	4.3185e-03	-1.40	2.5334e-02	2.5751e-02	-1.62
$2L$ $G2$	-	-	-	4.2502e-03	4.3044e-03	-1.26	2.5388e-02	2.5727e-02	-1.32

Table F.7 Comparison of fission rates between 1L and 2L schemes (ASSBLY-D)

	Zero BU			**BU at $k_{\text{eff}-\max}$**			**Max BU**		
	R_f^{D5}	R_f^{S2}	Δr	R_f^{D5}	R_f^{S2}	Δr	R_f^{D5}	R_f^{S2}	Δr
U235									
$1L\ G1$	8.6422e-02	8.6733e-02	-0.36	5.3186e-02	5.3194e-02	-0.01	9.6728e-03	9.5026e-03	1.79
$2L\ G1$	8.6194e-02	8.6729e-02	-0.62	5.3484e-02	5.3249e-02	0.44	9.3292e-03	9.4983e-03	-1.78
$1L\ G2$	2.9369e-01	2.9279e-01	0.31	1.8632e-01	1.8687e-01	-0.30	3.8520e-02	3.7905e-02	1.62
$2L\ G2$	2.9380e-01	2.9278e-01	0.35	1.8862e-01	1.8706e-01	0.83	3.7803e-02	3.7887e-02	-0.22
U238									
$1L\ G1$	2.5960e-02	2.6545e-02	-2.20	2.5421e-02	2.5621e-02	-0.78	3.4869e-02	3.5024e-02	-0.44
$2L\ G1$	2.6059e-02	2.6544e-02	-1.83	2.5446e-02	2.5647e-02	-0.78	3.5053e-02	3.5008e-02	0.13
$1L\ G2$	3.1781e-07	3.1766e-07	0.05	3.2381e-07	3.2451e-07	-0.21	4.9185e-07	4.9981e-07	-1.59
$2L\ G2$	3.1791e-07	3.1765e-07	0.08	3.2429e-07	3.2484e-07	-0.17	5.0103e-07	4.9958e-07	0.29
Pu239									
$1L\ G1$	-	-	-	1.0386e-02	1.0023e-02	3.62	1.7970e-02	1.7297e-02	3.89
$2L\ G1$	-	-	-	1.0172e-02	1.0033e-02	1.39	1.7750e-02	1.7289e-02	2.67
$1L\ G2$	-	-	-	9.8320e-02	9.7943e-02	0.39	1.8159e-01	1.8191e-01	-0.18
$2L\ G2$	-	-	-	9.6816e-02	9.8045e-02	-1.25	1.8208e-01	1.8183e-01	0.14
Pu241									
$1L\ G1$	-	-	-	1.9033e-03	1.8627e-03	2.18	1.1138e-02	1.1026e-02	1.01
$2L\ G1$	-	-	-	1.8091e-03	1.8646e-03	-2.98	1.1046e-02	1.1021e-02	0.22
$1L\ G2$	-	-	-	9.4169e-03	9.4393e-03	-0.24	6.1376e-02	6.2468e-02	-1.75
$2L\ G2$	-	-	-	9.0008e-03	9.4491e-03	-4.74	6.1910e-02	6.2439e-02	-0.85

Table F.8 Comparison of capture rates between 1L and 2L schemes (ASSBLY-D)

	Zero BU			**BU at $k_{\text{eff}-\max}$**			**Max BU**		
	R_c^{D5}	R_c^{S2}	Δr	R_c^{D5}	R_c^{S2}	Δr	R_c^{D5}	R_c^{S2}	Δr
U235									
$1L\ G1$	4.0614e-02	4.0665e-02	-0.13	2.5615e-02	2.5671e-02	-0.22	4.8044e-03	4.6869e-03	2.51
$2L\ G1$	4.0463e-02	4.0523e-02	-0.15	2.5701e-02	2.5521e-02	0.71	4.6298e-03	4.6890e-03	-1.26
$1L\ G2$	5.2031e-02	5.2210e-02	-0.34	3.2694e-02	3.3126e-02	-1.31	6.7180e-03	6.6079e-03	1.67
$2L\ G2$	5.2049e-02	5.2027e-02	0.04	3.3101e-02	3.2933e-02	0.51	6.5919e-03	6.6108e-03	-0.29
U238									
$1L\ G1$	1.9030e-01	1.8999e-01	0.16	1.8516e-01	1.8397e-01	0.65	2.5319e-01	2.5220e-01	0.39
$2L\ G1$	1.8932e-01	1.8932e-01	-0.00	1.8376e-01	1.8289e-01	0.48	2.5252e-01	2.5231e-01	0.08
$1L\ G2$	3.2480e-02	3.2562e-02	-0.25	3.3065e-02	3.3371e-02	-0.92	5.0170e-02	5.0806e-02	-1.25
$2L\ G2$	3.2491e-02	3.2448e-02	0.13	3.3114e-02	3.3176e-02	-0.19	5.1105e-02	5.0828e-02	0.55
Pu239									
$1L\ G1$	-	-	-	6.1021e-03	5.8946e-03	3.52	1.0571e-02	1.0087e-02	4.80
$2L\ G1$	-	-	-	5.9716e-03	5.8602e-03	1.90	1.0434e-02	1.0092e-02	3.39
$1L\ G2$	-	-	-	5.5580e-02	5.6142e-02	-1.00	1.0029e-01	1.0097e-01	-0.68
$2L\ G2$	-	-	-	5.4745e-02	5.5814e-02	-1.91	1.0049e-01	1.0102e-01	-0.52
Pu241									
$1L\ G1$	-	-	-	6.0462e-04	5.9792e-04	1.12	3.5287e-03	3.4978e-03	0.88
$2L\ G1$	-	-	-	5.7528e-04	5.9443e-04	-3.22	3.5015e-03	3.4994e-03	0.06
$1L\ G2$	-	-	-	3.5045e-03	3.5501e-03	-1.28	2.2519e-02	2.2927e-02	-1.78
$2L\ G2$	-	-	-	3.3504e-03	3.5294e-03	-5.07	2.2708e-02	2.2938e-02	-1.00

APPENDIX G RELATIVE ERRORS IN ALL RINGS

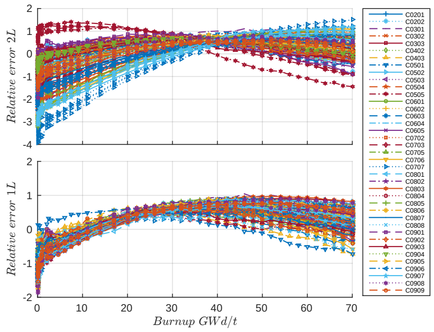

(a) U236

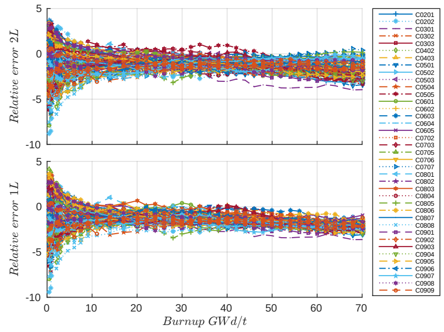

(b) Np237

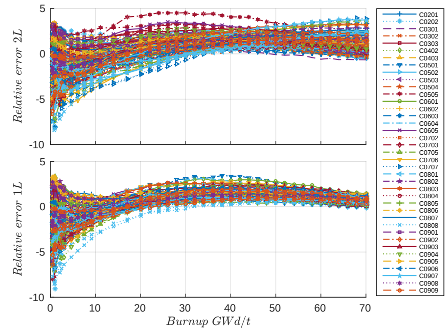

(c) Pu238

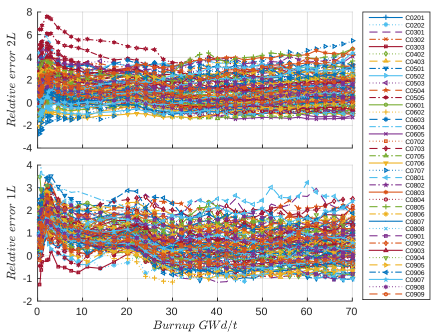

(d) Pu240

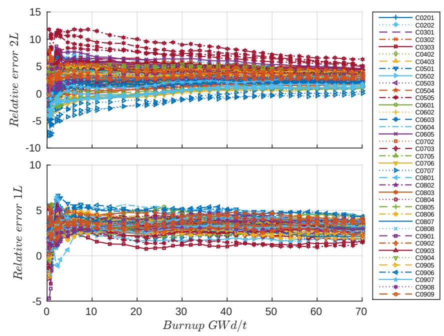

(e) Pu242

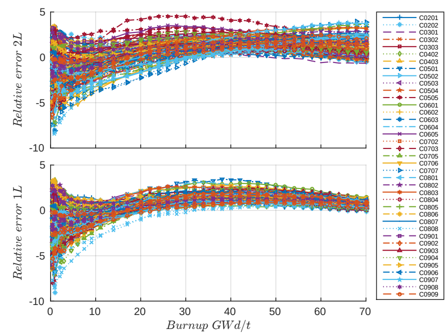

(f) Sm147

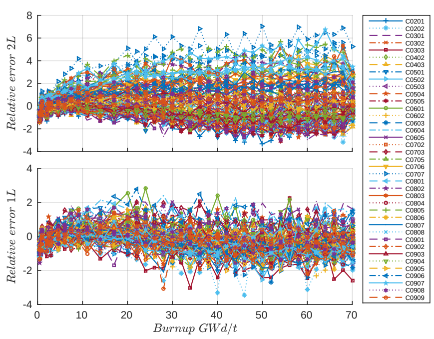

(g) Sm149

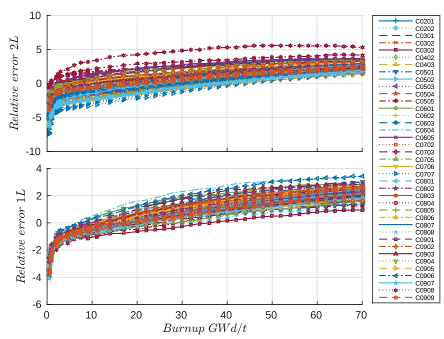

(h) Sm150

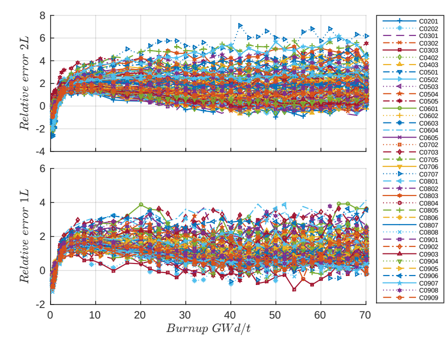

(i) Sm151

Figure G.1 Relative errors in atomic densities in all rings of all pins (ASSBLY-A)

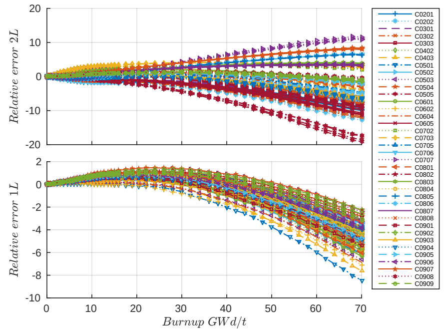

(a) U235 (UOX pins)

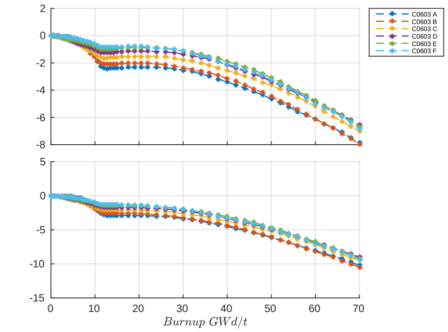

(b) U235 (Gd pins)

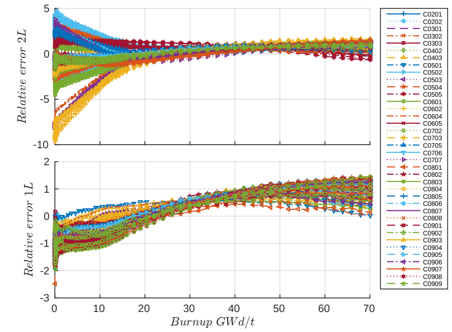

(c) U236 (UOX pins)

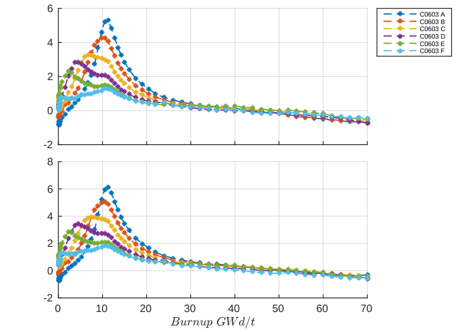

(d) U236 (Gd pins)

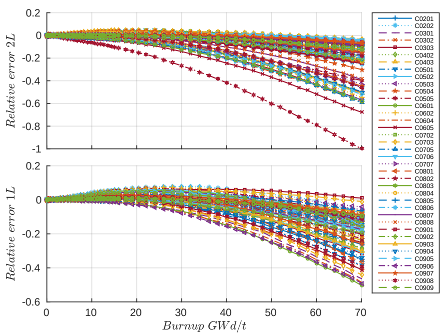

(e) U238 (UOX pins)

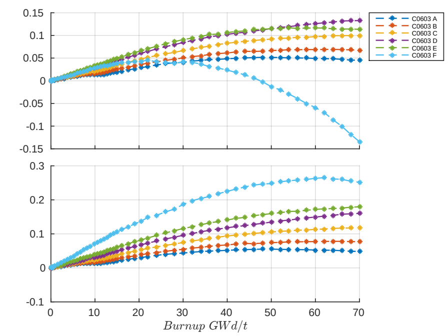

(f) U238 (Gd pins)

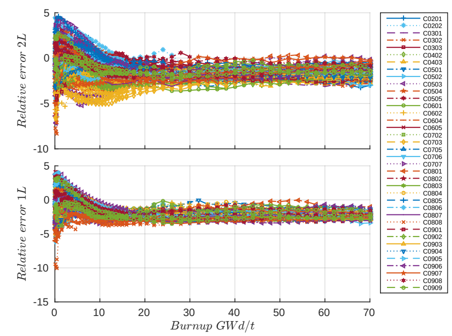

(g) Np237 (UOX pins)

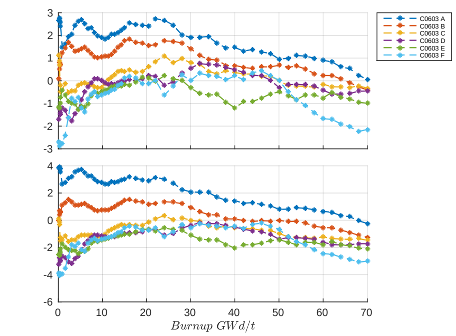

(h) Np237 (Gd pins)

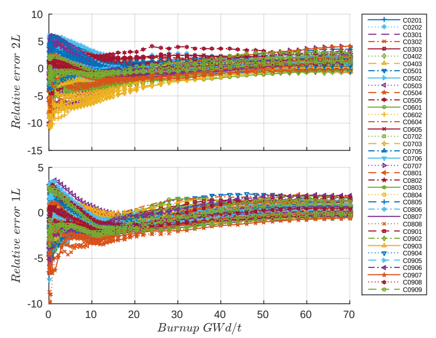

(i) Pu238 (UOX pins)

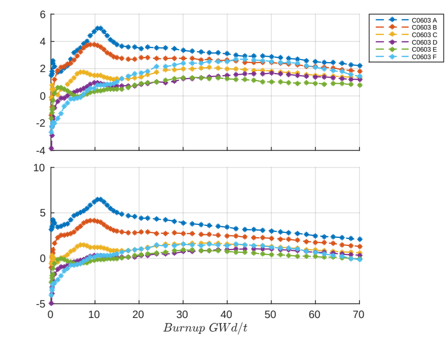

(j) Pu238 (Gd pins)

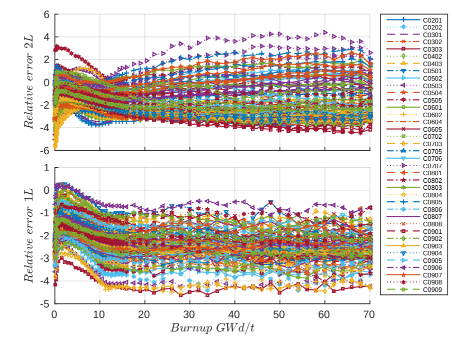

(k) Pu239 (UOX pins)

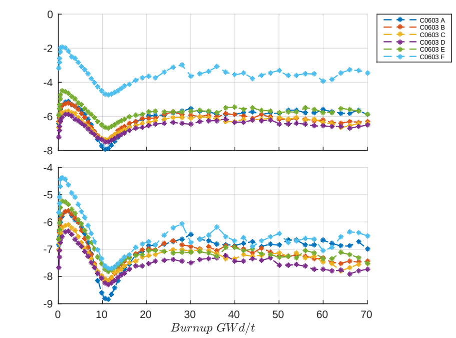

(l) Pu239 (Gd pins)

Figure G.2 Relative errors in atomic densities in all rings of all pins (ASSBLY-B, 1)

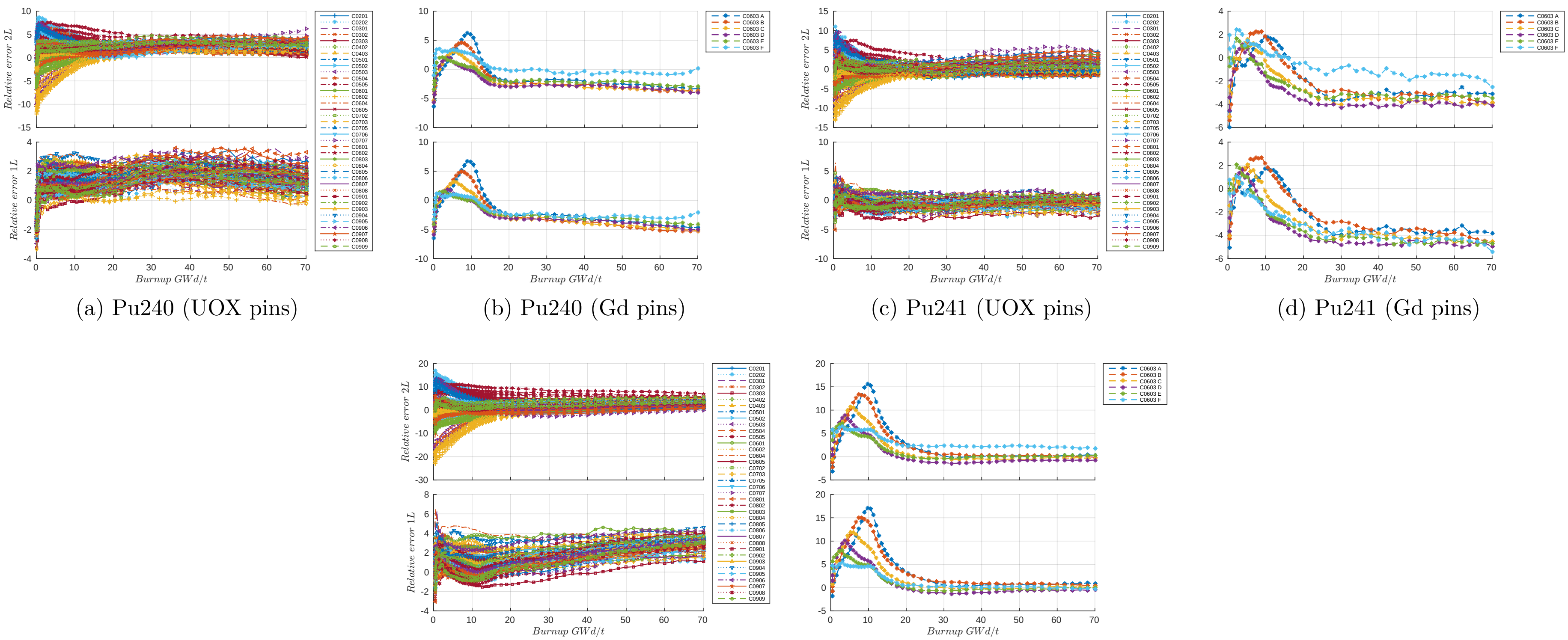

(a) Pu240 (UOX pins) (b) Pu240 (Gd pins) (c) Pu241 (UOX pins) (d) Pu241 (Gd pins)

(e) Pu242 (UOX pins) (f) Pu242 (Gd pins)

Figure G.3 Relative errors in atomic densities in all rings of all pins (ASSBLY-B, 2)

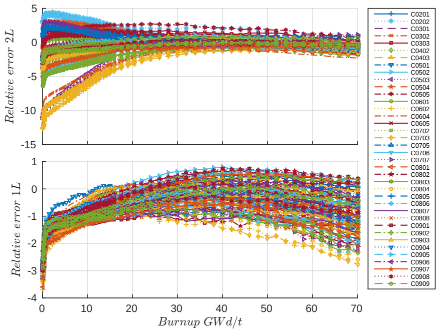

(a) Sm147 (UOX pins)

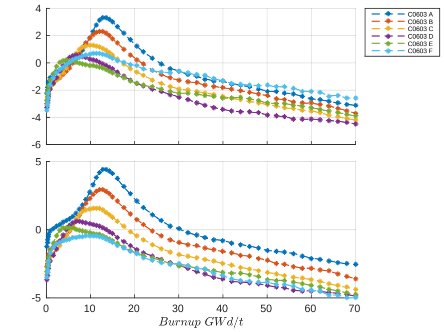

(b) Sm147 (Gd pins)

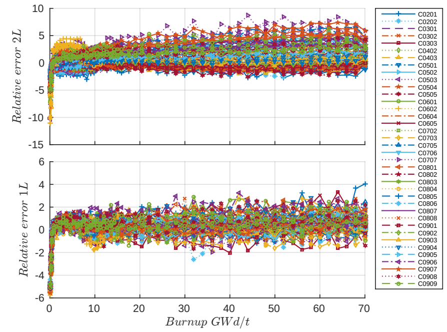

(c) Sm149 (UOX pins)

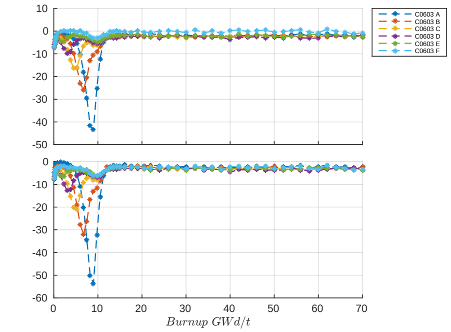

(d) Sm149 (Gd pins)

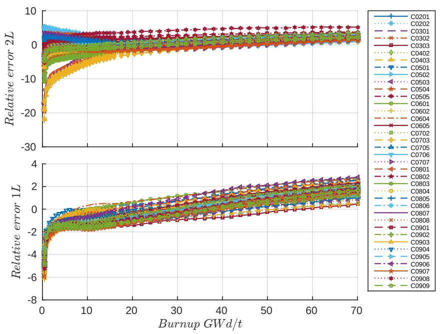

(e) Sm150 (UOX pins)

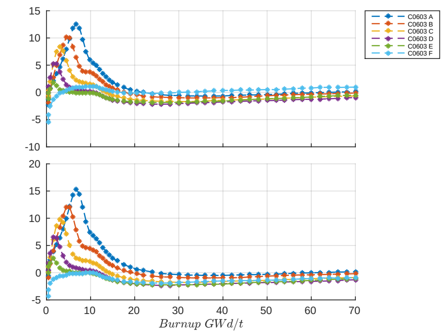

(f) Sm150 (Gd pins)

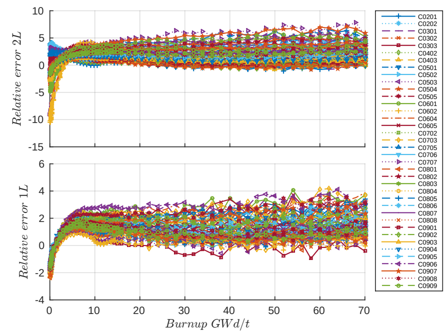

(g) Sm151 (UOX pins)

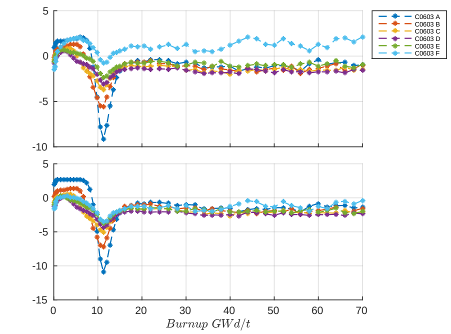

(h) Sm151 (Gd pins)

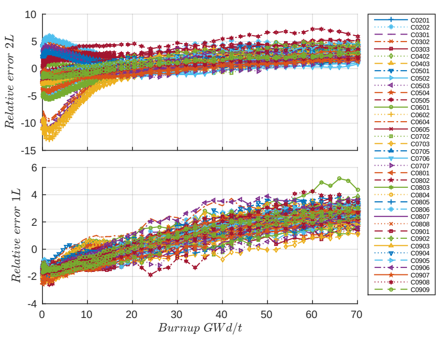

(i) Sm152 (UOX pins)

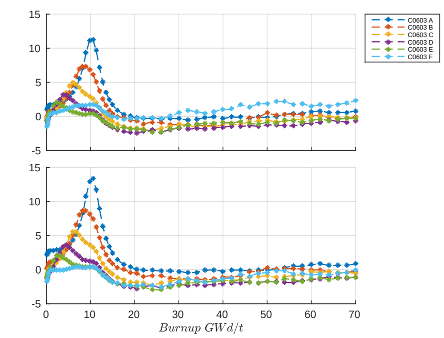

(j) Sm152 (Gd pins)

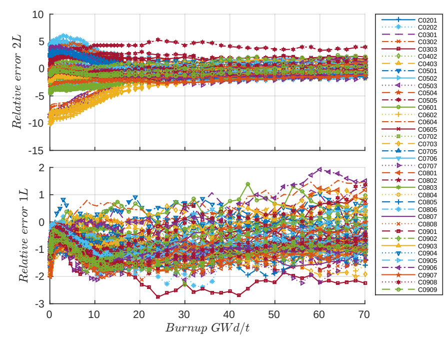

(k) Eu153 (UOX pins)

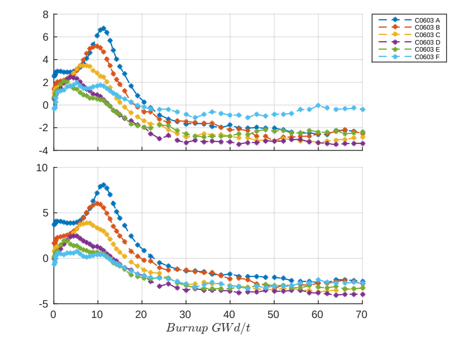

(l) Eu153 (Gd pins)

Figure G.4 Relative errors in atomic densities in all rings of all pins (ASSBLY-B, 3)

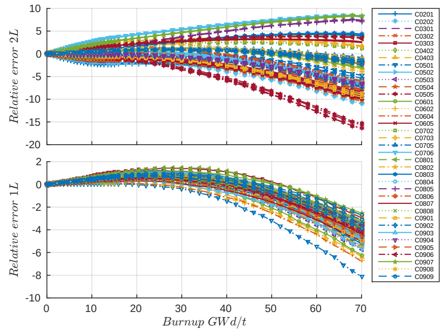

(a) U235 (UOX pins)

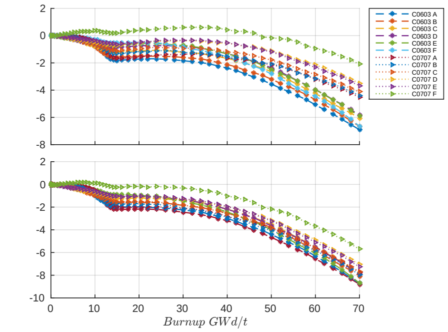

(b) U235 (Gd pins)

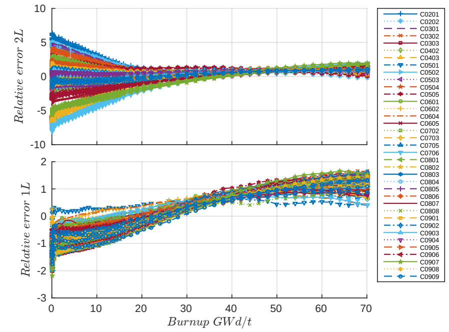

(c) U236 (UOX pins)

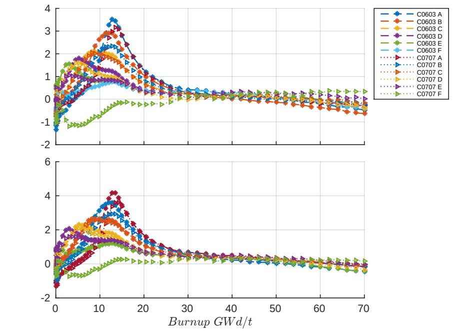

(d) U236 (Gd pins)

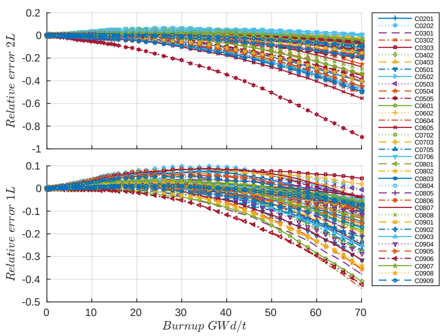

(e) U238 (UOX pins)

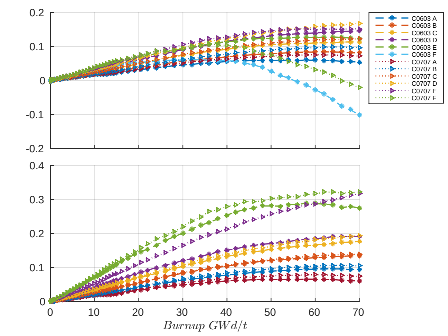

(f) U238 (Gd pins)

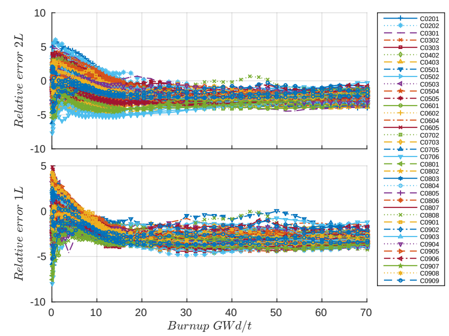

(g) Np237 (UOX pins)

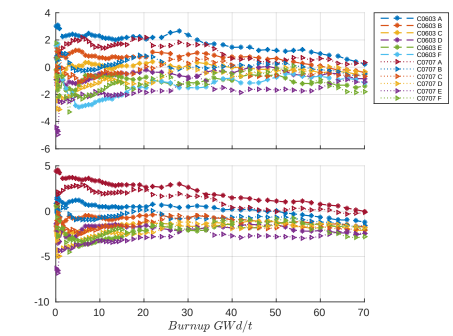

(h) Np237 (Gd pins)

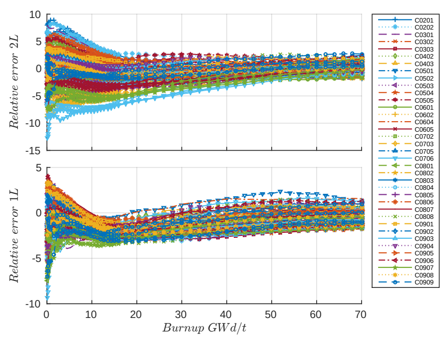

(i) Pu238 (UOX pins)

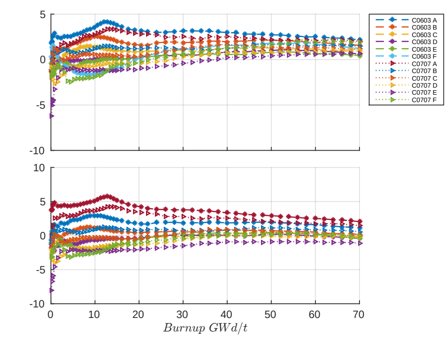

(j) Pu238 (Gd pins)

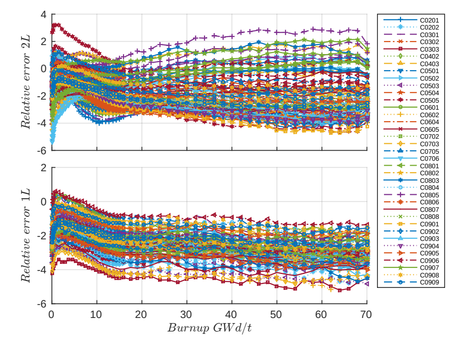

(k) Pu239 (UOX pins)

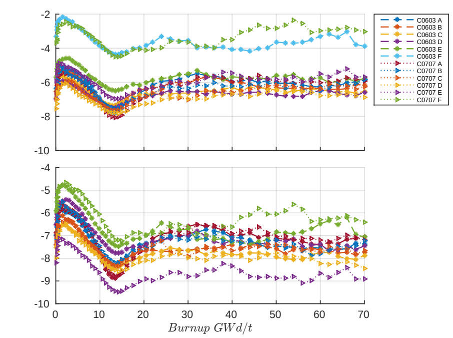

(l) Pu239 (Gd pins)

Figure G.5 Relative errors in atomic densities in all rings of all pins (ASSBLY-C, 1)

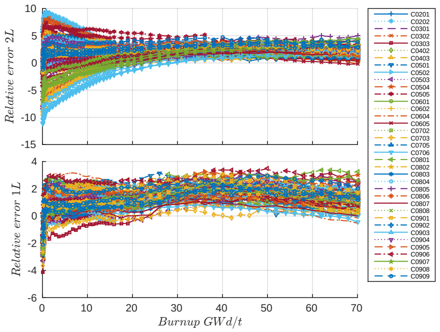

(a) Pu240 (UOX pins)

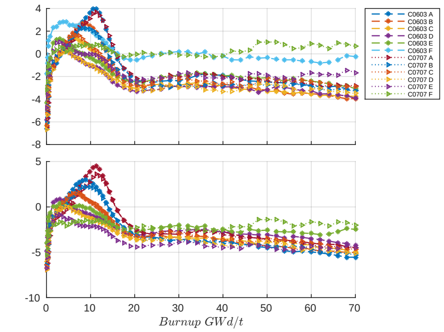

(b) Pu240 (Gd pins)

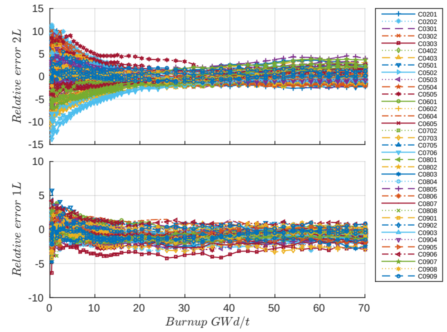

(c) Pu241 (UOX pins)

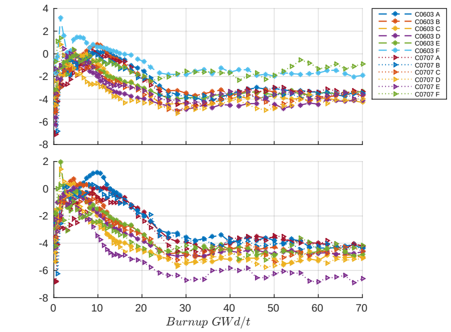

(d) Pu241 (Gd pins)

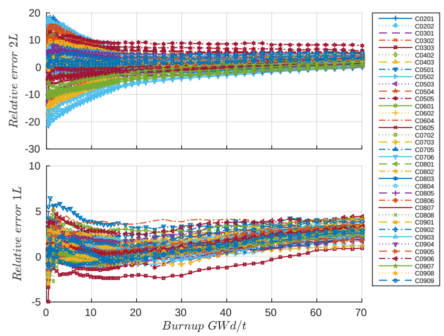

(e) Pu242 (UOX pins)

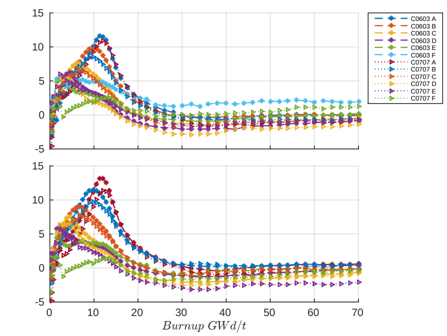

(f) Pu242 (Gd pins)

Figure G.6 Relative errors in atomic densities in all rings of all pins (ASSBLY-C, 2)

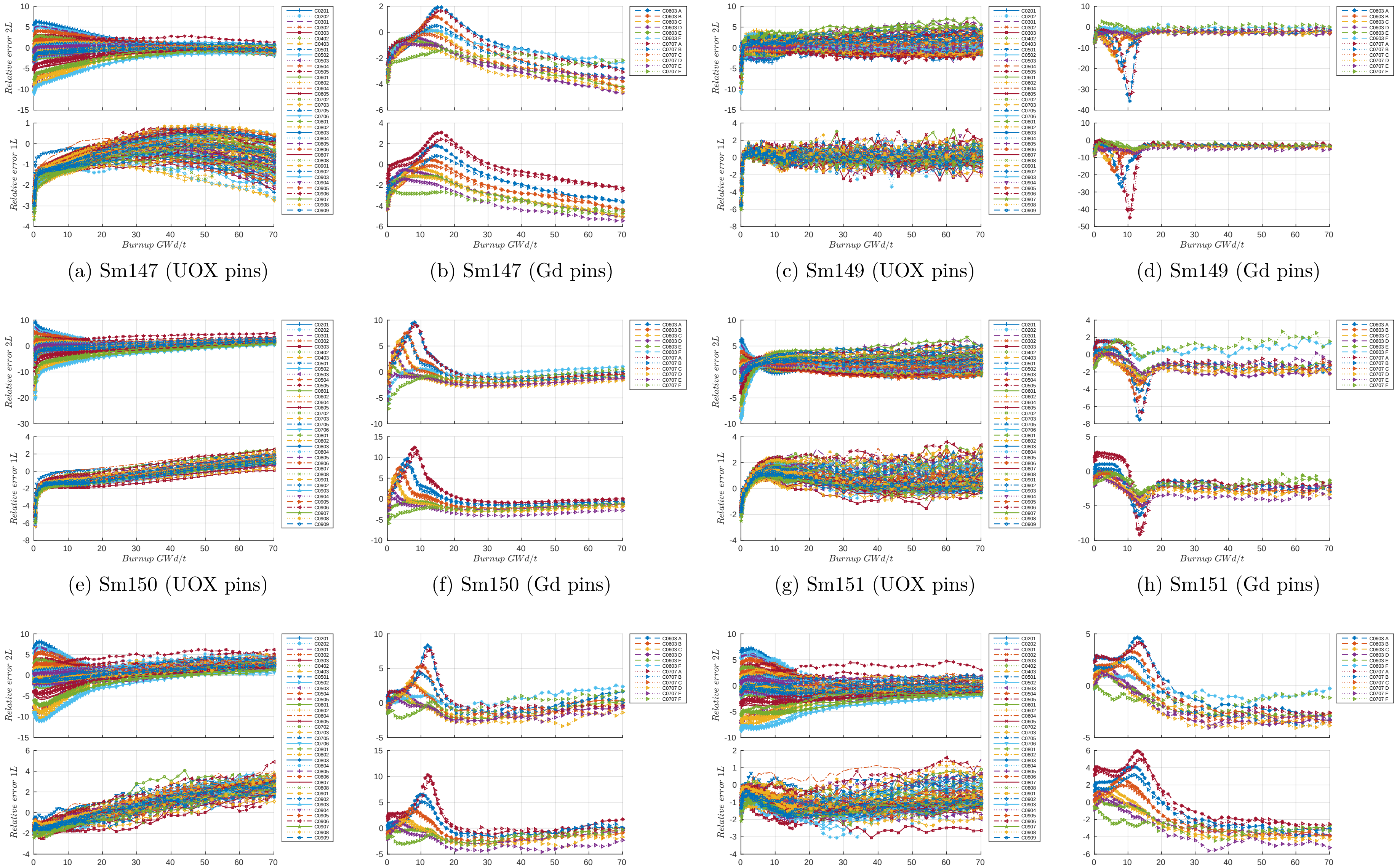

(a) Sm147 (UOX pins)
(b) Sm147 (Gd pins)
(c) Sm149 (UOX pins)
(d) Sm149 (Gd pins)
(e) Sm150 (UOX pins)
(f) Sm150 (Gd pins)
(g) Sm151 (UOX pins)
(h) Sm151 (Gd pins)
(i) Sm152 (UOX pins)
(j) Sm152 (Gd pins)
(k) Eu153 (UOX pins)
(l) Eu153 (Gd pins)

Figure G.7 Relative errors in atomic densities in all rings of all pins (ASSBLY-C, 3)

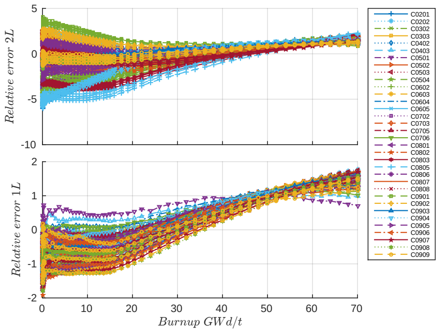

(a) U236 (UOX pins)

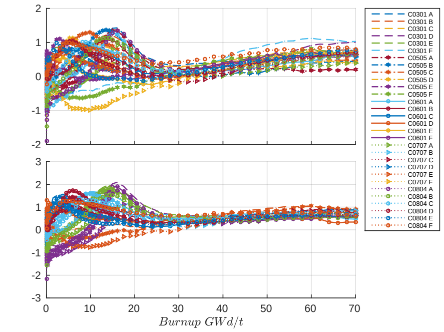

(b) U236 (Gd pins)

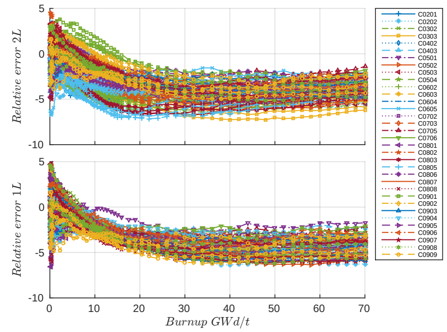

(c) Np237 (UOX pins)

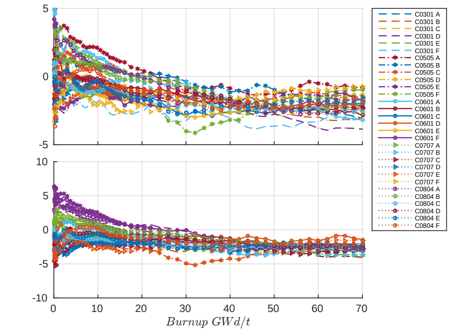

(d) Np237 (Gd pins)

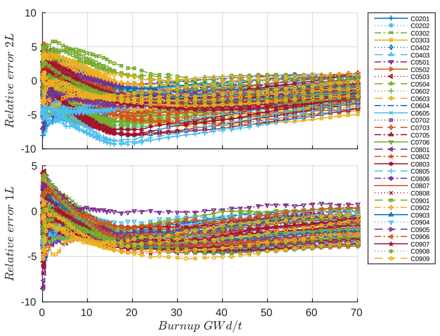

(e) Pu238 (UOX pins)

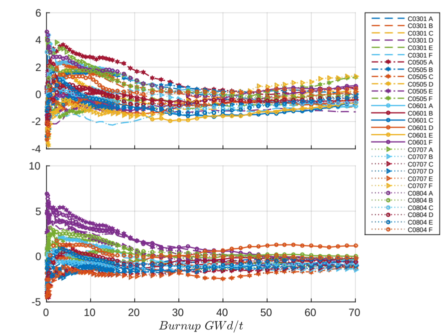

(f) Pu238 (Gd pins)

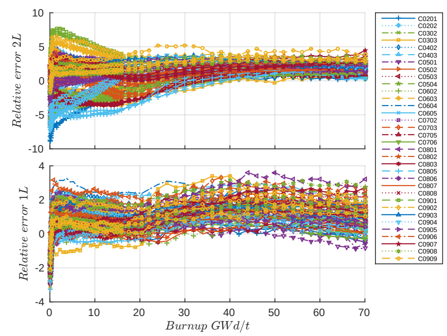

(g) Pu240 (UOX pins)

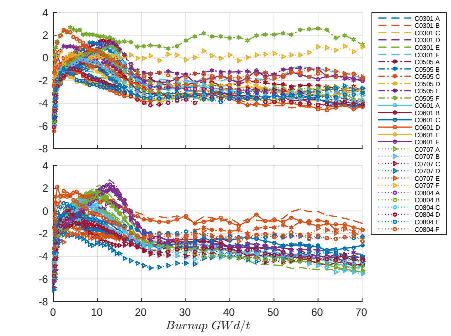

(h) Pu240 (Gd pins)

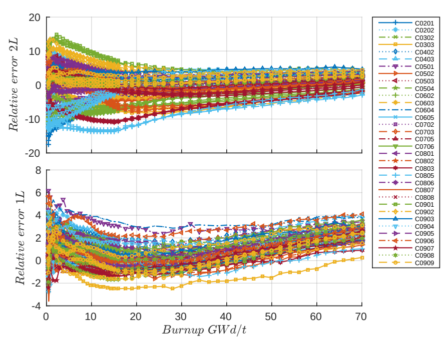

(i) Pu242 (UOX pins)

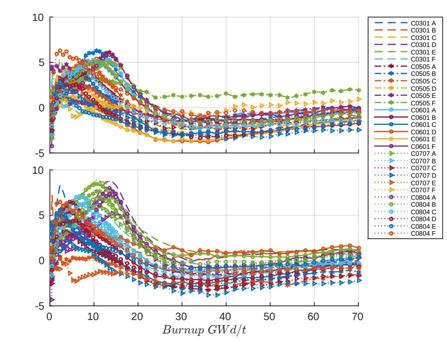

(j) Pu242 (Gd pins)

Figure G.8 Relative errors in atomic densities in all rings of all pins (ASSBLY-D, 1)

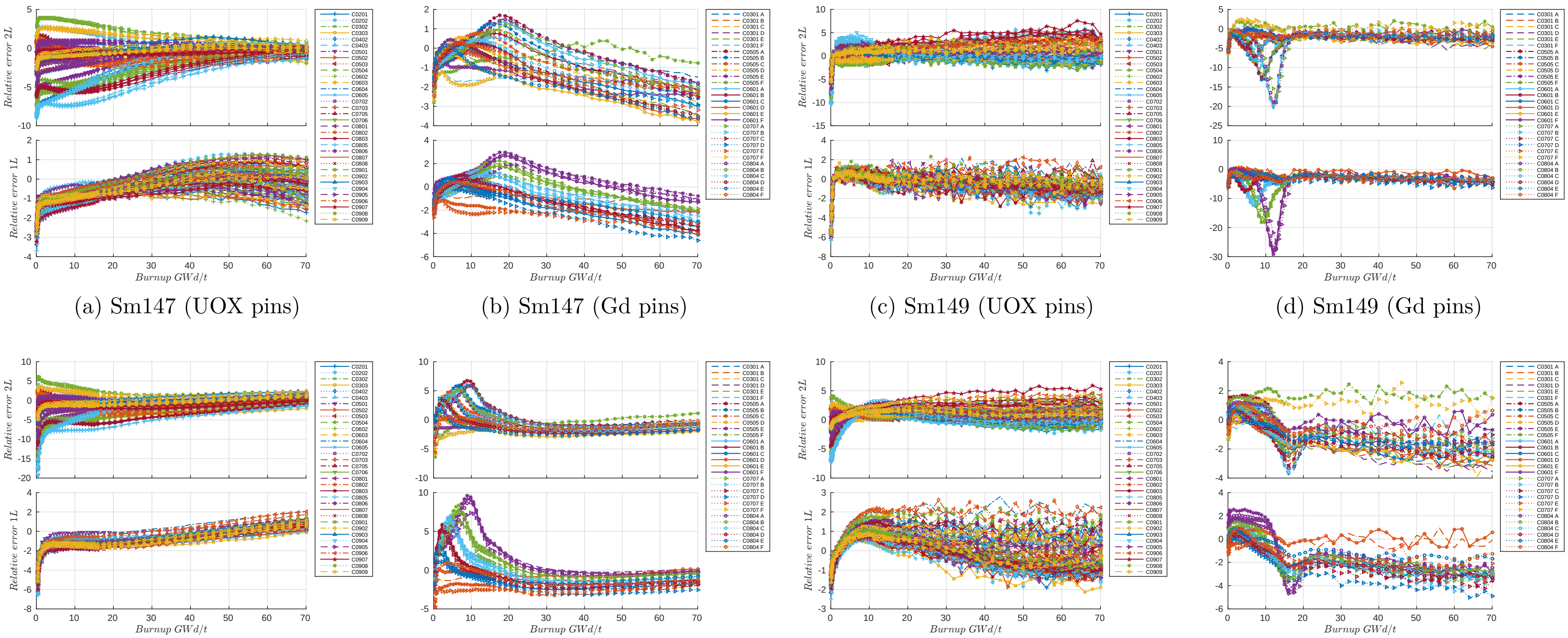

(a) Sm147 (UOX pins) (b) Sm147 (Gd pins) (c) Sm149 (UOX pins) (d) Sm149 (Gd pins)

(e) Sm150 (UOX pins) (f) Sm150 (Gd pins) (g) Sm151 (UOX pins) (h) Sm151 (Gd pins)

Figure G.9 Relative errors in atomic densities in all rings of all pins (ASSBLY-D, 2)